



USDOT Tier 1  
University Transportation Center  
on Improving Rail Transportation  
Infrastructure Sustainability and Durability

Final Report VT-10

**MANAGING VEHICLE-RAIL INTERFACE (VRI) DYNAMICS AND MECHANICS**

By

Mehdi Ahmadian, J. Bernard Jones Chair and Director

and

Karan Kothari, Graduate Research Assistant

Center for Vehicle Systems and Safety  
Railway Technologies Laboratory  
Virginia Tech  
3103 Commerce Street  
Blacksburg, VA 24060

October 2018

Grant Number: 69A3551747132



**DISCLAIMER**

The contents of this report reflect the views of the authors, who are responsible for the facts and the accuracy of the information presented herein. This document is disseminated in the interest of information exchange. The report is funded, partially or entirely, by a grant from the U.S. Department of Transportation's University Transportation Centers Program. However, the U.S. Government assumes no liability for the contents or use thereof.

## Executive Summary

The primary purpose of this study is to perform accurate dynamic measurements on a scaled roller rig designed and constructed by Virginia Tech and the Federal Railroad Administration (VT-FRA Roller Rig). The study also aims at determining the effect of naturally generated third-body layer deposits (because of the wear of the wheel and/or roller) on creep or traction forces. The wheel-rail contact forces, also referred to as traction forces, are critical for all aspects of rail dynamics. These forces are quite complex and they have been the subject of several decades of research, both in experiments and modeling. The primary intent of the VT-FRA Roller Rig is to provide an experimental environment for more accurate testing and evaluation of some of the models currently in existence, as well as evaluate new hypothesis and theories that cannot be verified on other roller rigs available worldwide.

The Rig consists of a wheel and roller in a vertical configuration that allows for closely replicating the boundary conditions of railroad wheel-rail contact via actively controlling all the wheel-rail interface degrees of freedom: angle of attack, cant angle, normal load and lateral displacement, including flanging. The Rig has two sophisticated independent drivelines to precisely control the rotational speed of the wheels, and therefore their relative slip or creepage. The Rig benefits from a novel force measurement system, suitable for steel on steel contact, to precisely measure the contact forces and moments at the wheel-rail contact.

Experimental studies are conducted on the VT – FRA Roller Rig that involved varying the angle of attack, wheel and rail surface lubricity condition (i.e., wet vs. dry rail), and wheel wear, to study their effect on wheel-rail contact mechanics and dynamics. The wheel-rail contact is in between a one-fourth scale AAR-1B locomotive wheel and a roller machined to US-136 rail profile. A quantitative assessment of the creep-creepage measurements, which is an important metric to evaluate the wheel-rail contact mechanics and dynamics, is presented. A MATLAB routine is developed to generate the creep-creepage curves from measurements conducted as part of a broad experimental study. The shape of the contact patch and its pressure distribution have been discussed. An attempt is made to apply the results to full-scale wheels and flat rails. The research results will help in the development of better simulation models for non-Hertzian contact and non-linear creep theories for wheel-rail contact problems that require further research to more accurately represent the wheel-rail interaction.

Contents	
Contents	iv
List of Figures	vi
List of Tables	ix
Chapter 1. Introduction	1
1.1 Broad Overview	1
1.2 Objectives	1
1.3 Contributions	1
1.4 Outline	2
Chapter 2. Background	3
2.1 Rolling Contact Mechanics	4
2.1.1 Normal Contact Problem	5
2.1.2 Tangential Contact Problem	6
2.2 Brief Description of VT – FRA Roller Rig	7
2.2.1 Data Acquisition and Control Architecture	10
2.2.2 Roller Rig’s Capabilities	12
Chapter 3. Test Setup	14
3.1 Measuring Creep Forces and Moments at the Wheel-Rail Contact	16
3.1.2 Overview of Different Control Algorithms for Motion Control	21
3.1.3 Control Algorithm for Wheel and Roller Driveline	26
3.1.4 Control Algorithm for Linear Positioning Systems	26
3.1.5 Wheel and Rail Profiles	28
3.1.6 Wheel Alignment	29
3.1.7 Contact Patch Parameter Estimation Using Hertzian Contact Theory	30
3.1.8 Creepage Control Between Wheel-Rail Contact	32
Chapter 4. Experiment Workflow	36
4.1 Effect of Input Parameters on Measured Responses	37
4.1.1 Angle of Attack (AoA)	37
4.1.2 Cant Angle	38
4.1.3 Lateral Displacement	39
4.2 Experiment Design Process	40
4.2.1 Contact Surface Preparation	41
4.2.2 Setting boundary conditions	41
4.2.3 Reference Points for Vertical Actuators	42
4.2.4 Load Application and Motion Start	42
4.2.5 Data Collection	43
4.2.6 Unloading and Resetting Instrumentation	43
Chapter 5. Data Post–Processing	44
5.1 Raw Data Collection	45
5.2 Batch Processing and Data Sorting	48
5.3 Low Pass Filtering of Raw Force Data	50
5.4 Checking Mean Normal Load Distribution	51
5.5 Correlation Analysis	52
5.6 Normalized Creep Force Computation	53
5.7 Experimental Mean of Means	55

Chapter 6. Testing Results.....	56
6.1 Case Study 1: Influence of Angle of Attack on Adhesion Coefficient and Lateral Stability .....	56
6.1.1 Baseline Study .....	57
6.1.2 Angle of Attack Study .....	59
6.1.3 Comparison of Results for Baseline Study and Angle of Attack Study .....	61
6.2 Case Study 2: Influence of Water Lubricated Wheel and Rail on Adhesion-Creepage Behavior .....	63
6.3 Case Study 3: Effect of Wheel Wear on Adhesion-Creepage Behavior .....	66
6.4 Repeatability of Measurements.....	70
Chapter 7. Summary and Future Studies .....	73
7.1 Summary .....	73
7.2 Recommendations for Future Studies .....	73
References	75

## LIST OF FIGURES

Figure 2-1 Pure sliding contact (left) versus rolling contact during acceleration (right) [9].....	5
Figure 2-2 General case of Hertzian contact [11].....	6
Figure 2-3 Graph showing adhesion as a function of creep rate at contact patch for dry wheel-rail type contact [8] .....	7
Figure 2-4 Isometric view of solid model (left), and fully assembled (right) VT – FRA Roller Rig .....	9
Figure 2-5 Front view of solid model (left), and fully assembled (right) VT – FRA Roller Rig ...	9
Figure 2-6 Top view of solid model (left), and fully assembled (right) VT – FRA Roller Rig ...	10
Figure 2-7 Schematic diagram of the Roller Rig’s configured motion architecture [5].....	12
Figure 3-1 Overview of VT – FRA Roller Rig testing facility (top); isometric view of the Roller Rig with rotary and linear positioning systems indicated (bottom-left); enclosure for the control tower of Roller Rig including S700 drives, AKD drives, safety/control circuits, regenerative and dynamic brake resistors and operator interface panel (bottom-right) [21, 23] .....	15
Figure 3-2 Contact coordinate system for the Roller Rig .....	15
Figure 3-3 Side view of Rig showing primary and secondary load platforms and load paths (left); top view of Rig showing wheel and motor dynamometers after being installed on the Rig (right) [21-23].....	16
Figure 3-4 Primary load platform mounted on the Roller Rig (left); diagram of primary load platform, mounted with four 6-component piezoelectric load cells on each corner (right) .....	17
Figure 3-5 High-pass filter circuit diagram inside the Kistler charge amplifiers [27].....	20
Figure 3-6 Step response (top), and gain and phase responses (bottom) of Kistler charge amplifier at low frequencies for DC (long) mode and short mode measuring modes of operation [27] .....	20
Figure 3-7 Measurements in short mode of Kistler charge amplifier showing piezoelectric sensor drift in normal load (left), and measurements in DC (long) mode of Kistler charge amplifier with no piezoelectric sensor drift (right).....	21
Figure 3-8 Block diagram showing Position Control (PC) mode for non-gantry axis of the Roller Rig.....	22
Figure 3-9 Surface imperfections and alignment tolerances resulting in radial run-out of wheel and roller .....	23
Figure 3-10 Normal load oscillations at wheel-rail contact patch without creepage (top), and superimposed wheel and roller time periods on time series plot (bottom) .....	25
Figure 3-11 Power Spectral Density (PSD) of normal load data showing dominant peaks at wheel and roller rotational frequencies and their harmonics.....	26
Figure 3-12 Block diagram showing Position Control (PC) mode for gantry (without yaw) axis of the Roller Rig.....	28
Figure 3-13 Detailed drawing of US 136 rail cross-section (left), and detailed drawing of AAR-1B wide flange wheel profile for freight (right) .....	29
Figure 3-14 Driveline with laser sensor and receiver units mounted on either side of coupling .	30
Figure 3-15 Components of the OPTALIGN smart RS5 laser alignment system.....	30
Figure 3-16 Hertzian contact patch stress for cylinder-on-cylinder contact condition [32] .....	31
Figure 3-17 Front view of the Roller Rig showing the wheel and roller mounted in a vertical configuration .....	33
Figure 4-1 Input-process-output diagram for Roller Rig.....	37
Figure 4-2 Angle of Attack (AoA) of wheelset relative to rail during curving .....	38

Figure 4-3 Vertical difference in elevation of inner and outer rail measured as cant angle .....	38
Figure 4-4 Lateral displacement of wheelset from equilibrium position.....	40
Figure 4-5 Block diagram of workflow of each experiment for conducting the creep-creepage measurements.....	41
Figure 4-6 Snapshot of Roller Rig’s Motion Console Graphic User Interface (GUI).....	42
Figure 4-7 Motion Scope (MS) traces consisting of data collected from 16 sensor channels.....	43
Figure 5-1 Data post–processing workflow for generating creep-creepage curves from an experimental study .....	44
Figure 5-2 Sample of raw force data collected from the DAQ system for measurement points corresponding to 1.9% creepage in the experimental study .....	47
Figure 5-3 Trapezoidal point-to-point motion for wheel and roller servo motors (top); actual, and commanded wheel positions (middle-right); actual, and commanded wheel velocities (middle-right); actual, and commanded roller positions (bottom-left); actual, and commanded roller velocities (bottom-right) .....	48
Figure 5-4 Wheel Rotations per Second (RPS), versus time where each step represents a creepage value between 0.2% and 10% .....	50
Figure 5-5 Raw measured force data in Newton (left), digital Butterworth low pass filtered measured force data (filter order = 4, break frequency = 10 Hz, sampling frequency = 2 kHz, creepage: 1.9%) (right) .....	51
Figure 5-6 Mean normal load distribution for baseline study and angle of attack study experiments .....	52
Figure 5-7 Correlation coefficients between the longitudinal creep force and normal load for baseline study and angle of attack study experiments .....	53
Figure 5-8 Adhesion coefficients for longitudinal creepages ranging from 0-6% for baseline study experiments.....	54
Figure 5-9 Adhesion coefficients for longitudinal creepages ranging from 0-6% for angle of attack study experiments .....	54
Figure 5-10 L/V ratios for longitudinal creepages ranging from 0-6% for angle of attack study experiments.....	55
Figure 6-1 Mean of mean of adhesion coefficients for 0-6% longitudinal creepage with rational fit curve for baseline study experiments.....	58
Figure 6-2 Mean of mean of L/V ratio for 0-6% longitudinal creepage with rational fit curve for baseline study experiments .....	59
Figure 6-3 Mean of mean of adhesion coefficients for 0-6% longitudinal creepage with rational fit curve for angle of attack study experiments .....	60
Figure 6-4 Mean of mean of L/V ratio for 0-6% longitudinal creepage with rational fit curve for angle of attack study experiments.....	61
Figure 6-5 Comparison of adhesion coefficient as a function of longitudinal creepage for baseline and angle of attack studies .....	62
Figure 6-6 Comparison of L/V ratio as a function of longitudinal creepage for baseline and angle of attack studies.....	63
Figure 6-7 Adhesion coefficients for longitudinal creepages ranging from 0-6% for dry contact and water lubricated contact studies with contact surface condition as a controlled parameter...	65
Figure 6-8 Rational curve fit of experimental data points for dry and water lubricated studies showing variation of adhesion coefficients as a function of longitudinal creepage .....	66

Figure 6-9 Experimental testing results of time series analysis of adhesion coefficients at high creepage and normal load .....	68
Figure 6-10 Comparison of wheel profile before conducting the wear test experiment (left) and after conducting the wear test experiment (right) .....	68
Figure 6-11 Comparison of roller profile before conducting the wear test experiment (left) and after conducting the wear test experiment (right) .....	69
Figure 6-12 Adhesion coefficients for 0-2% longitudinal creepage with rational fit curve for Case Study 3 experiments.....	70
Figure 6-13 Boxplot analysis of adhesion coefficients taken from 24 experiments conducted with exactly the same boundary conditions .....	70
Figure 6-14 Boxplot analysis of adhesion coefficients for experiments from specific creepage points for the baseline study experiments .....	71
Figure 6-15 Boxplot analysis of adhesion coefficients for experiments from specific creepage points, for the angle of attack study experiments .....	72
Figure 6-16 Box plot analysis of L/V ratios for experiments from specific creepage points for the angle of attack study experiments.....	72

## LIST OF TABLES

Table 2-1 Scaling factors for the physical quantities of the Rig [4, 5] .....	3
Table 2-2 12 nodes currently used by the Roller Rig, with connected components, DOFs controlled, and their corresponding axes number and motor number shown [21] .....	10
Table 2-3 Summary of the Roller Rig’s capabilities .....	12
Table 3-1 List of AIN channel numbers for mapping all forces and moments from motor dynamometer to Motion Scope.....	17
Table 3-2 List of AIN channel numbers for mapping all forces and moments from wheel dynamometer to Motion Scope.....	18
Table 3-3 Parameters to calculate the half-width at contact patch .....	31
Table 3-4 Wheel and roller commanded velocity counts calculated for adhesion-creepage measurements for conducting experimental studies on the Roller Rig.....	34
Table 5-1 Boundary conditions for baseline experimental study .....	45
Table 5-2 Conversion factors for converting raw data from DAQ to meaningful physical units	46
Table 5-3 2D lookup table consists of creepage on the Y-axis and wheel RPS on the X-axis for all wheel longitudinal commanded velocities.....	49
Table 6-1 List of testing parameters for baseline and angle of attack studies .....	57
Table 6-2 Regression model parameters for creep-creepage curves for baseline study and angle of attack study .....	61
Table 6-3 Summary of testing parameters for dry contact and water lubricated contact studies .	64
Table 6-4 Summary of boundary conditions for the wear test.....	67

## **Chapter 1. Introduction**

### **1.1 Broad Overview**

A 1/4<sup>th</sup> scale roller rig has been successfully designed and assembled at the Railway Technologies Laboratory (RTL), Virginia Tech. The Rig has been developed with an aim to shed light on the wheel-rail contact mechanics with an unprecedented level of accuracy.

The state-of-the-art Virginia Tech – Federal Railroad Administration (VT – FRA) Roller Rig has been commissioned successfully, and a series of contact mechanics and dynamic testing has been performed on the Rig. The Rig has been designed with the aim of conducting wheel-rail contact studies, which plays a crucial role in the behavior of railcars. The data is collected from experimental testing with an objective to create dynamic models, such as the creep-creepage curves. A literature review of past studies is conducted to validate the results obtained from the Rig by comparing the results from other contact mechanics' rigs across the world. The VT – FRA Roller Rig stands out from all other rigs as it makes use of state-of-the-art technologies from sophisticated motion control algorithms, data acquisition system, system integration, and high precision linear and rotary servo motors. This, combined with a three-layer safety system, unified communication protocol between sensors, and the ability to accommodate laser sensors, vision systems and IR cameras, makes the VT – FRA Roller Rig capable of exploring the unknown physics behind wheel-rail contact with an unprecedented level of accuracy. The objective of the Rig is to facilitate the design of faster, safer, and more efficient railway systems.

### **1.2 Objectives**

The aim of this study is to experimentally evaluate the creep forces at the wheel-rail contact to better understand the tangential contact problem, and provide a quantitative assessment of the accuracy and repeatability of measurements made on the VT-FRA Roller Rig. Specifically, the study intends to:

- Experimentally evaluate common railroad field scenarios on the Roller Rig and analyze its effect on wheel-rail contact creep forces,
- Analyze the behavior of adhesion coefficient and L/V ratio as a function of creepage (slip) at the wheel-rail contact,
- Establish experiment workflow to perform contact mechanics studies by selecting the independent, dependent, and control variables,
- Develop data processing algorithms to process and analyze the data across multiple contact mechanics experiments, and
- Establish the repeatability band for the force measurements at the contact patch.

### **1.3 Contributions**

The contributions of this study in regard to the VT – FRA Roller Rig include:

1. Quantifying Roller Rig's performance by analyzing experimental data,

2. Establishing baseline test results and performing experimental testing, data acquisition, and analysis for validating rail vehicle dynamics models,
3. Performing case studies involving the effects of angle of attack, cant angle, third-body layer and wheel tread wear on wheel-rail contact creep forces,
4. Defining protocols and procedures for future creep-creepage studies, wear studies, and other contact mechanics studies, and
5. Establishing measurement repeatability bandwidths for creep-creepage measurements.

## 1.4 Outline

This document is divided into seven chapters.

**Chapter 1** discusses the broad overview, objectives, and contributions of the research presented as a part of this report.

**Chapter 2** provides a background on various aspects of wheel-rail contact mechanics and dynamics, and provides a literature review of the past studies conducted on roller rigs around the world. A brief description of the VT – FRA Roller Rig, along with its various capabilities and limitations are also discussed in this chapter.

**Chapter 3** discusses the test setup of the VT – FRA Roller Rig with an in-depth discussion of different positioning systems and their feedback control loops, and the wheel and rail profiles used for conducting the experiments. The contact coordinate system, measurement of contact patch forces, moments, and creepage control at the wheel-rail contact have been discussed. A time and frequency domain analysis of the normal force data, along with a method to estimate the contact stress between the wheel-rail contact, have been discussed.

**Chapter 4** gives a comprehensive description of the experiment workflow that is developed for conducting reliable and repeatable tests on the Roller Rig. All of the inputs to the Roller Rig (both controlled and uncontrolled), along with the measurable outputs, have been discussed.

**Chapter 5** discusses the steps of data post-processing and data analysis for an experimental study consisting of a large number of experiments. A description of the correlation analysis, normalized creep force computation, and steps in the generation of the creep-creepage curves are also discussed.

**Chapter 6** discusses the testing results obtained from experimental studies conducted on the VT – FRA Roller Rig. Various tests involving varying the angle of attack, the wheel and rail surface lubricity condition (i.e., wet vs. dry rail), and the wheel wear are performed to study their effects on wheel-rail contact mechanics and dynamics.

**Chapter 7** summarizes the study performed on the Roller Rig and proposes a list of potential projects that can be realized on the Roller Rig.

## Chapter 2. Background

The Virginia Tech-Federal Railroad Administration (VT-FRA) Roller Rig testing facility provides a controlled laboratory environment for performing contact mechanics and dynamic studies on a single wheel-rail pair in a vertical configuration.

Roller rigs have been built worldwide to research rail vehicle dynamics, and they have applications towards the development of high-speed trains. Scaled roller rigs have many advantages over full-size rigs because they are more affordable and controllable.

The creep models of Kalker and Johnson and Vermeulen were used to establish the correction factors, scaling factors, and the resulting transformation factors in order to relate the results from a scaled rig to that of a tangent track. The correction factors for quantities, such as normalized creep forces, are a ratio between results obtained from tangent track and a full-scale roller rig. The scaling factors come into play to relate results from a full-scale roller rig to a scaled-down roller rig. The transformation factors are derived from the correction factors and scaling factors to relate the results from a scaled-down roller rig to a tangent track [1]. Careful attention needs to be paid for determining the overall transformation strategy for a given wheel-rail geometry and scaling ratio.

INRETS scaling strategy allows for the study of wheel-rail contact forces. This scaling strategy is based on the similarity of stresses everywhere in the system (that is, the stress scaling factor is 1), including contact patch and elastic components. It ensures identical correction factors for creep forces versus creepage curves for a full-scale and scaled rig. It is true under Kalker's and Johnson and Vermeulen's theories. This strategy is primarily used for designing roller rigs for studying wheel-rail contact mechanics [2-4].

Researchers at the Railway Technologies Laboratory conducted a separate study in the past to determine the most suitable scaling strategy for the Rig. An INRETS similitude formulation was chosen based on the primary purpose of the VT – FRA Roller Rig, which was to evaluate the contact mechanics at the wheel-rail interface in a dynamic, controlled and consistent manner. A length scaling factor of four was chosen for the Rig, and the scaling factor for other quantities was developed based on this factor. The scaling factor of four was decided upon after discussions with suppliers and rail experts, careful consideration of available components in the market, and after conducting many design calculations. The final scaling results are listed in Table 2-1 [4, 5].

**Table 2-1** Scaling factors for the physical quantities of the Rig [4, 5]

Physical Quantity	Symbol	Scaling Factor
Length	$\square_l$	4
Time	$\square_t$	4
Density	$\square_\rho$	1
Area	$\square_A$	16
Force	$\square_F$	16
Velocity	$\square_v$	1

Acceleration	$\square_a$	$\frac{1}{4}$
Stiffness	$\square_c$	4
Frequency	$\square_f$	$\frac{1}{4}$
Mass	$\square_m$	64
Friction Coefficient	$\square_\mu$	1

## 2.1 Rolling Contact Mechanics

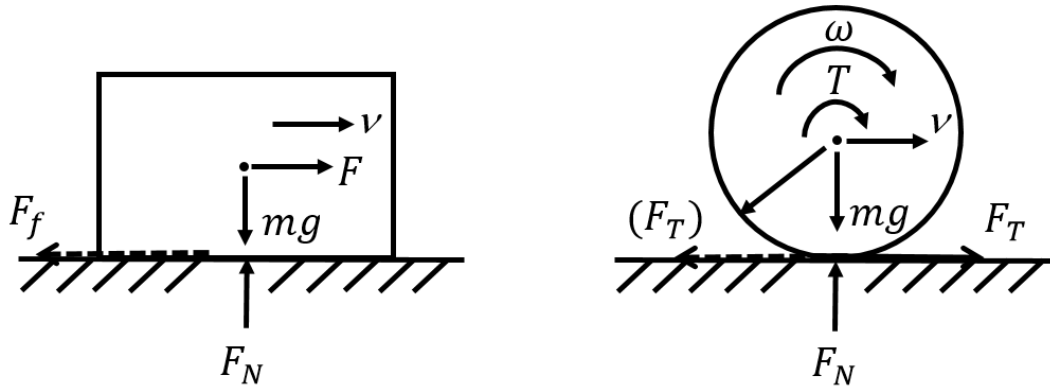
The history of rolling contact mechanics describing the phenomenon at the wheel-rail interface is an integrated part of contact mechanics. Problems involving wheel-rail contact, such as damage phenomenon and contact patch force distribution on vehicle stability, have been investigated since the middle of the 19<sup>th</sup> century. Heinrich Hertz, Frederick William Carter, Hans Fromm, Joost Kalker and Ken Johnson were the key contributors to this research and have laid the scientific foundation for pushing the boundaries of research in rolling contact mechanics with application to railroads [6].

Figure 2-1 shows a graphical representation of sliding contact vs rolling contact, illustrating the difference between adhesion and friction. Adhesion in the railroad community refers to the tangential force generated at the wheel-rail interface, while friction is defined as the resistance encountered by one body moving over another body [7, 8]. In Figure 2-1 (left), a block of mass,  $m$ , is subjected to a force,  $F$ . A frictional force,  $F_f$ , opposes the motion of the block. The static friction force is equal to the horizontal force required to initiate sliding, while the kinetic friction force is equal to the horizontal force required to continue sliding [8]. The ratio between friction force and normal force is called friction coefficient, as shown in Equation (1). In the case for pre-sliding, the friction force is studied at the microscopic level based on the interaction and deformation of the microscopic asperities at the contact and the adhesion forces between the two sliding bodies [7].

$$\mu_f = \frac{F_f}{F_N} \quad (1)$$

Figure 2-1 (right), shows a cylinder rolling along a stationary plane surface, which is analogous to a locomotive wheel rotating on a rail [9]. The wheel is subjected to a normal force,  $F_N$ , which travels along a rail with tangential velocity,  $v$ . During acceleration, the traction motors apply a positive torque,  $T$ , about the center of rotation of the wheel, which maintains an angular velocity,  $\omega$ , causing a reactive tangential force,  $F_T$ , at the wheel-rail interface. During deceleration, the tangential force acts opposite to the running direction of the locomotive. This tangential force during acceleration or deceleration is called adhesion. The ratio between adhesion force and the normal force, defined for a particular set of boundary conditions, is known as adhesion coefficient [10].

$$\mu_a = \frac{F_T}{F_N} \quad (2)$$



**Figure 2-1** Pure sliding contact (left) versus rolling contact during acceleration (right) [9]

### 2.1.1 Normal Contact Problem

Rail vehicles are supported, steered, accelerated, and decelerated by contact forces acting at the wheel-rail interface in an extremely small area (around  $1 \text{ cm}^2$ ). In order to study the behavior of these complex forces, certain contact patch parameters need to be determined: contact surface, pressure, and tangential forces [10, 11].

1. Normal problem, which deals with Hertzian and non-Hertzian contact models, is to find the stresses and deformation when two curved elastic bodies are brought into contact.
2. Tangential problem deals with the creep forces that are dependent on the relative speed between the wheel and rail, more commonly known in the railroad community as creepage.

Hertzian contact theory demonstrates that when dealing with two elastic bodies with large curvature radius compared to contact size, if there is constant curvature inside the contact patch in semi-infinite spaces, then the contact surface is a flat ellipse with semi-ellipsoidal contact pressure distribution. Figure 2-2 shows an example of two curved elastic bodies in contact with contact patch parameters defined by Hertzian contact theory [11].

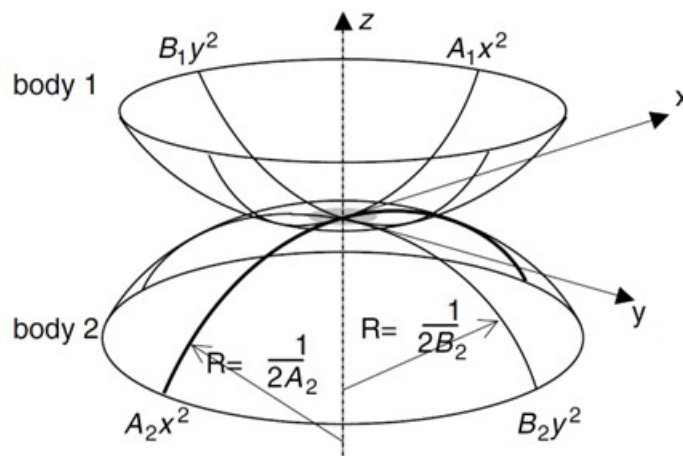


**Figure 2-2** General case of Hertzian contact [11]

For the above case, the mean pressure and maximum pressure at the elliptical contact patch are given by:

$$\sigma_{mean} = \frac{F_z}{\pi * a * b} \quad (3)$$

$$\sigma_{max} = 1.5 * \frac{F_z}{\pi * a * b} \quad (4)$$

### 2.1.2 Tangential Contact Problem

The tangential contact problem deals with finding the tangential forces for contact between the wheel and rail. It is different from a sliding friction Coulomb model, where the traction or braking force will be a function of Coulomb's friction coefficient and normal force. This necessitates the development of rolling contact theories, which can be used to obtain a deeper understanding of design of braking and traction control systems, prediction of wheel and rail wear, and evaluation of ride safety and comfort [12, 13].

During acceleration or while maintaining a constant speed due to the inertia of the wheel and vehicle, the tangential velocity at the wheel surface,  $\omega r$ , will always be greater than the vehicle's velocity,  $v$ . This difference between the tangential velocity of the wheel,  $\omega r$ , and the vehicle's velocity,  $v$ , is known as creep rate or creepage, usually expressed as a percentage, as depicted in Equation (5) [9]:

$$\varepsilon = \frac{v - \omega r}{\frac{1}{2} * (v + \omega r)} \quad (5)$$

where  $\varepsilon$  = longitudinal creepage between the wheel and rail expressed as a percentage. Equation (5) can be rewritten by normalizing the differential tangential velocity at the contact patch by the locomotive's velocity,  $v$ , assuming small creep rate [11].

The need to study the influence of creepage on the adhesion coefficient between the wheel and rail is important as it is fundamentally related to the locomotive adhesion, braking, railcar steering characteristics, curving forces, wheel and rail wear, Rolling Contact Fatigue (RCF), thermal defects, noise, squealing and corrugation. Longitudinal creep force and tangential forces arise due to slip that occurs in the trailing region of the contact patch. Longitudinal creepage ( $\varepsilon$ ) at the contact patch of a locomotive can be positive (during traction) or negative (during braking) [12, 14].

Figure 2-3 shows a typical a creep-creepage curve showing the adhesion coefficient as a function of the creep rate at the contact patch for a dry wheel-rail pair. This curve is also known as the traction versus slip curve. Figure 2-3 shows a linear region of the curve which is observed in the micro-slip region (creepage < 1 %). After this point, the curve saturates when it reaches the point of maximum adhesion, known as adhesion maximum, around 1-2 % creepage. At this point, the adhesion equals the friction force identical to the wheel and roller in pure sliding contact under

identical contact conditions. Figure 2-3 also shows the stick and slip regions. At 0 % creepage, the motion of wheel on rail is pure rolling contact, resulting in stick-type contact. As the creepage increases, the slip region increases at the expense of the stick region and the stick region disappears completely at adhesion maximum [12]. The maximum level of tangential force depends on the capacity of the contact patch to absorb the adhesion, which is expressed in the form of coefficient of friction [8]. Since part of the friction coefficient is utilized by the lateral and spin forces and is due to the fact that the load is not distributed equally at each axle and wheel, the maximum adhesion coefficient in the longitudinal direction shown in Figure 2-3 will be less than the total friction coefficient [15].

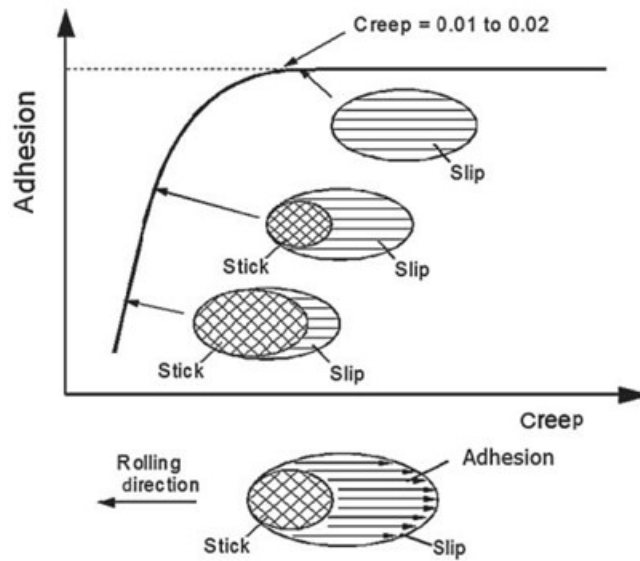


**Figure 2-3** Graph showing adhesion as a function of creep rate at contact patch for dry wheel-rail type contact [8]

The coefficient of friction is a system property rather than a material property. It not only depends on the mating materials, but also on other factors, such as temperature and humidity. The theory of friction is comprehensively discussed in Hutchings [16]. The adhesion between wheel and rail cannot be measured directly although the friction can be measured on the rail surface using measurement techniques, such as a hand-pushed tribometer or a vehicle companion Tribo-Railer [17]. In field measurements, a decreasing section of the creep-creepage curve is observed at high values of longitudinal creepage, which has been attributed to the increasing temperature in the contact area. With increasing creepage at the wheel-rail interface, the temperature in the contact area increases, leading to a decrease in the coefficient of friction. This explanation usually leads to good agreement between theory and measurements for dry and clean surface conditions [18-20].

## 2.2 Brief Description of VT – FRA Roller Rig

The VT – FRA Roller Rig consists of a single wheel-rail pair in a vertical configuration for studying the rolling contact mechanics and dynamics for railroad applications in a 1/4<sup>th</sup> scale

setup. It allows the experimental testing of different wheel-rail dynamics models in a controlled laboratory environment. Different wheel profiles in 1/4<sup>th</sup> scale can be easily mounted and tested on the Rig in a short time duration. A maximum of two wheel profiles can be mounted on the wheel driveline to perform testing and quick comparison of results. The Rig benefits from recent advances in hardware and software, such as high measurement bandwidths, better motion control technologies, and high-resolution encoders. Two high-precision rotary AC servo motors with 20-bit encoder feedback are used to independently power the wheel and roller drivelines. The setup enables independent creepage control at the contact patch in increments as low as 0.01%. Four positioning systems driven by high-precision linear AC servo motors allow for simulating all the different wheel-rail interactions in field testing scenarios, in a more controlled laboratory environment. The linear motors have 32-bit encoder feedback that help simulate the angle of attack, cant angle, lateral displacement, and vertical load within a micron level of accuracy. The Rig has two custom-designed and calibrated load platforms to accurately measure the contact patch forces and moments to within 13.6 N accuracy. The instantaneous torque in each driveline can be measured with less than 6.1 N-m resolution [21-23].

A number of sensors measure the contact patch parameters, including force, torque, displacement, rotation, speed, acceleration, and contact patch geometry. A unified communication protocol between the actuators and sensors minimizes data conversion time, which allows for servo update rates of up to 48 kHz. This high bandwidth allows for vibration analysis that is responsible for wear, noise, and ride discomfort [24]. A vast spectrum of studies can be conducted, such as creep-creepage measurements, evaluation of different third-body layers, wheel-rail wear analysis, and measurement of contact geometry.

This report elaborates on evaluating and validating slip dynamics by means of creep-creepage measurements by simulating different field scenarios. A brief analysis on the effects of “natural” third-body layer is presented in this report.

Figure 2-4 shows the isometric view of the solid model (left) and fully assembled (right) VT – FRA Roller Rig. The red arrows indicate the four degrees of freedom controlled by the six linear actuators. Figure 2-5 shows the front view of the solid model (left) and fully assembled (right) VT – FRA Roller Rig. Figure 2-6 shows the top view of the solid model (left) and fully assembled (right) VT – FRA Roller Rig [21-23].

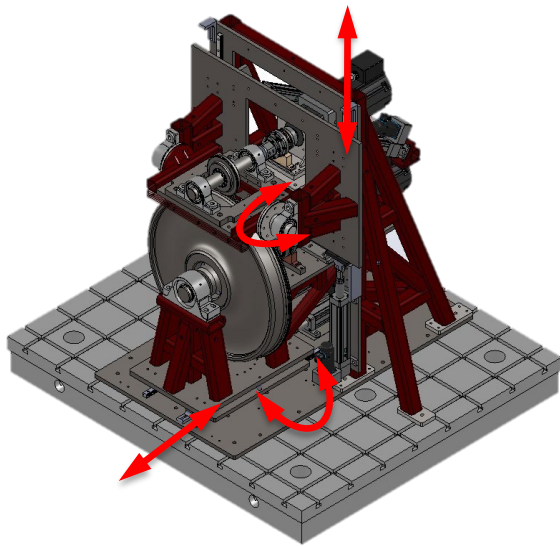


**Figure 2-4** Isometric view of solid model (left), and fully assembled (right) VT – FRA Roller Rig

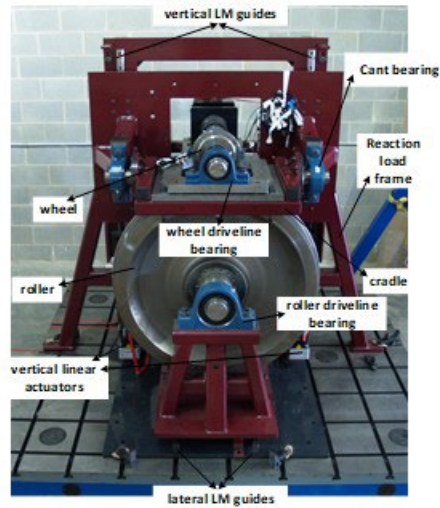
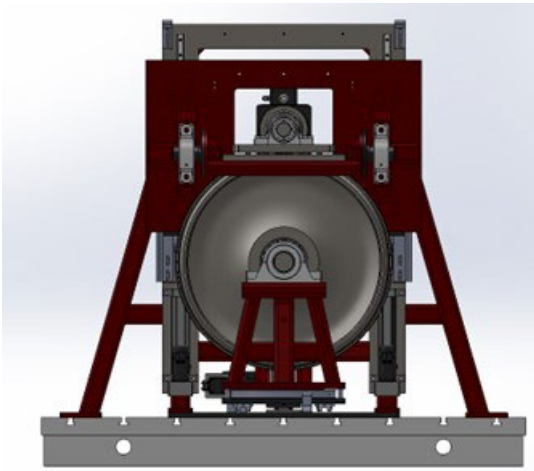


**Figure 2-5** Front view of solid model (left), and fully assembled (right) VT – FRA Roller Rig

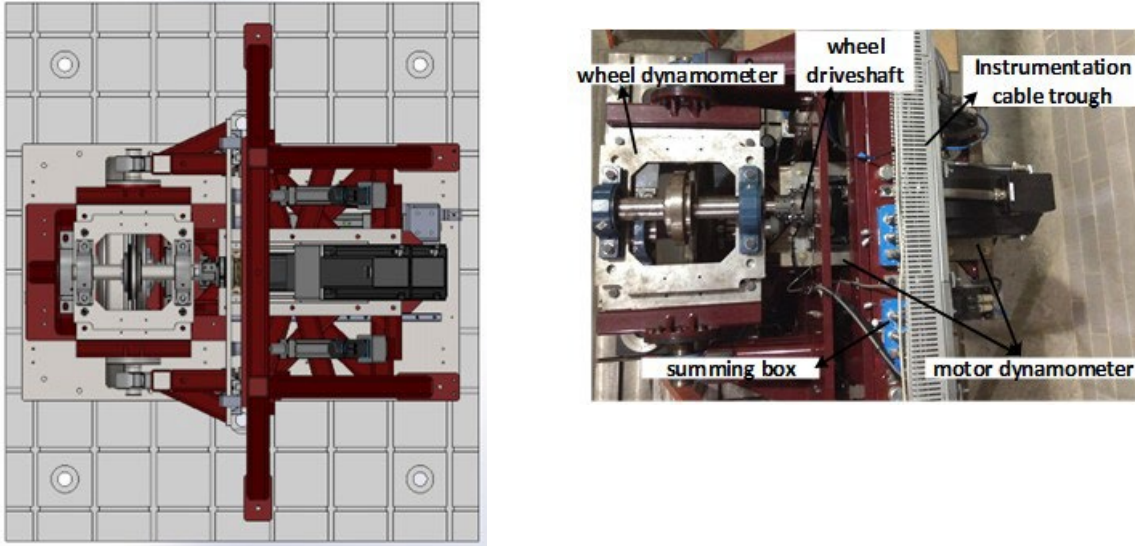


**Figure 2-6** Top view of solid model (left), and fully assembled (right) VT – FRA Roller Rig

### 2.2.1 Data Acquisition and Control Architecture

The Rig’s data acquisition is based on SynqNet technology, which is a digital communication protocol for multi-axis motion control applications. It has been used to interface all the electromechanical components of the Rig: servo drives, motion controllers, and data acquisition units. This eliminates the need for any data conversion between these units, thus maximizing the network bandwidth to 48 kHz. SynqNet has been successfully implemented on the S772 and AKD servo drives, QMP motion controller, and SQIO-SQID data acquisition boards.

The Roller Rig consists of 12 nodes which communicate with each other through the SynqNet network. Each node on the network refers to a component. The nodes are enumerated sequentially according to the wiring order of the network. Table 2-2 lists the 12 nodes currently used by the Roller Rig, with connected components, Degrees of Freedom (DOF) controlled, and their corresponding axes number and motor number. Axes 4 and 5 are mapped to control the vertical displacement of the wheel cradle and are responsible for loading the wheel on to the roller. Axes 6 and 7 are mapped to control the cant angle to simulate the superelevation when a train negotiates a curve. Thus, two motors are mapped to control a single axis, thus making it a gantry configuration with an aim to obtain independent and slow-fine motion of vertical displacement and cant angle.

**Table 2-2** 12 nodes currently used by the Roller Rig, with connected components, DOFs controlled, and their corresponding axes number and motor number shown [21]

Node Number	Connected Components	Degrees of Freedom	Axis Number	Motor Number
1	S772 digital servo drive, AKM84T servo motor, single-turn EnDat 2.2 absolute sine encoder	Wheel rotation	1	0
2		Roller rotation	2	1

3	AKD digital servo drive, EC4 linear actuator, multi-turn EnDat 2.2 absolute sine encoder	Lateral displacement	3	2
4		Angle of attack	4	3
5		Vertical displacement (standard gantry without yaw axis)	5	4
6				5
7		Cant angle (standard gantry without yaw axis)	6	6
8				7
9	SQIO-SQID data acquisition board	N/A	N/A	N/A
10	SQIO-SQID data acquisition board, SQIO- MIXEDMODULE	N/A	N/A	N/A
11	SQIO-SQID data acquisition board, SQIO- MIXEDMODULE	N/A	N/A	N/A
12	SQIO-SQID data acquisition board	N/A	N/A	N/A

SynqNet supports 64 nodes and 32 bits of configurable I/O per axis. New components can be easily added to the Rig by connecting two RJ45 cables to its adjacent components and refreshing the Roller Rig's Motion Programming Interface (MPI). The control architecture is set up in a ring topology (closed-loop), which has many advantages when compared to a string topology. In case a cable or a node fails, the network will continue to operate and communicate with the other components, while the motion controller will inform the user of the error.

Figure 2-7 shows the control architecture configured for the Roller Rig. The host computer that includes a ZMP-SynqNet card connects to two S772 digital drives in series, then connects to 6 AKD drives in series, then connects to four SQIO-SQID cards in series, and finally connects back to the host computer [5].

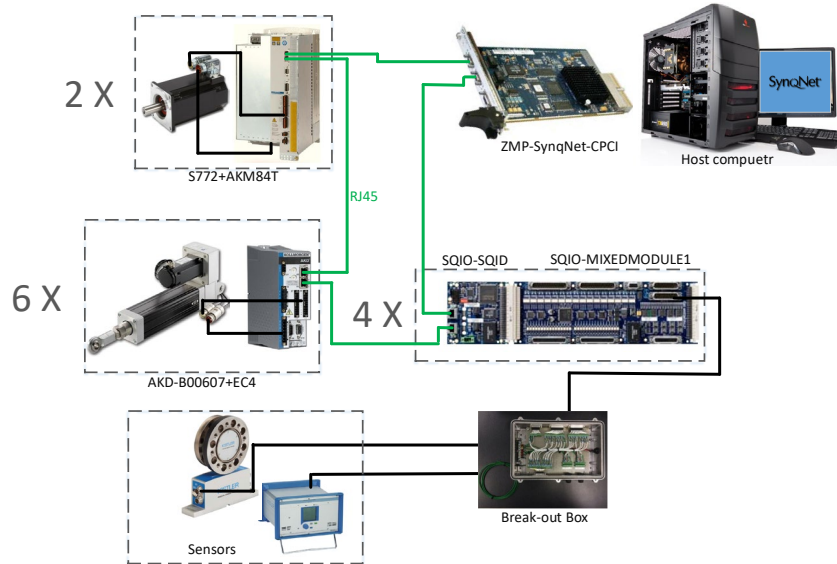


**Figure 2-7** Schematic diagram of the Roller Rig's configured motion architecture [5]

## 2.2.2 Roller Rig's Capabilities

Table 2-3 summarizes the boundary conditions that can be set on the Roller Rig. As can be seen, the capabilities mentioned are far greater than the means currently available to the FRA and rail industry, making the Rig a crucial tool for rail vehicle modeling and engineering analysis of passenger and freight trains.

**Table 2-3** Summary of the Roller Rig's capabilities

Scaling factor	1:4	
Angle of attack (deg.)	± 6	0.1 increments
Cant angle (deg.)	± 6	0.1 increments
Lateral displacement (inch)	± 1	4/1000 increments
Max. velocity (km/h / mph)	16 / 10 (actual)	16 / 10 (simulated)
Max. creep rate (%)	10	0.01 increments
Max. contact forces (per wheel-rail pair)		
Normal load (kN / KIPS)	12 / 2.7 (actual)	192 / 43 (simulated)
Longitudinal force (kN / KIPS)	16 / 3.6 (actual)	256 / 57 (simulated)
Lateral force (kN)	16 / 3.6 (actual)	256 / 57 (simulated)
Max. DAQ bandwidth (kHz)	48	

Controller bandwidth (Hz)	150
---------------------------	-----

Key features that will be useful to railroad industry research are as follows:

- High precision 20-bit encoder feedback for the wheel and roller driveline, with independent position, velocity, acceleration, and jerk control
- Precise positioning systems with 32-bit encoder feedback to command the simulated load, angle of attack, cant angle, and lateral displacement
- Positioning accuracy to within 16 nm of the target location
- Custom made dynamometers for acquiring contact forces and moments with a very fast response to changing loads
- Contact force measurement accuracy to within 40 N of the applied load
- Capability of simulating freight railcar with a maximum of 344 KIPS simulated load
- Capability of simulating braking and traction with creepage resolution as low as 0.1%.
- Unified communication protocol provides an unprecedented servo update rate of 48 kHz
- Easy assembly of the wheel allows for quick testing of different wheel profiles
- Seamlessly embeds SynqNet, MATLAB, C, and XML programming environments with a user-friendly GUI
- When testing under high loads, the maximum allowable creepage value is less than 10%, as shown in Table 2-3, to prevent damage to the roller contact surface under high slippage
- Deflection of the structure under maximum loading is less than 0.1 mm, enabling it to simulate the operating parameters and boundary conditions with a high degree of accuracy

### Chapter 3. Test Setup

The main components of the Roller Rig test setup consist of mechanical and electromechanical components as listed below:

- Scaled wheel and roller in vertical configuration
- Independent wheel and roller drivelines for connecting motors to the wheel and roller, each consisting of shafts, bearings, couplers, gearbox, torque coupling, and torque sensor
- Positioning mechanisms for simulating angle of attack, lateral displacement, cant angle, and normal loads
- Load frame to which all components, including wheel and roller drivelines and positioning systems, are attached
- Base frame to isolate the Rig from external noise and vibration, and to provide a rigid basement to support the weight of the load frame
- Two 3-phase AC servomotors for powering wheel and roller drivelines
- Power electronics that include mains power network, power isolation and filtering, DC power, and DC bus
- Grounding and shielding mechanisms for minimizing electromagnetic noise coupling
- Thermal management systems for maintaining the temperature of the power electronics below standard/manufacturer regulations
- Safety and monitoring circuits that include Safe-Torque-Off, Hardware Enable, Ready-to-Operate, Logic ON-OFF, Emergency Stop, Dynamic Braking, and Holding Brake
- Instrumentation, motion control, and sensory systems including command and feedback network, data acquisition systems, electronic gearing, motion programming interface, and control tower

Details of the mechanical and electromechanical developments for the Roller Rig are available in [21, 23]. Figure 3-1 shows the testing facility (top), mechanical (bottom-left), and electromechanical (bottom-right) components of the Roller Rig.



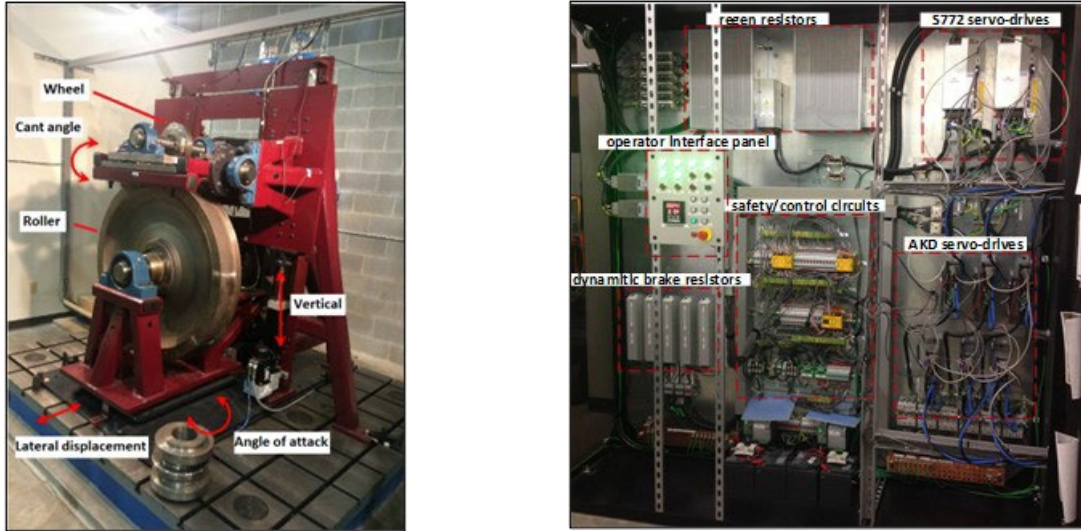


**Figure 3-1** Overview of VT – FRA Roller Rig testing facility (top); isometric view of the Roller Rig with rotary and linear positioning systems indicated (bottom-left); enclosure for the control tower of Roller Rig including S700 drives, AKD drives, safety/control circuits, regenerative and dynamic brake resistors and operator interface panel (bottom-right) [21, 23]

The Roller Rig’s coordinate system is the same as the contact coordinate system commonly used in the railroad industry. Both the local and global coordinate systems are denoted by the following nomenclature:

- $F_z$ : normal direction
- $F_x$ : longitudinal direction
- $F_y$ : lateral direction

Figure 3-2 illustrates the above-mentioned coordinate system as applied to the Roller Rig.

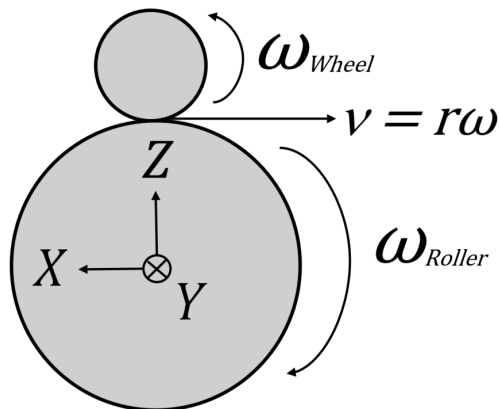


**Figure 3-2** Contact coordinate system for the Roller Rig

### 3.1 Measuring Creep Forces and Moments at the Wheel-Rail Contact

The main purpose of the Rig is to conduct contact mechanics studies to evaluate the creep forces and moments at the contact patch. A novel force measurement system was designed, fabricated, and calibrated at the Railway Technologies Laboratory (RTL) with an aim to measure the contact patch forces ( $F_x, F_y, F_z$ ) and spin moments ( $M_x, M_y, M_z$ ) with a high degree of precision and accuracy. The VT – FRA Roller Rig consists of two load platforms. The primary load platform is placed in-line with the wheel-roller contact patch, and measures forces for the primary load path of the Rig. The secondary load platform is placed below the wheel traction motor casting. It measures any axial force component that goes through the wheel driveline and is reacted at the base of this casting. Figure 3-3 shows the side view and top view of the Rig, with the wheel dynamometer and motor dynamometer indicated.

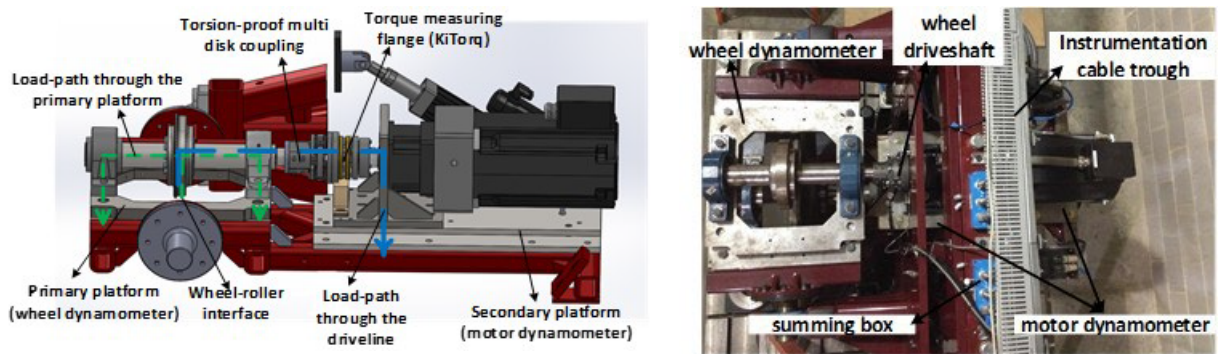


**Figure 3-3** Side view of Rig showing primary and secondary load platforms and load paths (left); top view of Rig showing wheel and motor dynamometers after being installed on the Rig (right) [21-23]

The motor dynamometer is interfaced with SQIO-SQIO data acquisition board 1, and the wheel dynamometer is interfaced with SQIO-SQIO data acquisition board 2 in the Roller Rig’s SynqNet network.

Each dynamometer consists of four tri-axial load cells placed in each corner of the rectangular load platform. Each tri-axial load cell is a quartz force sensor that works based on piezoelectric principles. Mechanical compression due to application of force leads to generation of a proportional electrostatic charge. This charge is picked up by the built-in electrodes and transferred to the corresponding connector. These load cells are capable of making both dynamic and quasi-static measurements. The electrostatic measurement signals for the four sensors in each dynamometer are summed up using a summing box to reduce the outputs from 12 to 8.

Figure 3-4 (left) shows the primary load platform (wheel dynamometer) mounted on the Roller Rig, and in plane with the wheel-rail contact patch. Figure 3-4 (right) shows a diagram of the primary load platform with the four piezoelectric load cells on each corner of the platform. The direction of contact patch forces and moments has also been indicated.

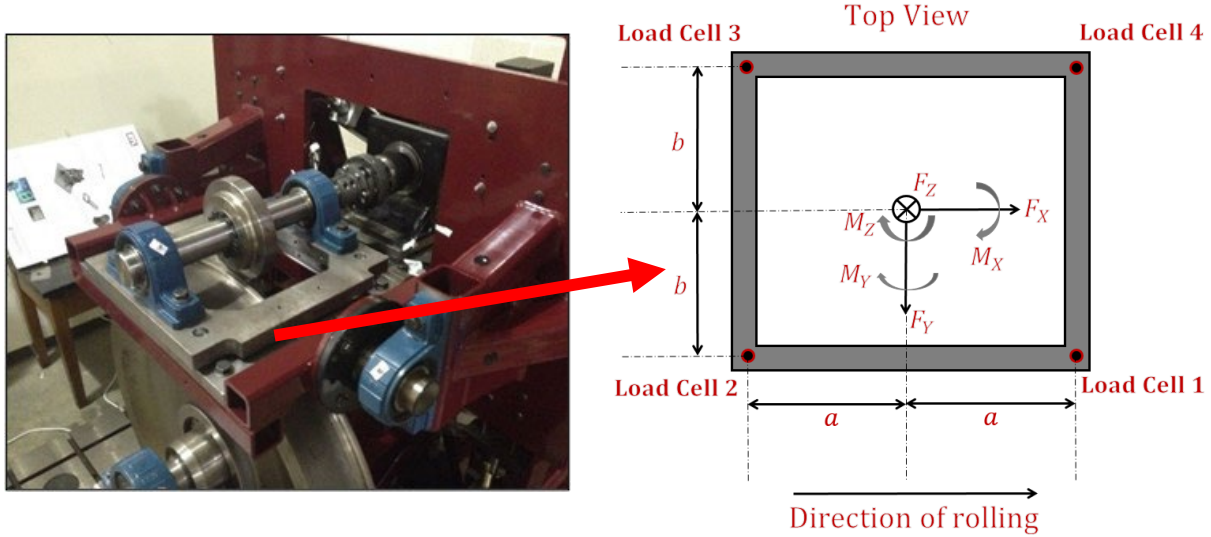


**Figure 3-4** Primary load platform mounted on the Roller Rig (left); diagram of primary load platform, mounted with four 6-component piezoelectric load cells on each corner (right)

The forces at the wheel-rail interface are calculated from the relations

$$\begin{aligned}
 F_x &= F_{x_{1+2}} + F_{x_{3+4}} \\
 F_y &= F_{y_{1+4}} + F_{y_{2+3}} \\
 F_z &= F_{z_1} + F_{z_2} + F_{z_3} + F_{z_4}
 \end{aligned} \tag{6}$$

The contact patch moments are calculated from the measured forces and distances of the load cells from the center of the contact patch, given by the relations

$$\begin{aligned}
 M_x &= b * (F_{z_1} + F_{z_2} - F_{z_3} - F_{z_4}) \\
 M_y &= a * (-F_{z_1} + F_{z_2} + F_{z_3} - F_{z_4}) \\
 M_z &= b * (-F_{x_{1+2}} + F_{x_{3+4}}) + a * (F_{y_{1+4}} - F_{y_{2+3}})
 \end{aligned} \tag{7}$$

The multichannel charge amplifier then converts and amplifies these charges into  $\pm 10$  VDC fourteen signals, as shown in Table 3-1 and Table 3-2 [25, 26]. These signals then go to the break-out boxes and through the SQIO-MIXEDMODULE units and are finally recorded to the host computer from Motion Scope. Table 3-1 and Table 3-2 also show the corresponding nodes, SynqNet components, and SynqNet Analog Inputs (AIN) for the motor dynamometer and wheel dynamometer, respectively, for all 14 signals.

**Table 3-1** List of AIN channel numbers for mapping all forces and moments from motor dynamometer to Motion Scope

Signal from Charge Amp #1	SynqNet Component	SynqNet Node	Correct SynqNet I/O
---------------------------	-------------------	--------------	---------------------

$F_{(x1+x2)}$	MIXEDMODULE #1 P2	10	AIN 0
$F_{(x3+x4)}$	MIXEDMODULE #1 P2	10	AIN 1
$F_{(y1+y4)}$	MIXEDMODULE #1 P2	10	AIN 2
$F_{(y2+y3)}$	MIXEDMODULE #1 P2	10	AIN 3
$F_{z1}$	MIXEDMODULE #1 P2	10	AIN 4
$F_{z2}$	MIXEDMODULE #1 P2	10	AIN 5
$F_{z3}$	MIXEDMODULE #1 P2	10	AIN 6
$F_{z4}$	MIXEDMODULE #1 P2	10	AIN 7
Sum $F_x$	MIXEDMODULE #1 P3	10	AIN 8
Sum $F_y$	MIXEDMODULE #1 P3	10	AIN 9
Sum $F_z$	MIXEDMODULE #1 P3	10	AIN 10
$M_x$	MIXEDMODULE #1 P3	10	AIN 11
$M_y$	MIXEDMODULE #1 P3	10	AIN 12
$M_z$	MIXEDMODULE #1 P3	10	AIN 13

**Table 3-2** List of AIN channel numbers for mapping all forces and moments from wheel dynamometer to Motion Scope

Signal from Charge Amp #2	SynqNet Component	SynqNet Node	Correct SynqNet I/O
$F_{(x1+x2)}$	MIXEDMODULE #2 P3	11	AIN 0
$F_{(x3+x4)}$	MIXEDMODULE #2 P3	11	AIN 1
$F_{(y1+y4)}$	MIXEDMODULE #2 P3	11	AIN 2
$F_{(y2+y3)}$	MIXEDMODULE #2 P3	11	AIN 3
$F_{z1}$	MIXEDMODULE #2 P3	11	AIN 4
$F_{z2}$	MIXEDMODULE #2 P3	11	AIN 5
$F_{z3}$	MIXEDMODULE #2 P3	11	AIN 6

F <sub>Z4</sub>	MIXEDMODULE #2 P3	11	AIN 7
Sum F <sub>x</sub>	MIXEDMODULE #2 P2	11	AIN 8
Sum F <sub>y</sub>	MIXEDMODULE #2 P2	11	AIN 9
Sum F <sub>z</sub>	MIXEDMODULE #2 P2	11	AIN 10
M <sub>x</sub>	MIXEDMODULE #2 P2	11	AIN 11
M <sub>y</sub>	MIXEDMODULE #2 P2	11	AIN 12
M <sub>z</sub>	MIXEDMODULE #2 P2	11	AIN 13

### 3.1.1.1 Operational Modes for Multichannel Charge Amplifier

The charge amplifier consists of a high gain and highly insulated operational amplifier with the capacitor,  $C_g$ , connected in negative feedback. As a result of the very high gain,  $U_d$ , is reduced almost to zero. The high input resistance is maintained. Resistance,  $R_g$ , in the negative feedback branch determines the lower cut-off frequency of the charge amplifier, thus making this a high pass filter. Figure 3-5 shows a time constant resistor,  $R_g$ , which can be switched in parallel with the range capacitor,  $C_g$ . The lower cut-off frequency of the charge amplifier is determined by the resistance,  $R_g$ , in the negative feedback branch. Two modes of operation of the charge amplifier are possible, depending on the value of the resistance,  $R_g$ , as follows:

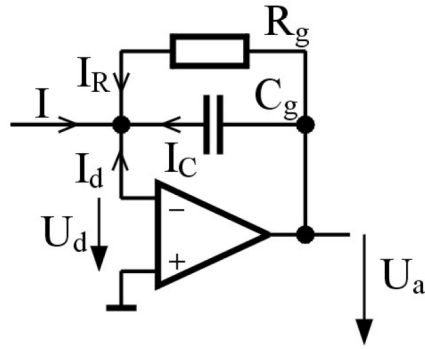
- DC (long) mode
- Short mode

The DC (long) mode has the lowest possible cut-off frequency and hence the longest time constant. As a result, the parallel resistance,  $R_g$ , consists only of the insulation resistance of the range capacitor,  $C_g$ . The corresponding time constant value amounts to anywhere between 10,000 – 100,000 s in practice. This mode is selected when taking quasi-static measurements. The short mode has the highest possible cut-off frequency and the shortest time constant, resulting in time constants of 220 s in practice. In this case, the time constant resistor,  $R_g$ , has a value of  $10^{10} \Omega$  which is switched in parallel with the relevant range capacitor,  $C_g$ , as shown in Figure 3-5. It is useful for capturing high-frequency content, such as analyzing the effects of wheel-rail vibrations under high angle of attack and flanging conditions, or analyzing the rocking dynamics phenomenon [27].

Equation (8) is used for calculating the cut-off frequency for the DC (long) mode and short mode of the Kistler charge amplifier.

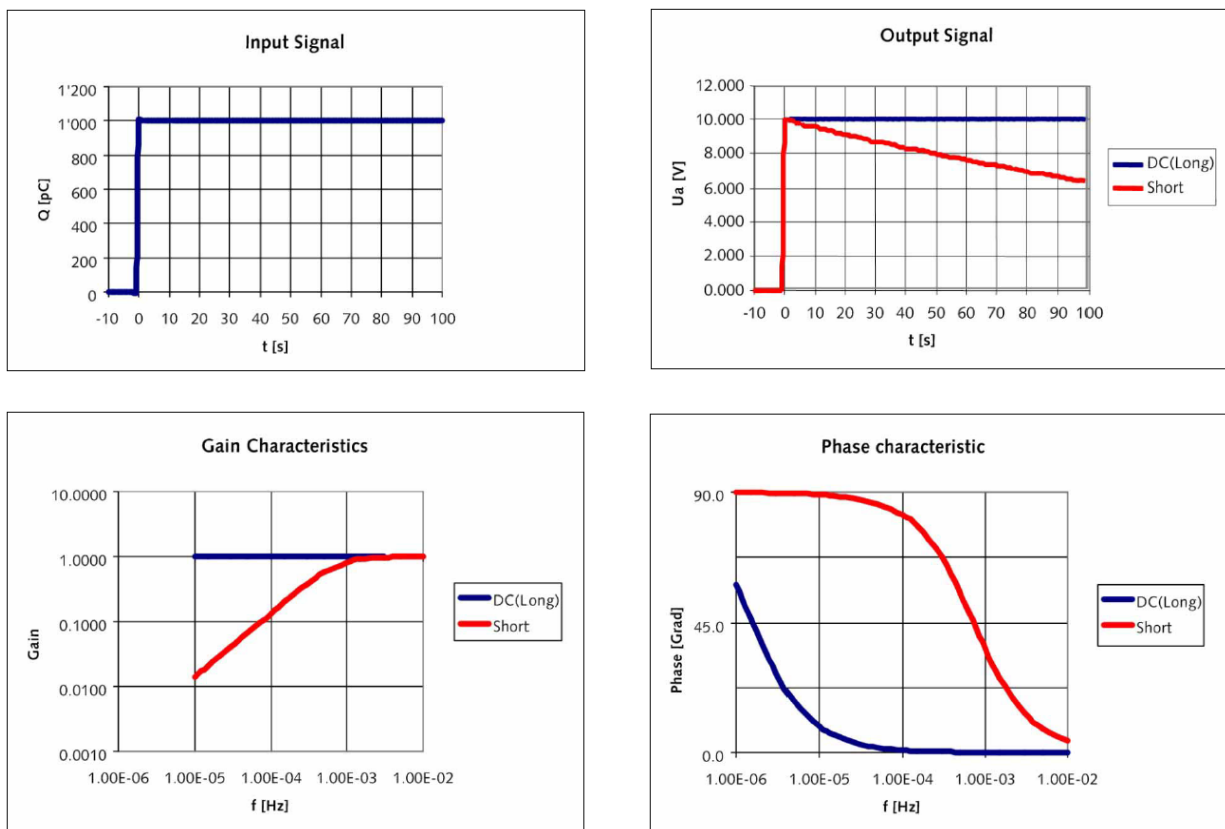
$$f_u = \frac{1}{2 * \pi * R_g * C_g} \quad (8)$$

where  $R_g$  is the time constant, and  $C_g$  is the range capacitance.



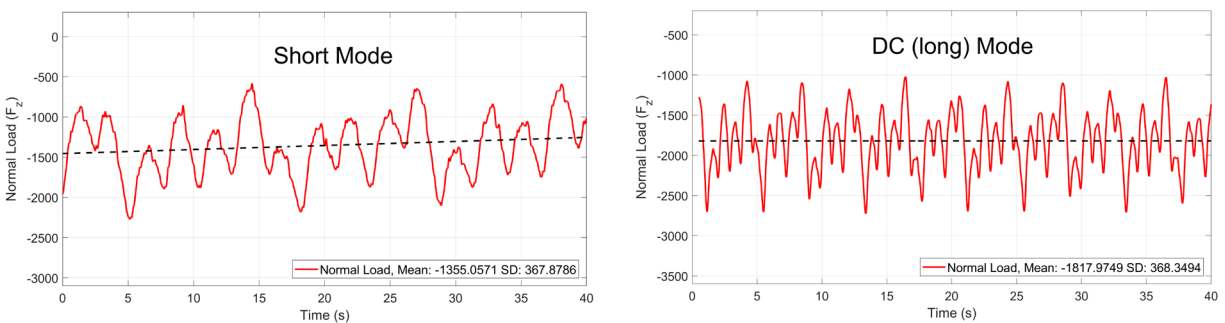
**Figure 3-5** High-pass filter circuit diagram inside the Kistler charge amplifiers [27]

Figure 3-6 shows the step response, amplitude, and phase response curves of the charge amplifier at low frequencies. It can be seen from the gain plot that the -3 dB point, which represents the cut-off frequency of the high-pass filter, is around 0.001 Hz. A phase change of 90° is observed at the cut-off frequency due to the presence of a pole at that frequency. The Kistler charge amplifiers also allow for adjusting the analog second order low-pass filter characteristics.



**Figure 3-6** Step response (top), and gain and phase responses (bottom) of Kistler charge amplifier at low frequencies for DC (long) mode and short mode measuring modes of operation [27]

Careful attention needs to be given when choosing the operational mode of the Kistler charge amplifier. Figure 3-7 shows normal load measurements taken from the Rig when the wheel and roller are in contact, for short mode and DC (long) mode of the Kistler charge amplifier. Each of these experiments was performed for a duration of 40 seconds and for different linear speeds. The normal load data was low-pass filtered using a digital second order Butterworth filter at 10 Hz break frequency, in order to eliminate all of the high frequency noise in the data. The filtering was performed using a zero phase distortion method, using the “filtfilt” function in MATLAB software, which makes the equivalent filter a fourth order filter. The black dotted line in Figure 3-7 indicates the trend of the data with the short mode clearly showing a drift in the measurements towards zero. Both measurements reported in Figure 3-7 are conducted in quasi-static conditions, that is, the testing conditions are kept constant for the entire duration of the test. Quasi-static testing conditions are used for results reported in this report and hence, DC (long) mode of charge amplifiers are used to capture the forces for the experimental testing. The short mode can be used for dynamic testing in order to precisely capture high frequency content between wheel-rail contact. An analysis for the cause of trends in normal load data is given in Section 3.1.2.2.



**Figure 3-7** Measurements in short mode of Kistler charge amplifier showing piezoelectric sensor drift in normal load (left), and measurements in DC (long) mode of Kistler charge amplifier with no piezoelectric sensor drift (right)

### 3.1.2 Overview of Different Control Algorithms for Motion Control

Each axis of the Roller Rig is controlled using a QMP-SynqNet-GB-PCie-RJ motion controller, which performs real time trajectory calculations, closed-loop control, handles the dedicated I/O, updates status, event messages, data recording, SynqNet network data processing, and many other features. This controller, along with Mechaware Matlab/Simulink plugin, allows the user to define and design custom control algorithms (control laws).

The controller algorithms can be operated using either PID or PIV (Proportional-Integral-Velocity) feedback control loops. PID is a control algorithm based on position error and is commonly used in the industry for motion control applications. On the other hand, the PIV control algorithm uses position error and velocity error (calculated by differentiating position). It consists of an inner velocity loop and an outer position loop. The inner velocity loop must be tuned first before the outer position loop can be tuned. The PIV control algorithm performs better than a PID control algorithm based on its additional velocity control, which is missing in a PID control algorithm. It is considered for controlling the rotary axis of the wheel and roller driveline. However, with a high bandwidth of the position control loop of servo motors and linear actuators, the PID algorithm is

able to regulate the input velocity and position trajectories with less than 1% error. As a result, it is chosen as the preferred option to avoid tuning the extra parameters of a PIV control loop. As a result, the creepage at the wheel-rail contact is being controlled to a very high degree of precision, which is of paramount importance for creep-creepage studies presented in this current research. Below is an overview of the different control algorithms for controlling the servo motors and linear actuators that are part of the powertrain and positioning systems of the Rig.

### 3.1.2.1 Position Control (PC) Mode

A simple PID control algorithm is used to regulate the position of the linear actuators in Torque mode. A schematic of the PC mode control algorithm is shown in Figure 3-8. The algorithm uses feedback from the encoders to regulate the position. Feedforward gains are also used to make the controller's performance more aggressive by increasing its bandwidth.

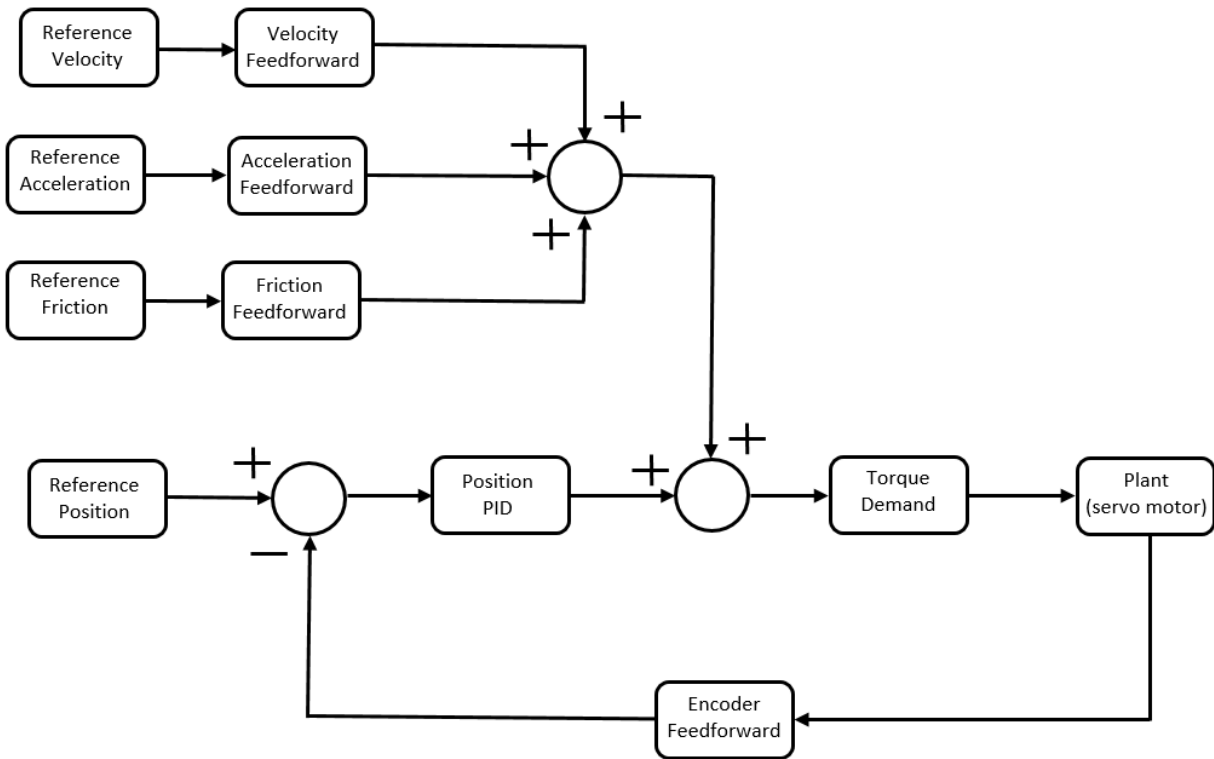


**Figure 3-8** Block diagram showing Position Control (PC) mode for non-gantry axis of the Roller Rig

### 3.1.2.2 Need for Force Control (FC) Mode

The Roller Rig is designed to control the boundary conditions to a very high degree of precision in order to provide the ability to measure the contact patch forces with high accuracy and repeatability. The error for the normal load ( $F_z$ ) obtained using PC mode on the vertical positioning system is  $\pm 35\%$  of the mean normal load ( $F_z$ ). A review of the current roller rigs

around the world showed a measurement error for normal load ( $F_z$ ) to be  $\pm 50\%$  of the mean. In order to push the boundaries of force measurement accuracy even further, a need was identified for developing a FC algorithm using force feedback from the two load platforms in order to minimize the standard deviation in the normal load data.

The need for developing a novel FC algorithm using feedback from the two load platforms for the linear actuators controlling the normal load ( $F_z$ ) is listed below:

1. In PC mode, the normal load ( $F_z$ ) between the wheel and roller cannot be directly controlled. Instead, the position of the linear actuators is changed incrementally by the engineer until the pre-determined normal load ( $F_z$ ) is achieved.
2. The current low frequency oscillations observed in the raw normal load data are an artifact of the PC mode, as explained in this section. After the pre-determined normal load ( $F_z$ ) is achieved, the center distance between the wheel and roller is fixed. Small radial run-outs are present in the wheel and roller due to machining tolerances. Continuous wear and plastic deformations on the wheel and roller due to continuous testing on the Rig also contribute to the radial run-outs. Also, absolute alignment is impossible and a small degree of error will always be present. Figure 3-9 shows the wheel and roller represented as ellipses, in order to stress the fact that the nominal radius at the point of contact is not the same because of the above-mentioned imperfections. Finally, the high stiffness of steel-on-steel contact, along with small surface imperfections and fixed center distance between the wheel and roller during a test, lead to a high spread of data around the mean measured normal loads ( $F_z$ ).
- 3.

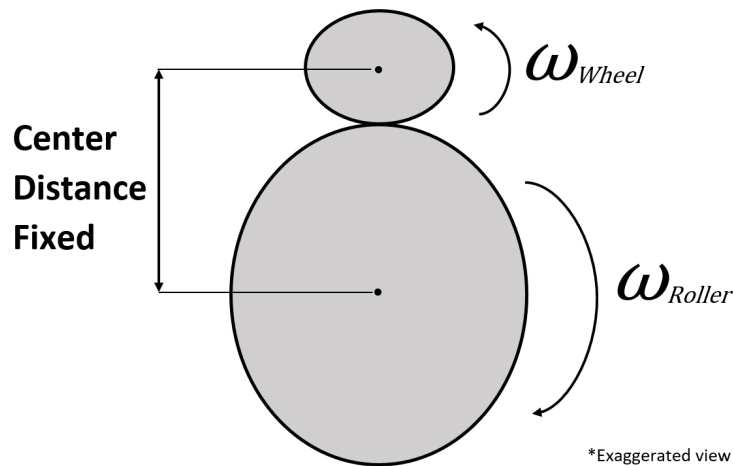


**Figure 3-9** Surface imperfections and alignment tolerances resulting in radial run-out of wheel and roller

Figure 3-10 (top) shows the normal load oscillations of  $\pm 500$  N about the mean value, due to the above-mentioned constraints at the contact patch. The normal load data is low-pass filtered using a digital second order Butterworth filter at 10 Hz break frequency in order to eliminate all of the high frequency noise in the data. The filtering is performed using a zero phase distortion method, using the “filtfilt” function in MATLAB software, which makes the equivalent filter a fourth order filter. The roller diameter is  $\sim 4.62$  times the wheel diameter. As a result, the roller diameter is not an integer multiple of the wheel diameter.

Therefore, for every one rotation of the roller, the initial positions of the wheel and roller do not coincide and are separated by a finite distance. This results in a “phase shift” in the data. Figure 3-10 (top) shows normal load data collected for a linear speed of 3 km/h and zero creepage between the wheel and roller. Figure 3-10 (bottom) shows the wheel and roller time periods superimposed as rectangular boxes on the normal load time series data. The wheel time period is represented in yellow rectangular boxes, and the roller time period as red rectangular boxes. Comparing the second and seventh rotation of the wheel highlighted in yellow shows a “phase shift” in the data, which is caused by roller diameter not being an integer multiple of wheel diameter.

Another analysis is carried out to show that the normal load trend in the data is a function of wheel and roller rotational frequency. A Discrete Fourier Transform (DFT) is conducted using the Fast Fourier Transform (FFT) to calculate the Power Spectral Density (PSD) of the normal load data shown in Figure 3-10 (top). The wheel has a rotational frequency of  $\sim 1.15$  Hz and the roller has a rotational frequency of  $\sim 0.25$  Hz. Figure 3-11 shows the PSD of the normal load data. It is observed that the wheel and roller rotational frequencies, along with their harmonics, feature prominently as peaks in the spectral plot. These peaks are higher than the other peaks by a factor of 10 in the dB scale. This confirms that the periodicity in normal load data is composed of harmonic elements of wheel and roller rotational frequencies.

4. Potential to reduce force error to  $\pm 5\%$  of the mean commanded normal loads ( $F_z$ ) by rejecting force disturbances due to rolling contact
5. Command force trajectory inputs instead of current position inputs
6. Ability to perform scientific studies, such as analyzing hunting dynamics, flange contact, wheel climb, and derailment

A cascaded force-position control loop is currently being simulated, tested, and calibrated on the Roller Rig. The PC configuration uses feedback from the shaft encoders on the linear actuators to regulate position. The FC loop consists of the current inner position loop and an outer force control loop that takes feedback from the two load platforms to regulate/track a commanded force trajectory.

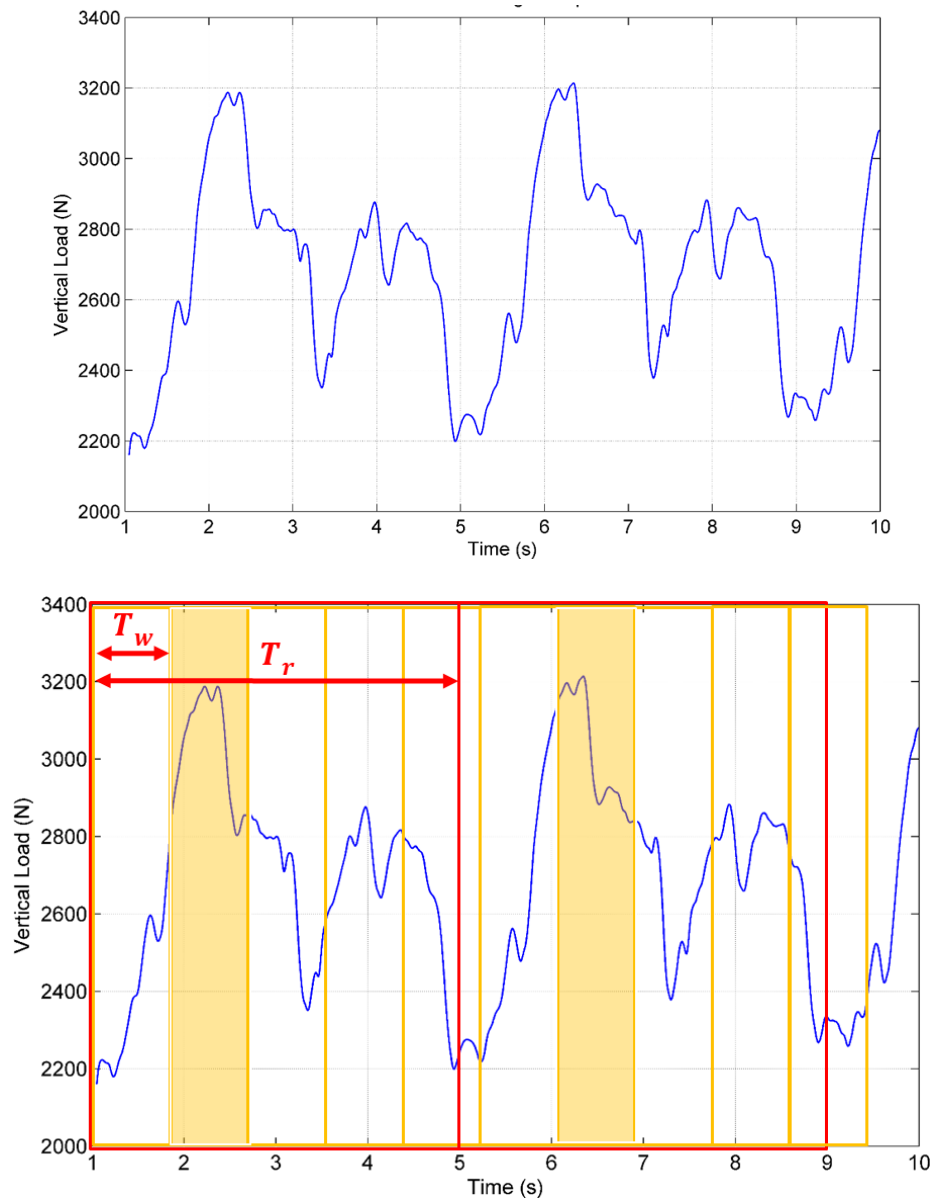


**Figure 3-10** Normal load oscillations at wheel-rail contact patch without creepage (top), and superimposed wheel and roller time periods on time series plot (bottom)

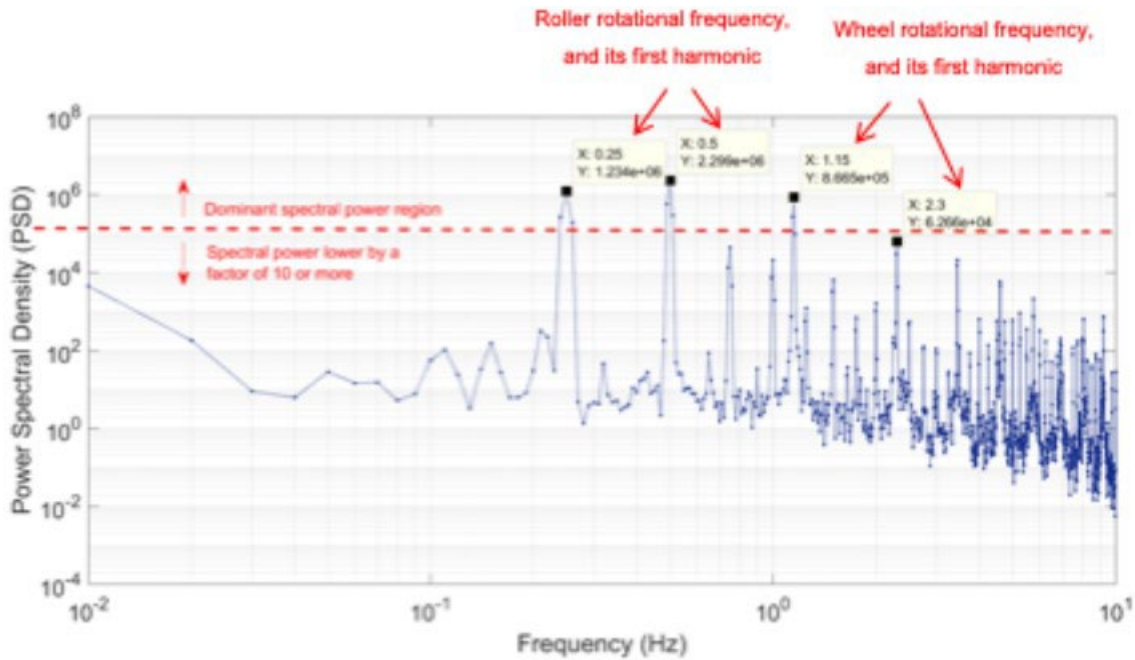


**Figure 3-11** Power Spectral Density (PSD) of normal load data showing dominant peaks at wheel and roller rotational frequencies and their harmonics

### 3.1.3 Control Algorithm for Wheel and Roller Driveline

The wheel and roller have independent drivelines, with the primary purpose of accurately controlling the creepage at the wheel-roller contact patch. A position control feedback loop, as shown in Figure 3-8, is used to tune each of the drivelines. Bode Tool’s auto-tuning feature is used for configuring the PID parameters of the control loop.

### 3.1.4 Control Algorithm for Linear Positioning Systems

The linear positioning systems built as a part of the Rig are used for controlling the vertical load, angle of attack, cant angle, and lateral displacement of the wheel. It can be operated using two different types of controller algorithms, as follows:

- Position Control Mode
- Force Control Mode

#### 3.1.4.1 Angle of Attack (AoA) Positioning System

AoA comes into play for simulating a locomotive negotiating a curve, where the AoA needs to be held constant for the entire duration of the test. Thus, a simple PID control algorithm in position control mode, as shown in Figure 3-8, is used to control the AoA degree of freedom on the Roller Rig.

#### 3.1.4.2 Lateral Axis (Y) Positioning System

Lateral displacement of a wheelset from its mean location on the roller is important for analyzing the distribution of forces at the contact patch during various scenarios, such as hunting oscillation, gauge widening, wheel flange climb, and derailment mechanics. A simple PID control algorithm in position control mode, as shown in Figure 3-8, is used to control the lateral displacement on the Roller Rig.

#### 3.1.4.3 Vertical Axis (Z) Positioning System

A PID control algorithm in position control mode, as shown in Figure 3-12, is used to control the two vertical actuators set up in a gantry configuration in order to apply the predetermined amount of normal load at the contact patch. For the current configuration, a human operator is required to adjust the position of the wheel carriage based on the force readings obtained from the charge amplifiers of the load platform.

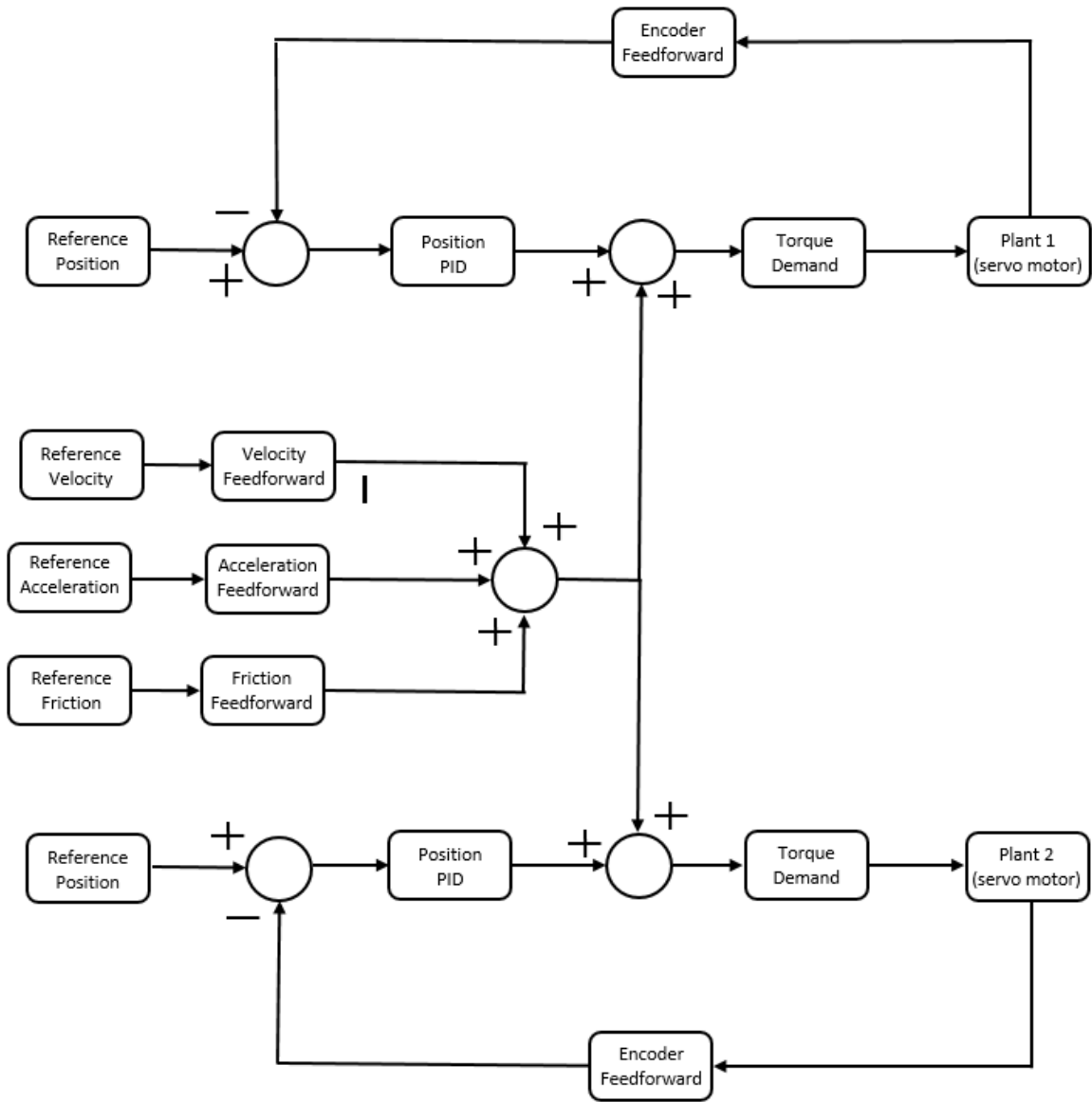


**Figure 3-12** Block diagram showing Position Control (PC) mode for gantry (without yaw) axis of the Roller Rig

#### 3.1.4.4 Cant Angle Positioning System

Cant angle or super elevation of a locomotive comes into play when it is negotiating a curve. The rail cant, along with the radius of the curve and wheelbase of the bogie, help determine the maximum velocity of the locomotive for a given curve rail section. A PID control algorithm in position control mode, as shown in Figure 3-12, is used to control the cant angle degree of freedom on the Roller Rig.

#### 3.1.5 Wheel and Rail Profiles





**Figure 3-14** Driveline with laser sensor and receiver units mounted on either side of coupling  
 Figure 3-15 shows the receiver unit (left), computer unit (middle), and laser unit (right) as a part of the OPTALIGN Smart RS laser alignment system.



**Figure 3-15** Components of the OPTALIGN smart RS5 laser alignment system

### 3.1.7 Contact Patch Parameter Estimation Using Hertzian Contact Theory

In the past, various studies have been conducted to measure the wheel-rail contact patch parameters, including the contact shape, size, and stresses. Andrews [28] used pressure sensitive materials, such as carbon paper, between the wheel-rail contact points to estimate the contact geometry. He also accounted for the thickness of the paper in the calculations, which introduced a small error in the static measurements. The results had good agreement with Hertzian theory and Carter's contact theories.

Marshall et al. [29] used ultrasonic sound waves to nondestructively quantify the stress distribution at the wheel-rail contact patch. A spring model was used to represent the response of the wheel-

rail interface to an ultrasonic wave. The amount of ultrasonic wave reflected from the wheel-rail interface under high and low contact stiffness conditions was used to quantify the contact stiffness. A map of the contact stiffness points was determined, and pressure was then determined using a parallel calibration experiment. Pau et al. [30] also used an ultrasonic method to estimate contact stresses at the wheel-rail interface. They used a finite element modeling approach to establish an empirical relationship between contact pressure and ultrasonic reflection that was used to calibrate their experimental setup. Their results also had good agreement with the Hertzian contact theory. Recently, Dwyer-Joyce et al. [31] used an ultrasonic sensor-based approach to detect the onset of flange contact in real-time conditions.

In order to quantify the contact patch parameters for the present research for a cylinder-on-rail type contact, the length and width of the contact patch and contact stresses are estimated using the Hertzian contact theory, assuming a cylinder-on-cylinder contact. The maximum contact stresses between two curved surfaces depends on the following:

- type of curvature (sphere/cylinder)
- radius of curvature
- magnitude of contact forces
- elastic modulus and Poisson's ratio of contact surfaces

Figure 3-16 shows the Hertzian contact condition for a cylinder-on-cylinder.

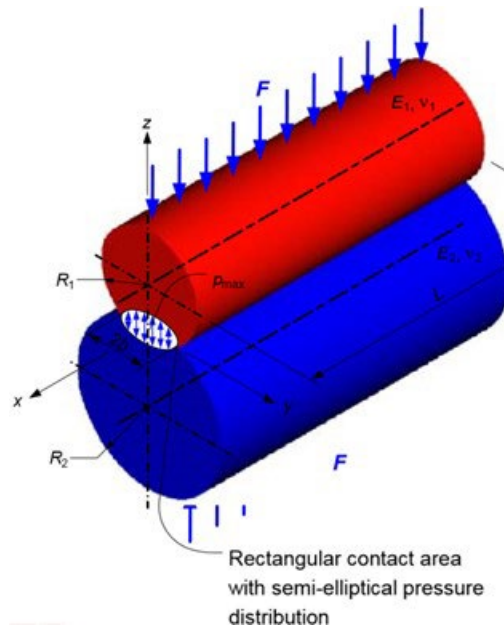


**Figure 3-16** Hertzian contact patch stress for cylinder-on-cylinder contact condition [32]  
 The contact patch length is estimated using the contact marks on the roller. The wheel and roller are first cleaned. Both materials are made from steel, whose properties are given in Table 3-3.

**Table 3-3** Parameters to calculate the half-width at contact patch

Parameter		Value
Young's modulus - $E_1, E_2$ (GPa)		200
Poisson's ratio - $\nu_1, \nu_2$		0.27
Wheel radius, $R_w$ (m)		0.116
Roller radius, $R_r$ (m)		0.504
Normal load ( $F_z$ )		2660
Estimated length of contact patch (mm)		4
Calculated half-width of contact patch, $b$ (mm)		0.83
Static contact patch stress estimation	$\sigma_{mean}$ (ksi)	58.1
	$\sigma_{max.}$ (ksi)	74

The half-width,  $b$ , of the rectangular contact area of two parallel cylinders is calculated using the relation

$$b = \sqrt{\frac{4 * F_z * \left[ \frac{1 - \nu_1^2}{E_1} + \frac{1 - \nu_2^2}{E_2} \right]}{\pi * L * \left( \frac{1}{R_1} + \frac{1}{R_2} \right)}} \quad (9)$$

where  $b$  is the half-width of the rectangle,  $F_z$  is the normal load,  $\nu_1, \nu_2$  are the Poisson's ratio for the two cylinders,  $E_1, E_2$  are the modulus of elasticity for the two cylinders,  $R_1, R_2$  are the radius of curvature of the two cylinders, and  $L$  is the length of the contact patch.

Thus, using the value of half-width of the estimated rectangular contact patch, the mean and maximum contact stresses are calculated using the equations shown below:

$$\sigma_{mean} = \frac{F_z}{2 * b * L} \quad (10)$$

$$\sigma_{max} = \frac{2 * F_z}{\pi * b * L} \quad (11)$$

### 3.1.8 Creepage Control Between Wheel-Rail Contact

In case of Hertzian contact, the creepage at the contact patch is a function of the relative speeds between the wheel and roller. All experimental studies on the Roller Rig are performed using the quasi-static creepage formula, as the wheel-rail contact does not move on the wheel tread. Figure 3-17 shows the front view of the Roller Rig with the wheel and roller mounted in a vertical configuration. The roller velocity is kept at the base velocity, and the creepage is introduced between the wheel and roller by changing the wheel velocity at the wheel-rail contact. Both the

wheel and roller driveline are driven by an AKM84T 3-phase permanent magnet AC servo motor manufactured by Kollmorgen (Radford, VA). The high-resolution 20-bit encoder feedback, and a motion controller tuned to a high bandwidth, control the differential speed between the two rotating bodies with 0.1-rpm accuracy. This ensures low velocity error in the wheel and roller drivelines, thus ensuring creepage control with a higher accuracy.

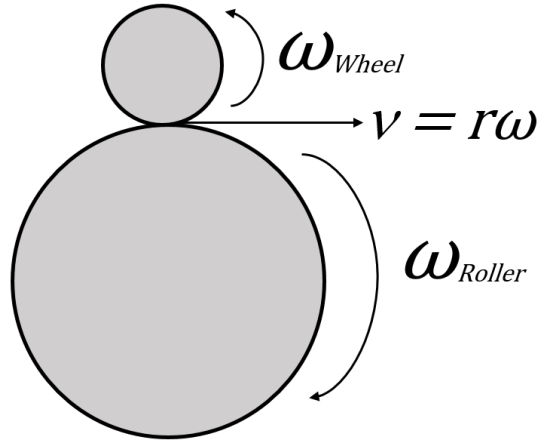


**Figure 3-17** Front view of the Roller Rig showing the wheel and roller mounted in a vertical configuration

Table 3-4 shows an example of measurement points chosen for a creep-creepage experimental study. A 27-point creep-creepage experimental study is shown with base speed of 3 km/h. The wheel linear velocity at each creepage point is determined using Equation 12. The quasi-static longitudinal creepage formula is useful for test rigs, as it uses the mean of the wheel and roller velocities for normalizing the creepages. On the other hand, the railway case leads to a simplified formula, where  $0.5 * (V_{wheel} + V_{roller}) \sim V_{wheel}$  [11].

$$\text{Longitudinal Creepage (\%)} = \frac{(V_{wheel} - V_{roller})}{0.5 * (V_{wheel} + V_{roller})} \quad (12)$$

where,  $V_{wheel}$  is the wheel tangential velocity, and  $V_{roller}$  is the roller tangential velocity.

The rotational frequencies are determined from the base speed and the wheel and roller diameters. The commanded velocity counts for each of the wheel and roller drivelines is determined using the relation

$$\text{Velocity Counts} = \text{CPR} * \text{RPS} \quad (13)$$

where  $CPR$  is the counts per revolution of the wheel/roller driveline, and  $RPS$  is the rotational frequency of the wheel/roller.

For conducting any study on the slip dynamics at the wheel-rail contact, the base speed is set on the roller, which remains constant for all the experiments. The creepage at the wheel-rail contact is introduced by increasing the wheel velocity. In order to command velocities to the wheel and

roller drivelines, velocity counts are calculated based on the encoder resolution of the servo motor and accounting for the gear ratio of the gearbox. The wheel velocity counts for a base velocity of 3 km/h and for a 27 point, creep-creepage curves for 0 – 10% longitudinal creepage are calculated and shown in Table 3-4.

**Table 3-4** Wheel and roller commanded velocity counts calculated for adhesion-creepage measurements for conducting experimental studies on the Roller Rig

Exp. No.	Longitudinal Creepage (%)	Roller Velocity (km/h)	Wheel Velocity (km/h)	Wheel RPS (Hz)	Roller RPS (Hz)	Wheel Velocity (Counts)	Roller Velocity (Counts)
1	0	3	3.000	1.144	0.262	5997511	7301850
2	0.1	3	3.003	1.145	0.262	6003511	7301850
3	0.2	3	3.006	1.146	0.262	6009518	7301850
4	0.4	3	3.012	1.149	0.262	6021549	7301850
5	0.6	3	3.018	1.151	0.262	6033604	7301850
6	0.8	3	3.024	1.153	0.262	6045684	7301850
7	1	3	3.030	1.155	0.262	6057787	7301850
8	1.3	3	3.039	1.159	0.262	6075989	7301850
9	1.6	3	3.048	1.162	0.262	6094245	7301850
10	1.9	3	3.058	1.166	0.262	6112556	7301850
11	2.3	3	3.070	1.171	0.262	6137058	7301850
12	2.7	3	3.082	1.175	0.262	6161660	7301850
13	3	3	3.091	1.179	0.262	6180176	7301850
14	3.5	3	3.107	1.185	0.262	6211163	7301850
15	4	3	3.122	1.191	0.262	6242307	7301850
16	4.5	3	3.138	1.197	0.262	6273611	7301850
17	5	3	3.154	1.203	0.262	6305075	7301850
18	5.5	3	3.170	1.209	0.262	6336702	7301850
19	6	3	3.186	1.215	0.262	6368491	7301850
20	6.5	3	3.202	1.221	0.262	6400444	7301850
21	7	3	3.218	1.227	0.262	6432563	7301850
22	7.5	3	3.234	1.233	0.262	6464849	7301850
23	8	3	3.250	1.239	0.262	6497303	7301850
24	8.5	3	3.266	1.245	0.262	6529927	7301850
25	9	3	3.283	1.252	0.262	6562721	7301850
26	9.5	3	3.299	1.258	0.262	6595688	7301850
27	10	3	3.316	1.264	0.262	6628828	7301850

For experiments conducted at different base speed and creepage distribution, tables can be generated in a similar manner for creep-creepage studies in order to measure the distribution of longitudinal and lateral creep forces at the wheel-rail contact.



## Chapter 4. Experiment Workflow

Design of Experiments (DOE) is a powerful tool used in a variety of experimental situations. DOE allows multiple input factors to be manipulated to study their effects on a desired output. By changing multiple inputs to the test at the same time, DOE can identify important interactions, which is not possible when changing only one input parameter. All possible combinations can be investigated (full factorial), or only a portion of the possible combinations can be investigated (fractional factorial). Another possible DOE is one-factor-at-a-time (OFAT), which examines the effect of a single factor or variable [33]. Factorial design experiments offer several advantages over OFAT, as listed below:

- Factorial designs are more efficient than OFAT experiments, as they can help find optimal conditions faster than OFAT,
- Factorial designs allow for additional factors to be analyzed at no additional cost,
- The effect of one factor is different for different levels of another factor, which cannot be analyzed by an OFAT experiment design. Factorial design allows the effect of one factor to be estimated at several levels of other factors, leading to conclusions over a range of experimental conditions, and
- Use of OFAT design can lead to serious misunderstanding of how the response changes by changing different factors.

In this experimental study, each factor has multiple levels. With a large number of input factors, conducting a full factorial design is not feasible. As a result, a fractional factorial design is used to limit the input variables and levels of each input factor that are of interest to the railroad industry. As a primary step, the different input factors that affect the contact patch dynamics are identified. Figure 4-1 lists the controlled input factors, uncontrolled input factors, and the measured output responses used to design the experiments for the study.

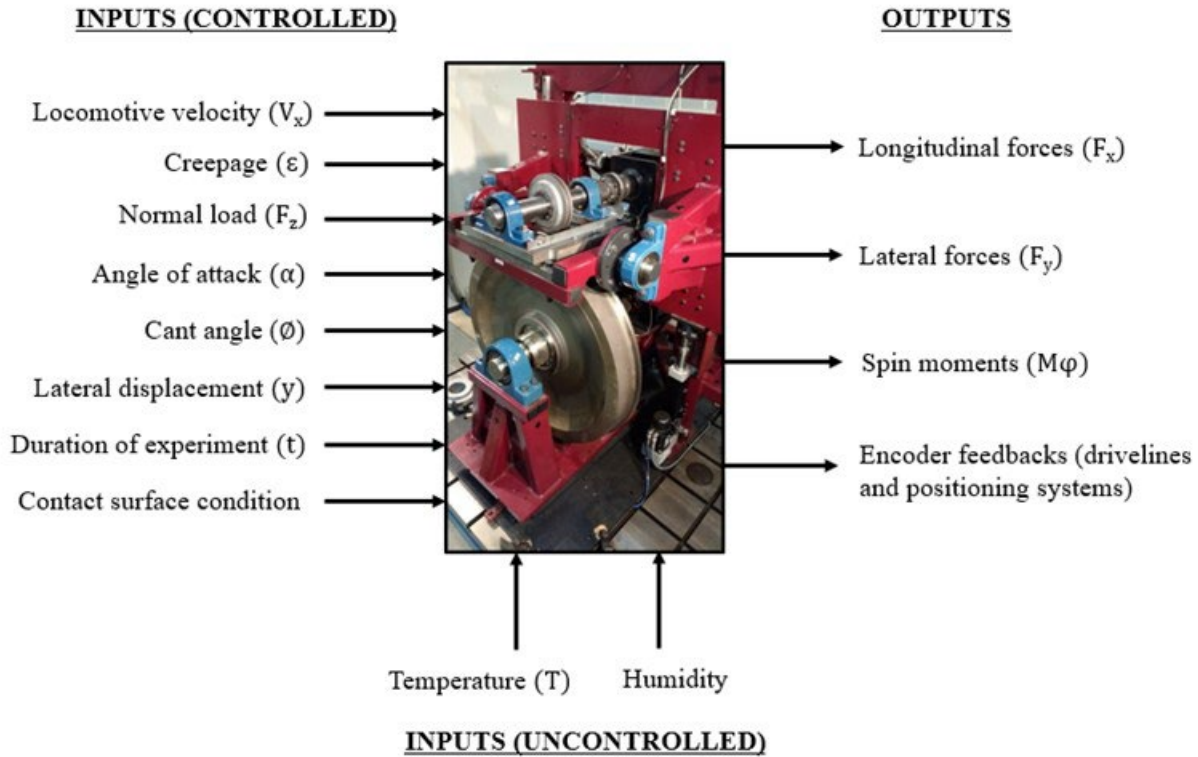


**Figure 4-1** Input-process-output diagram for Roller Rig

#### 4.1 Effect of Input Parameters on Measured Responses

Before conducting experimental studies on the Roller Rig, the effect of each input parameter on the measured outputs is studied in detail to obtain a deeper understanding of each of their effects on the creep forces at the wheel-rail contact. The objective of the experimental studies presented in this research is to establish a baseline for the performance of the Rig, conduct parametric studies by varying input parameters of interest, and to streamline the experimental design process and data post-processing to generate results in a repeatable, and reliable manner. Another major objective of this research is to automate the data post-processing by developing algorithms that can automatically extract raw data from saved experiment files, perform data conversion and filtering operations, conduct statistical analysis on data, and generate the required results. These measures would save huge amounts of time in data post-processing so that more time can be devoted to interpreting the results.

##### 4.1.1 Angle of Attack (AoA)

AoA is defined as the yaw motion of the wheel flange with respect to the rail, and it occurs especially on curves. Figure 4-2 shows the angle of attack on a wheelset due to yaw motion of the wheelset. It is the main parameter causing high rate of wear for both wheel and rail. Small values of angle of attack can be associated with large forces at the wheel-rail contact. Hence, it is one of the most important parameters that is evaluated as part of this research. For a given wheel profile, and constant creepage, the lateral force is determined by the AoA. A non-zero yaw angle will give

rise to a lateral velocity component, which is converted to the corresponding force by the creep-creepage relationship [34]. The Roller Rig is equipped with the AoA positioning system with the capability to adjust the angle dynamically during the course of an experiment.

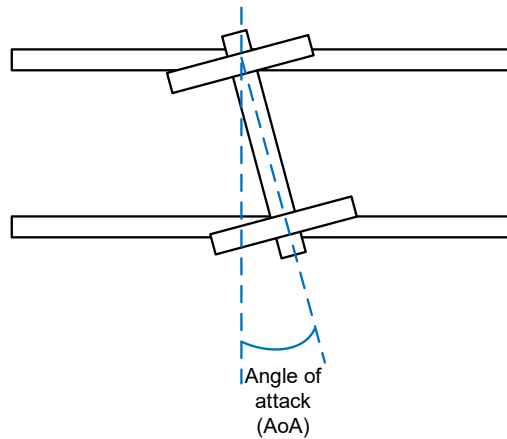


**Figure 4-2** Angle of Attack (AoA) of wheelset relative to rail during curving

#### 4.1.2 Cant Angle

Cant is the difference in elevation (or vertical distance) of the outer rail with respect to the inner rail in a curve. The angular difference is called the cant angle and helps a train negotiate a curve, minimizing contact between the wheel flange and rail, which in turn minimizes friction and wear. Figure 4-3 shows the cant angle of a single locomotive wheel, as experienced in the field. Cant is positive when the outer rail is at a higher vertical elevation than the inner rail, which is the desirable configuration for laying the track in a curve. Cant is negative when the inner rail has a higher vertical elevation than the outer rail. It is a non-standard configuration that becomes unavoidable in curves involving turnouts.

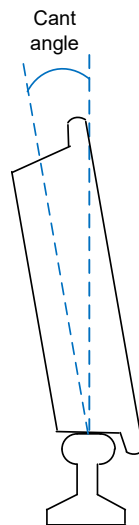


**Figure 4-3** Vertical difference in elevation of inner and outer rail measured as cant angle

Cant deficiency occurs when a train negotiates a curve at a speed greater than the balance speed, resulting in a net lateral force acting towards the outside of the curve. It is measured in inches and is the extra amount of elevation that must be added to achieve balance speed. Cant excess is a situation when a train negotiates a curve at a speed lower than the balance speed, resulting in net lateral acceleration acting towards the inside of the curve. The aim of introducing rail cant in a curve is to prevent flange contact. Slower trains will tend to make contact with the gauge side of the inner rail due to cant excess, while the fast trains will tend to make contact with the gauge side of the outer rail due to cant deficiency. An extreme situation of any one of the above cases results in excessive lateral forces, with a potential to cause gauge widening, flange climbing, and derailment.

Super elevation of a rail for a given section of a curve is determined by the maximum design speed and degree of curve, and is independent of the weight of the locomotive. The value of super elevation/cant is typically 6-7" for freight trains and 5" for passenger trains.

### **4.1.3 Lateral Displacement**

Lateral displacement is the offset distance of the center of the wheel tread from the contacting rail surface. It is defined as the linear position of the wheel with respect to the rail.

When the wheel is displaced laterally from the center of the track, the diameters of the wheels on the two sides of the wheelset become different, leading to different tangential velocities at the contact patch. As a result, the wheelset tries to steer back to its equilibrium position. Thus, the coning of the locomotive wheels manifests itself into this lateral swaying behavior, known as hunting oscillation. In theory, if the track is straight, hunting will not take place, as the wheelset will be centrally aligned on the track (that is, be at its equilibrium position), pointing straight ahead with the axle at right angle to the rails. In real life, no track is straight, so once the wheelset is lowered onto the rails and is rolling, it will have a deviation in alignment irrespective of how well it is aligned. As a result, the wheelset will have an angle of attack and will try to ride up the rail on its conical wheel profile. The difference in rolling radius of the wheels on either side of the axle will become larger, leading to larger differential velocity between the two wheels. This results in the outer wheel speeding up and the inner wheel slowing down, causing the wheelset as a whole to swivel in a horizontal plane and steer back towards an equilibrium position. Once it reaches its equilibrium position, the wheelset will overshoot in the other direction laterally, and this phenomenon repeats itself. The magnitude and duration of the hunting oscillations will depend on the lateral damping in the wheelset [35]. Figure 4-4 shows the lateral displacement from the equilibrium position, as experienced by a truck-set on a straight tangent track in the field.

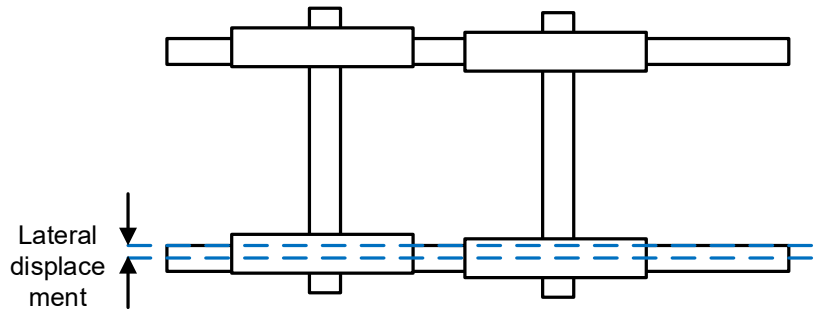


**Figure 4-4** Lateral displacement of wheelset from equilibrium position

## 4.2 Experiment Design Process

A well-designed experiment is as simple as possible, while enabling the user to obtain the required information in a repeatable manner.

The quickest and most efficient experiment design is determined by carrying out the experiments and analyzing the collected data. Several approaches are considered before a design is finalized. The following factors are considered when evaluating an experiment design:

- Awareness of different errors to which the instrumentation is subject, and
- Experience with the use of the current instrumentation.

Figure 4-5 illustrates the final experiment design process incorporated for conducting the creep-creepage experimental studies. This experimental design is used to evaluate the contact forces for each treatment combination of the fractional factorial Design of Experiments (DOE). This experiment design ensures that boundary conditions are kept constant for each experiment, and that data collection and post-processing procedure are uniform in order to reduce the sources of variability that are controllable. This experiment design is used for conducting all the experimental studies presented in this report.

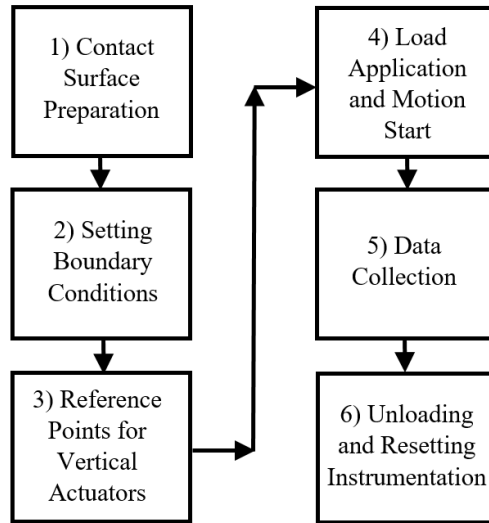


**Figure 4-5** Block diagram of workflow of each experiment for conducting the creep-creepage measurements

Each individual step in Figure 4-5 is explained in detail in the following sections.

#### 4.2.1 Contact Surface Preparation

The effect of a third-body layer significantly affects the distribution of the longitudinal and lateral creep forces at the contact patch. A third-body layer refers to an interfacial layer at the wheel-rail contact which separates the two primary bodies in contact. The Roller Rig consists of two rotating steel bodies in rolling contact motion. At high normal loads, a machining action is inevitable, and the resulting debris significantly affects the longitudinal and lateral creep forces at the wheel-rail contact, thereby introducing a new source of variability in the experiment. As a result, the contacting surfaces of the wheel and roller are controlled for each experiment to reduce sources of variability. For treatment combinations involving clean and dry contacting surface condition, fabric sheets are used to clean the surfaces of wheel and roller before conducting each experiment. A thorough cleaning is performed using this method to remove any natural third-body layer, such as metal debris and metal oxide, which might have formed at the wheel-rail interface.

For treatment combinations involving top-of-rail lubricants, a thin layer of the lubricant is applied on both the wheel and roller contacting surfaces for the entire duration of the experiment. This is done so that any lubricant displaced from the contacting surfaces because of high contact pressures is restored back onto the surface.

#### 4.2.2 Setting boundary conditions

Based on the goal of the experimental study, an adjustment of the boundary conditions for each experiment is performed. The Roller Rig has six linear actuators and two rotary motors that control these boundary conditions, namely, cant angle, angle of attack, creepage, lateral displacement, locomotive velocity, and normal load. Any changes in these parameters influences the creep-creepage dynamic measurements at the wheel-rail contact. The zeroing of the cant angle, angle of

attack, and lateral displacement are performed using external instrumentation and techniques that are independent of the encoder feedback from the actuators. The lateral displacement for a cylindrical wheel profile does not play a role in affecting the contact patch forces. However, for a conical wheel profile, the lateral displacement is kept at the center of the wheel tread for all experimental studies. The linear speed of the wheels is kept constant at 3 km/h to focus the attention on the low speed contact mechanics and dynamics. The normal load is varied from half-load of a passenger locomotive to that of a fully loaded freight locomotive.

### 4.2.3 Reference Points for Vertical Actuators

The normal load, in a position control feedback loop setup, such as the Roller Rig is controlled by pressing the wheel carriage on the roller contact surface, until the pre-defined static load is achieved. Since the load is kept constant for the treatment combinations (experiments) in an experimental study, two reference positions are defined. The first reference position is when the load on the roller is zero, which represents the unloaded condition. The second reference position is when the simulated load on the roller is the pre-defined amount based on the experimental study testing parameters.

### 4.2.4 Load Application and Motion Start

After setting the static load using the vertical linear actuators, all the boundary conditions are verified again, and the motion of the wheel and roller is started. The wheel is rotated in the clockwise direction, while the roller is rotated in the counter-clockwise direction. This sign convention is kept constant for all the experimental studies presented in this research study. Figure 4-6 shows a snapshot of the Roller Rig's Motion Console Graphic User Interface (GUI) that is used to control the motion of all the degrees of freedom. It provides an environment for conducting experimental testing and monitoring of motion control components of the Roller Rig.



Figure 4-6 Snapshot of Roller Rig's Motion Console Graphic User Interface (GUI)

## 4.2.5 Data Collection

The data acquisition setup is setup in such a way that the data collection begins as soon as the motion of the wheel and roller driveline starts. The total duration of data collection for each treatment combination (experiment) is pre-defined based on the parameters of the experimental study. This ensures an equal number of data points being collected for each experimental study which makes the batch processing of data easier. The longitudinal and lateral creep forces and normal load data is collected from the two load platforms. The encoder feedback from the positioning systems and the two rotary motors is also collected. With 16 measurement channels and a sampling rate of 2000 Hz, a large amount of data points are collected in a short time, which captures the contact patch dynamics. Figure 4-7 shows the measurement traces that are recorded when the wheel is rotated in contact with the roller. The feedback from the positioning systems verifies if the boundary conditions are kept constant for the full experiment duration. The velocity feedback from each of the rotary motors verifies that the creepage is constant between the wheel and roller. After completing the experiment, the data is saved in a new text file after assigning it a file identification number.

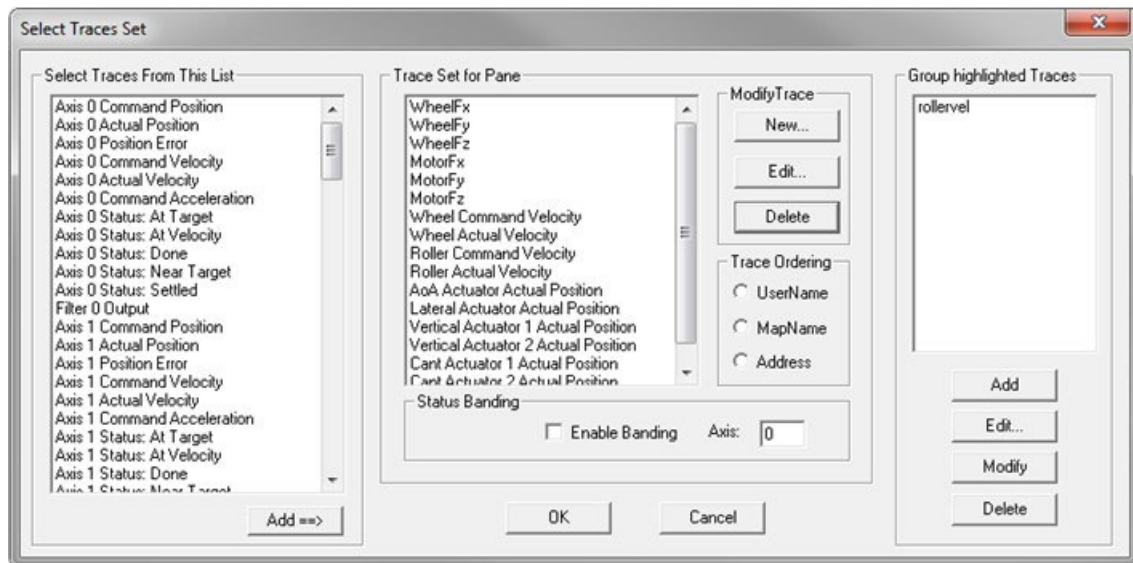


Figure 4-7 Motion Scope (MS) traces consisting of data collected from 16 sensor channels

## 4.2.6 Unloading and Resetting Instrumentation

After saving the collected data points of the experiment in a new text file, the Rig is unloaded by bringing the vertical actuators that are responsible for controlling the normal load to their first reference position (unloaded condition). Instrumentation resetting for the charge amplifiers is done to remove any residual charge readings from the sensors.

These steps ensure a well-designed experiment that allows measuring the creep forces and spin moments quasi-statically at the wheel-rail contact interface in a repeatable and consistent manner, with the controlled input variables held tightly for the entire duration of the experiment.

## Chapter 5. Data Post-Processing

This chapter explains the data processing techniques that are developed as part of this research to automate the data post-processing to convert the raw data collected from the DAQ system of the Rig into creep-creepage curves. The Roller Rig is designed to conduct wear studies, creep-creepage curve analysis, vibration analysis, and derailment studies, among many others. To ensure that all the dynamics are captured when conducting such studies, a sampling rate of 2 kHz is chosen for data collection from the instrumentation setup, comprised of two load platforms and six encoder feedbacks. As a result, in a very short duration of testing, a large amount of data is collected. Batch processing scripts were developed that can automatically extract and sort data from individual experiments using look-up tables, perform data conversion from counts into standard units, apply post filters, compute the required statistical parameters, perform curve fitting using linear/non-linear regression analysis and remove outliers. The experimental design techniques presented in the previous chapter and data post-processing techniques presented in the current chapter allows for conducting and analyzing results in an organized manner, thus enabling us to conduct many more experiments in the same duration of time.

Figure 5-1 shows the steps performed to post-process the data collected and stored by the DAQ system when performing an experimental study on the Roller Rig testing setup.

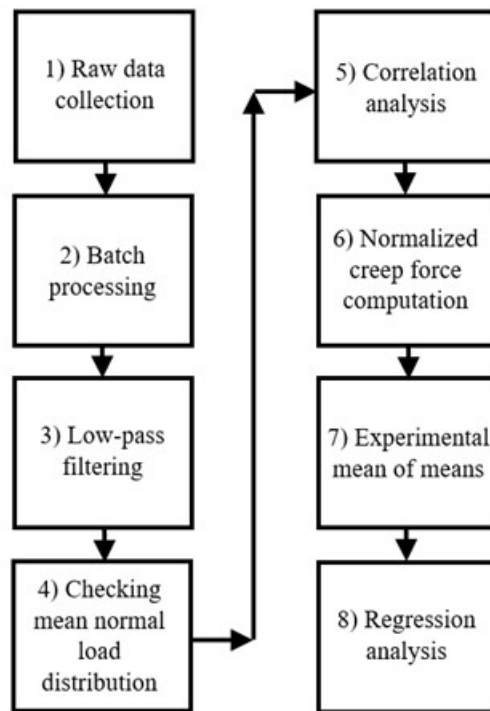


**Figure 5-1** Data post-processing workflow for generating creep-creepage curves from an experimental study

Each step mentioned in Figure 5-1 is explained in the subsequent sections by taking the example of a baseline experimental study. The boundary conditions used for this baseline experimental study are listed in Table 5-1.

The field load, which is the load corresponding to field testing loads, is calculated using the following equation:

$$\text{Field Load} = \text{Lab Load} * \text{Force Scaling Factor} * \text{number of W/R pairs} \quad (14)$$

where *Lab Load* is the actual load measured between the wheel-roller contact patch, *Force Scaling Factor* for the Roller Rig is 16, and *number of W/R pairs* for a full railcar is 8.

**Table 5-1** Boundary conditions for baseline experimental study

Wheel profile	Cylindrical
Roller profile	US-136 rail
Angle of attack (°)	0
Cant angle (°)	0
Field speed (mph / km/h)	1.86 / 3
Lab Load (lb. / kN)	562 / 2.5
Field load (lb. / kN)	71936 / 320
Lateral displacement (in.)	0
Contact condition	Dry
Commanded creepage (%)	0.2 - 6
Creepage increments (%)	0.1% from 0.2-3%, 0.2% from 3-6%
Repetitions per creepage point	4
Experiments conducted	176
Sampling frequency (kHz)	2
Measurement time for each experiment (sec.)	7

### 4.3 Raw Data Collection

In the control network of the Roller Rig, all the sensor readings, including the eight piezoelectric load cells from the primary and secondary load platforms and the six encoder feedbacks from the AKM84T (rotary) and AKM52H (linear) motors, are collected using the SynqNet's SQIO-SQID data acquisition boards. Table 5-2 lists the conversion factors for converting the raw data collected from the DAQ to meaningful physical units. The wheel and roller drivelines each have gearboxes with reduction ratios of 5:1 and 28:1, respectively, attached to the face of the AKM84T rotary

motors. As a result, the required encoder counts for one complete rotation of the wheel and roller are given by the following equations:

$$1 \text{ wheel rotation} = 2^{20} * 5 = 5242880 \text{ encoder counts}$$

$$1 \text{ roller rotation} = 2^{20} * 28 = 29360128 \text{ encoder counts}$$

As part of the EC4 linear positioning system, the AKM52H servo motor transfers rotary motion using a belt/pulley mechanism with a reduction ratio of 2:1 to a 10 mm/revolution ballscrew mechanism for providing smooth and efficient linear motion. The PPR for 1 mm linear stroke of the linear actuators is given by the following equation:

$$1 \text{ mm linear displacement} = \frac{2^{32} * 2}{10} = 858993459 \text{ counts}$$

**Table 5-2** Conversion factors for converting raw data from DAQ to meaningful physical units

Component	Sensor / Resolution	Query	Raw Data Form (counts)	Post Unit Conversion (Physical Units)
Primary and secondary load platforms	Piezoelectric load cells / 13.6 kN	Vertical forces, $F_z$	-32768 to +32767	-16000 N to +16000 N
		Longitudinal forces, $F_x$	-32768 to +32767	-8000 N to +8000 N
		Lateral forces, $F_y$	-32768 to +32767	-8000 N to +8000 N
AKM84T rotary motors	Single-turn EnDat 2.2 absolute sine encoder / $2^{20}$ PPR	Wheel position	5242880 PPR	1 wheel revolution
		Roller position	29360128 PPR	1 roller rotation
AKM52H linear motors	Multi-turn EnDat 2.2 absolute sine encoder / $2^{32}$ PPR	Lateral displacement	858993459.2 PPR	1 mm linear displacement
		Angle of attack		
		Vertical displacement		
		Cant angle		

For analog inputs, SynqNet reads  $\pm 10$  V with  $\pm 32767$  counts. For example, for converting a SynqNet reading of 8000 counts for the primary load platform in the vertical axis (Z) to Newton, we have the following:

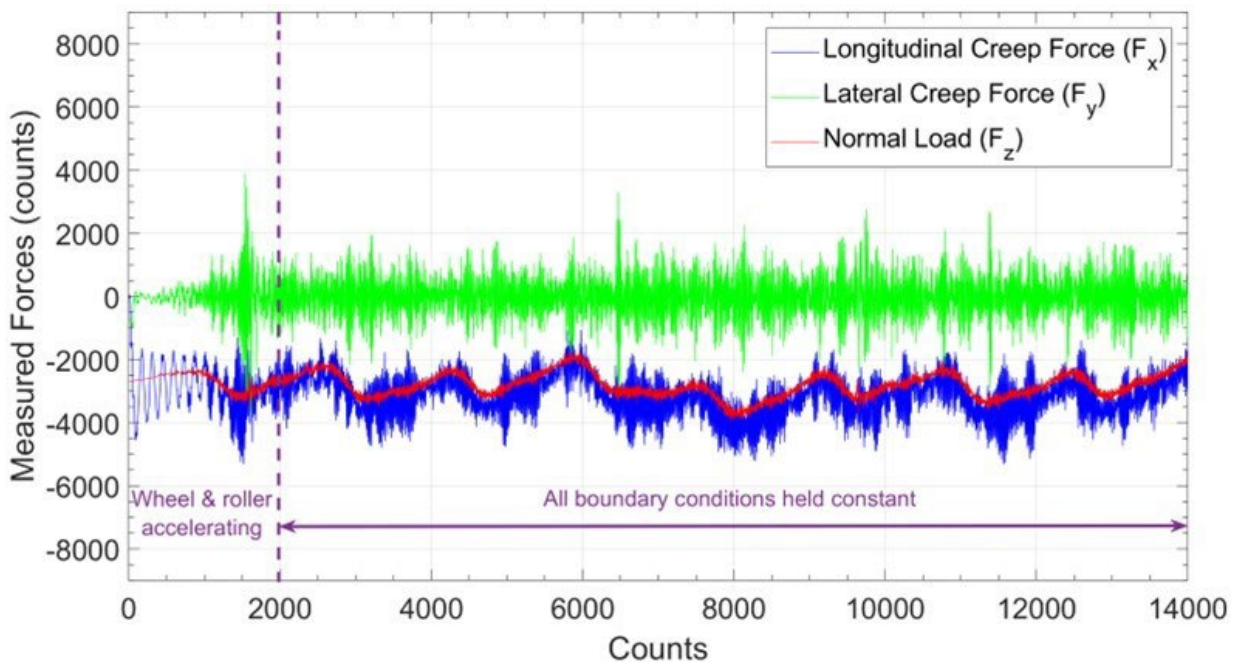
$$F_z = 8000 * \frac{32000}{32767} = 7812.73 \text{ N}$$

Similarly, for converting a SynqNet reading of 3500 counts for the primary load platform in the longitudinal axis (X) to Newton, we have the following:

$$F_x = 3500 * \frac{16000}{32767} = 1709.03 \text{ N}$$

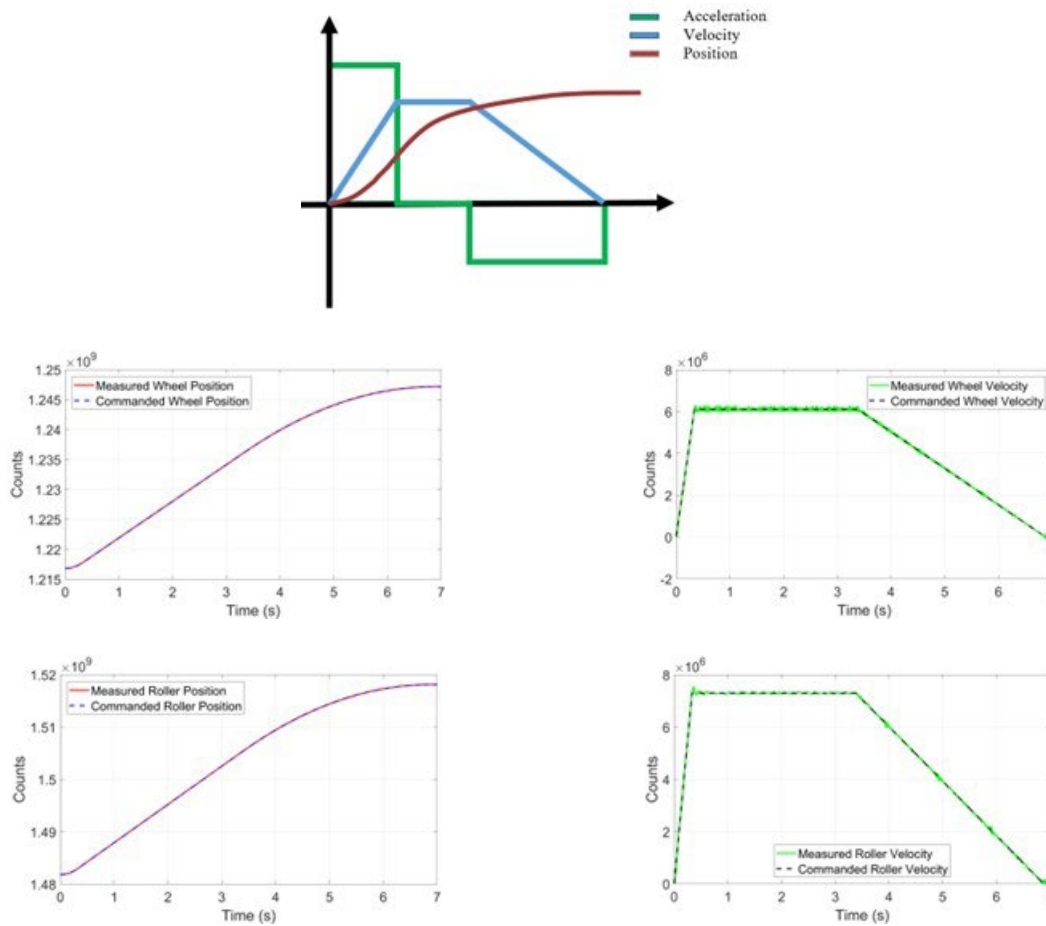
The conversion factors listed in Table 5-2 for the primary and secondary load platforms will have to be adjusted if the range of measurement for the force channels is changed at any point of time from the charge amplifiers.

Figure 5-2 shows raw data for a measurement/experiment taken at 1.9% creepage, when all other boundary conditions mentioned in Table 5-1 are held constant.



**Figure 5-2** Sample of raw force data collected from the DAQ system for measurement points corresponding to 1.9% creepage in the experimental study

From Figure 5-2, it is observed that the raw data consists of a high frequency signal riding on top of a low frequency signal. The high frequency component is because of a lack of compliance between the steel wheel and roller, under high normal loads and stresses. The low frequency component is an artifact of the position control mechanism of the vertical loading actuators. A detailed analysis on the effect of position control setup on the force measurements is given in Chapter 3. Figure 5-3 shows the commanded, and measured wheel and roller positions, and velocities when they are rotated in contact at 1.9% creepage. The angle of attack, and cant angle are kept at zero for the entire duration of the test. The mean normal load for the entire test duration is ~2500N. It is observed that the measured wheel, and roller velocities are held tightly at the commanded values. The length of the velocity ramp during acceleration, and deceleration is adjusted on the magnitude of acceleration, and deceleration, respectively.



**Figure 5-3** Trapezoidal point-to-point motion for wheel and roller servo motors (top); actual, and commanded wheel positions (middle-left); actual, and commanded wheel velocities (middle-right); actual, and commanded roller positions (bottom-left); actual, and commanded roller velocities (bottom-right)

#### 4.4 Batch Processing and Data Sorting

Once all the raw data is collected from all the measurements/experiments at different creepage levels for an experimental study, it is fed into a batch-processing algorithm written in MATLAB. The algorithm takes the start and end experiment file numbers and look-up table data as inputs. The first 2000 samples (1 second) of data are chopped off from the raw data from each measurement, as the wheel and roller are accelerating and have not reached their steady state values. The remaining 12000 samples (6 seconds) of data are collected with all the boundary conditions held constant.

The look-up table consists of multiple columns consisting of commanded creepages and its corresponding wheel rotational frequency, as shown in Table 5-3. A different look-up table is generated for different base velocities simulated on the Roller Rig. The algorithm compares the wheel rotational frequency of the experiment to that of the lookup table and matches the experiment to the corresponding creepage value.

Figure 5-4 shows the wheel Rotations per Second (RPS) versus time, where each step represents the wheel velocity at a different creepage value ranging from 0.2% to 10%.

**Table 5-3** 2D lookup table consists of creepage on the Y-axis and wheel RPS on the X-axis for all wheel longitudinal commanded velocities

	<b>Wheel Longitudinal Velocity (km/h)</b>			
	<b>Wheel Rotational Frequency (Hz)</b>			
<b>Creepage</b>	<b>3</b>	<b>4</b>	<b>5</b>	<b>6</b>
<b>0.2</b>	1.146	1.528	1.392	1.670
<b>0.4</b>	1.149	1.531	1.394	1.673
<b>0.6</b>	1.151	1.534	1.397	1.677
<b>0.8</b>	1.153	1.537	1.400	1.680
<b>1</b>	1.155	1.541	1.403	1.683
<b>1.3</b>	1.159	1.545	1.407	1.688
<b>1.6</b>	1.162	1.550	1.411	1.694
<b>1.9</b>	1.166	1.555	1.416	1.699
<b>2.3</b>	1.171	1.561	1.421	1.705
<b>2.7</b>	1.175	1.567	1.427	1.712
<b>3</b>	1.179	1.572	1.431	1.717
<b>3.5</b>	1.185	1.580	1.438	1.726
<b>4</b>	1.191	1.588	1.446	1.735
<b>4.5</b>	1.197	1.595	1.453	1.743
<b>5</b>	1.203	1.603	1.460	1.752
<b>5.5</b>	1.209	1.612	1.467	1.761
<b>6</b>	1.215	1.620	1.475	1.770
<b>6.5</b>	1.221	1.628	1.482	1.779
<b>7</b>	1.227	1.636	1.490	1.788
<b>7.5</b>	1.233	1.644	1.497	1.797
<b>8</b>	1.239	1.652	1.505	1.806
<b>8.5</b>	1.245	1.661	1.512	1.815
<b>9</b>	1.252	1.669	1.520	1.824
<b>9.5</b>	1.258	1.677	1.527	1.833
<b>10</b>	1.264	1.686	1.535	1.842

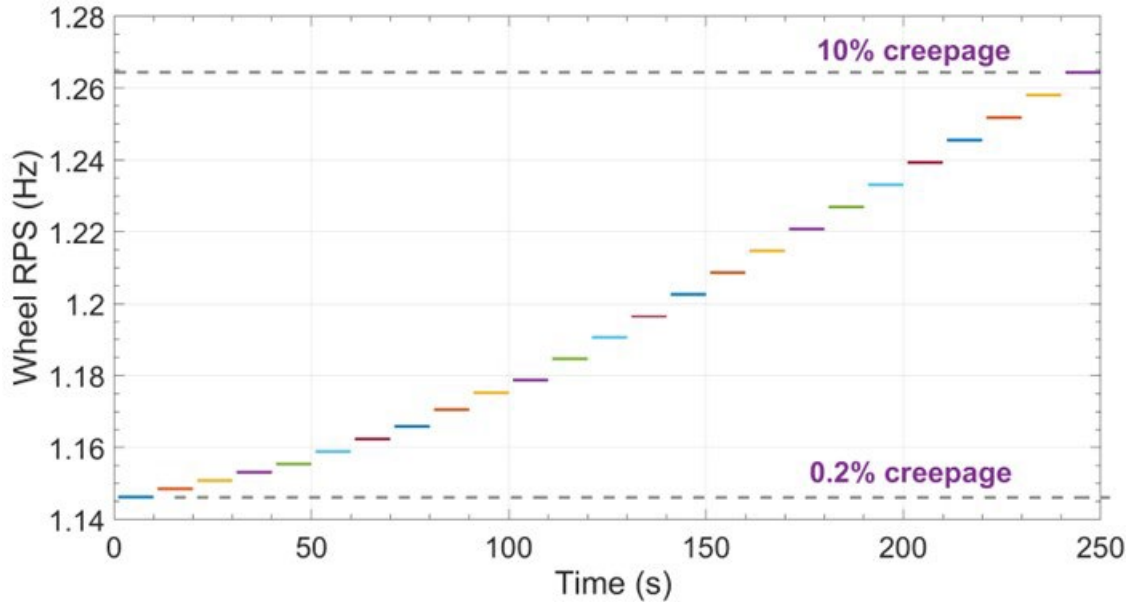


**Figure 5-4** Wheel Rotations per Second (RPS), versus time where each step represents a creepage value between 0.2% and 10%

#### 4.5 Low Pass Filtering of Raw Force Data

The normal load data was low-pass filtered using a digital second order Butterworth filter at 10 Hz break frequency, in order to eliminate all of the high frequency noise in the data. The filtering is performed using a zero phase distortion method, using the “filtfilt” function in MATLAB software, which makes the equivalent filter a fourth order filter. A Butterworth digital filter is chosen, as it has a gain of 0 dB throughout the passband. It ensures that the signal content below the break frequency passes through the filter in its original form without getting attenuated or amplified, which is desired. At a field speed of 3 km/h, the wheel and roller’s rotational frequencies are 1.14 Hz and 0.26 Hz respectively. Thus, a break frequency of 10 Hz is chosen, as it is higher than the frequency range of interest, and is low enough to get rid of all the high frequency content generated because of metal-to-metal rolling contact. Figure 5-5 shows the raw data (left) and filtered data (right) for the experiment conducted at 1.9% commanded creepage.

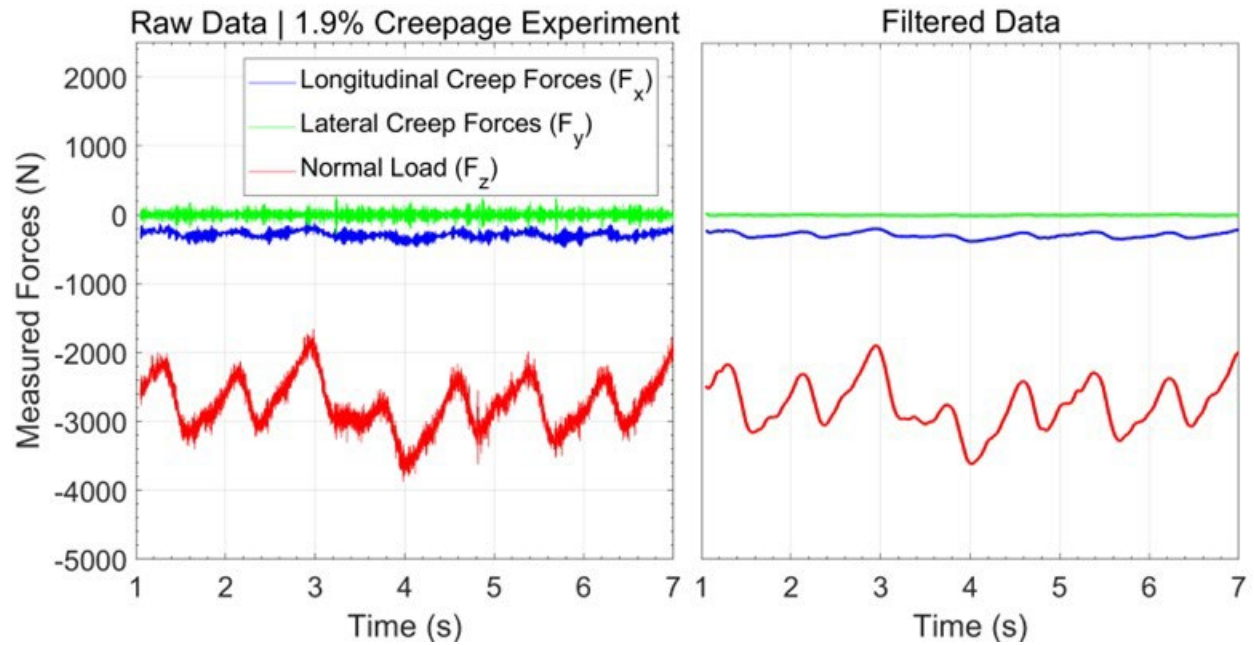


**Figure 5-5** Raw measured force data in Newton (left), digital Butterworth low pass filtered measured force data (filter order = 4, break frequency = 10 Hz, sampling frequency = 2 kHz, creepage: 1.9%) (right)

Due to the presence of these force oscillations in the data, as shown in Figure 5-5, only mean experimental values are used for calculating the creep-creepage curves.

#### 4.6 Checking Mean Normal Load Distribution

Figure 5-6 shows the normal load distribution for the baseline study and angle of attack study experiments; 99% of the mean normal load lies within  $\pm 13\%$  of the mean value. Results indicate a tight band of repeatability of measurements.

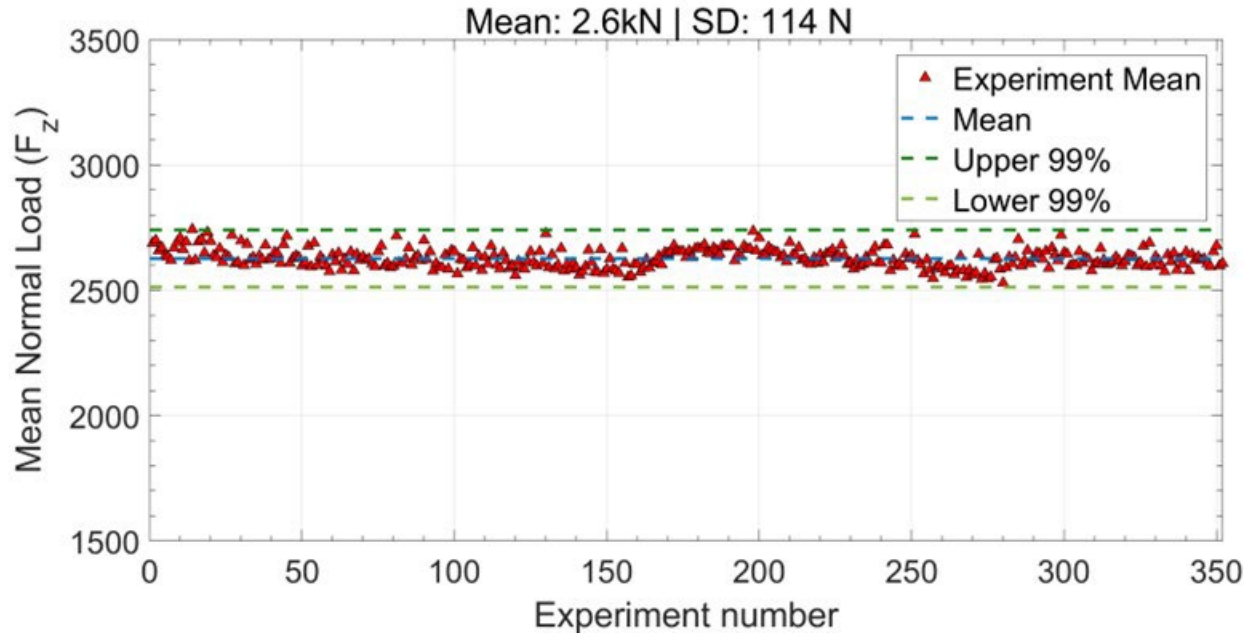


**Figure 5-6** Mean normal load distribution for baseline study and angle of attack study experiments

#### 4.7 Correlation Analysis

Correlation coefficient measures the strength and direction of a linear relationship between two variables whose values lie between -1 and 1. A high correlation coefficient represents a strong linear relationship between the two variables under consideration. A correlation analysis can only indicate the presence and absence of a relationship, not the nature of the relationship. Correlation is not causation, as there is also a possibility of an external variable influencing the results.

As a primary test on the data, a correlation analysis is conducted to verify whether the longitudinal creep force has a high positive correlation with the corresponding normal load measurement points. The Pearson Product Moment Correlation Coefficient is used to estimate the correlation coefficient:

$$r = \frac{n(\Sigma xy) - (\Sigma x)(\Sigma y)}{\sqrt{[n\Sigma x^2 - (\Sigma x)^2] [n\Sigma y^2 - (\Sigma y)^2]}} \quad (15)$$

where  $\Sigma$  is the summation operator,  $x$  is the independent variable, which in this case is the longitudinal creep force, and  $y$  is the dependent variable, which in this case is the normal load.

Figure 5-7 shows 352 data points, where each data point represents the correlation coefficient for commanded normal load and measured longitudinal creep force for each individual experiment. All of the experimental data points in Figure 5-7 are from the baseline study and angle of study. The correlation coefficients are more than 0.8 for almost all experiments, falling below 0.8 for the measurements made at longitudinal creepage values of 0.1% and 0.2%, where the signal-to-noise ratio of the creep force measurement is low. Thus, measurements taken at low creepage values of

0.1% and 0.2% are not included in the creep-creepage curves due to a weak correlation coefficient between the independent and dependent variables. However, a high correlation coefficient does not imply causation. The adhesion model used to govern the creep-creepage behavior between the wheel-rail contact, investigated as part of this research, proposes an increase in the longitudinal creep force for an increase in longitudinal creepage in the micro-creepage region.

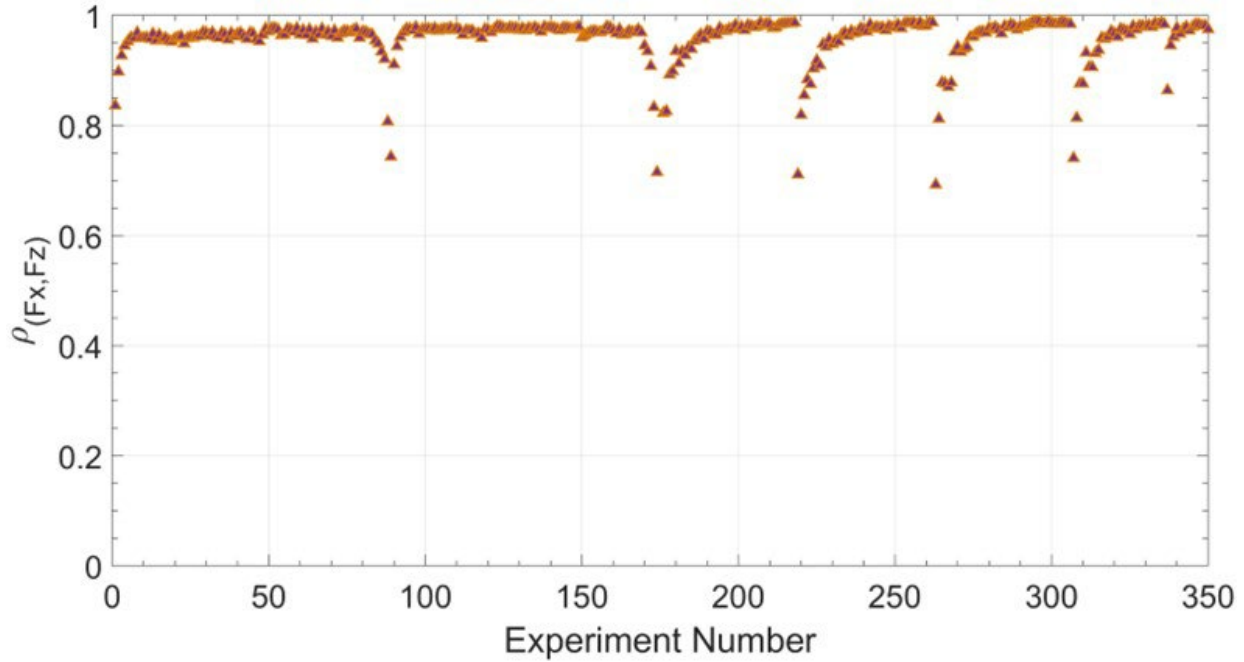


**Figure 5-7** Correlation coefficients between the longitudinal creep force and normal load for baseline study and angle of attack study experiments

#### 4.8 Normalized Creep Force Computation

The longitudinal creep force and normal load force arrays obtained from experiments conducted at a given set of boundary conditions are recorded, and the adhesion coefficients are computed using the relation

$$\mu = \frac{F_x}{F_z} \quad (16)$$

where  $F_x$  is the measured longitudinal creep force, and  $F_z$  is the commanded normal load. The  $L/V$  ratio for all the experiments is computed using the relation

$$\left(\frac{L}{V}\right) \text{ ratio} = \frac{F_y}{F_z} \quad (17)$$

The adhesion coefficients determined for each experiment represent a single point in the creep-creepage curves for the baseline study and angle of attack study experiments, as shown in Figure 5-8, Figure 5-9, and Figure 5-10.

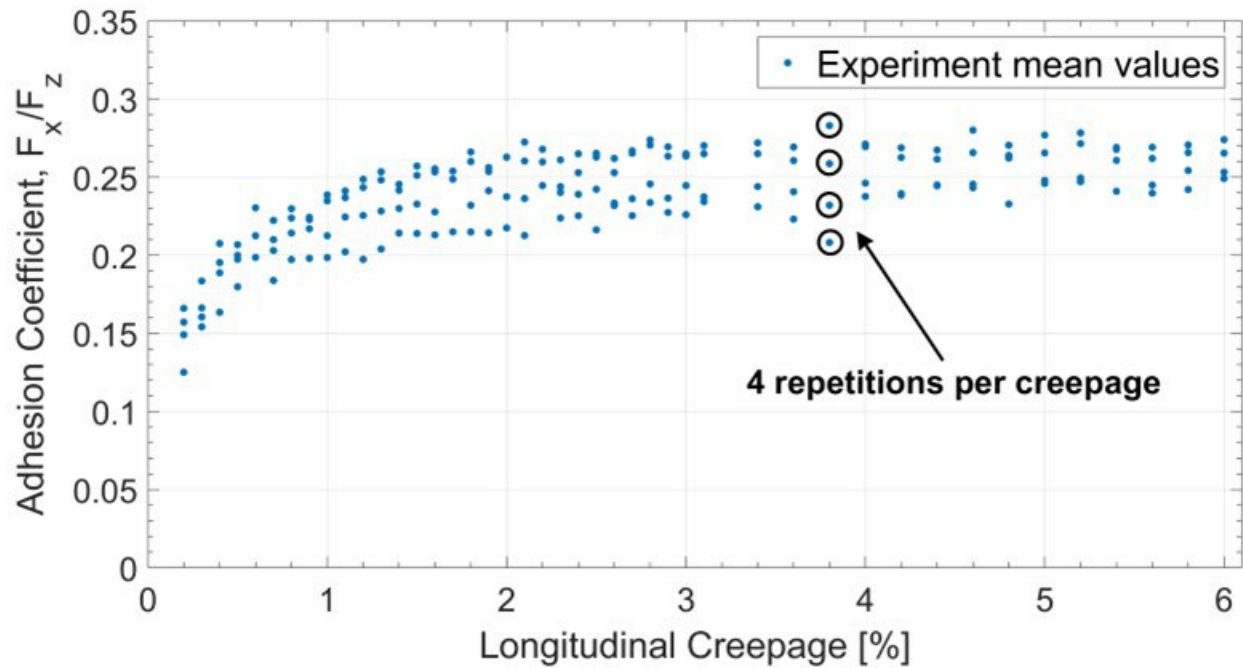


**Figure 5-8** Adhesion coefficients for longitudinal creepages ranging from 0-6% for baseline study experiments

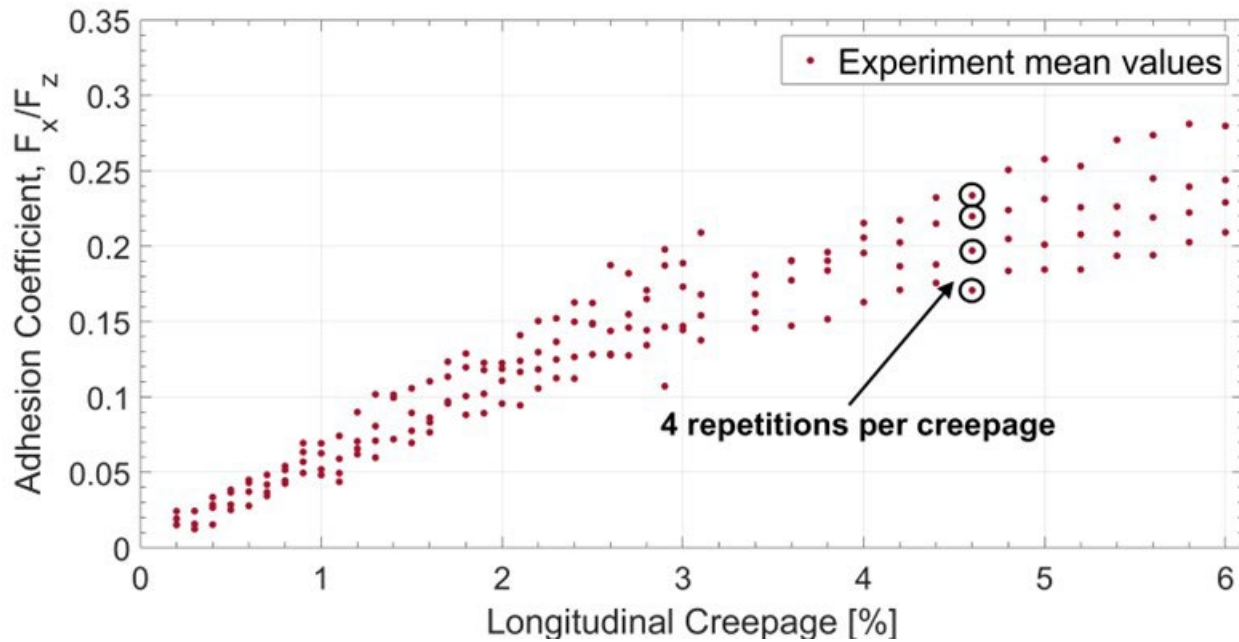


**Figure 5-9** Adhesion coefficients for longitudinal creepages ranging from 0-6% for angle of attack study experiments

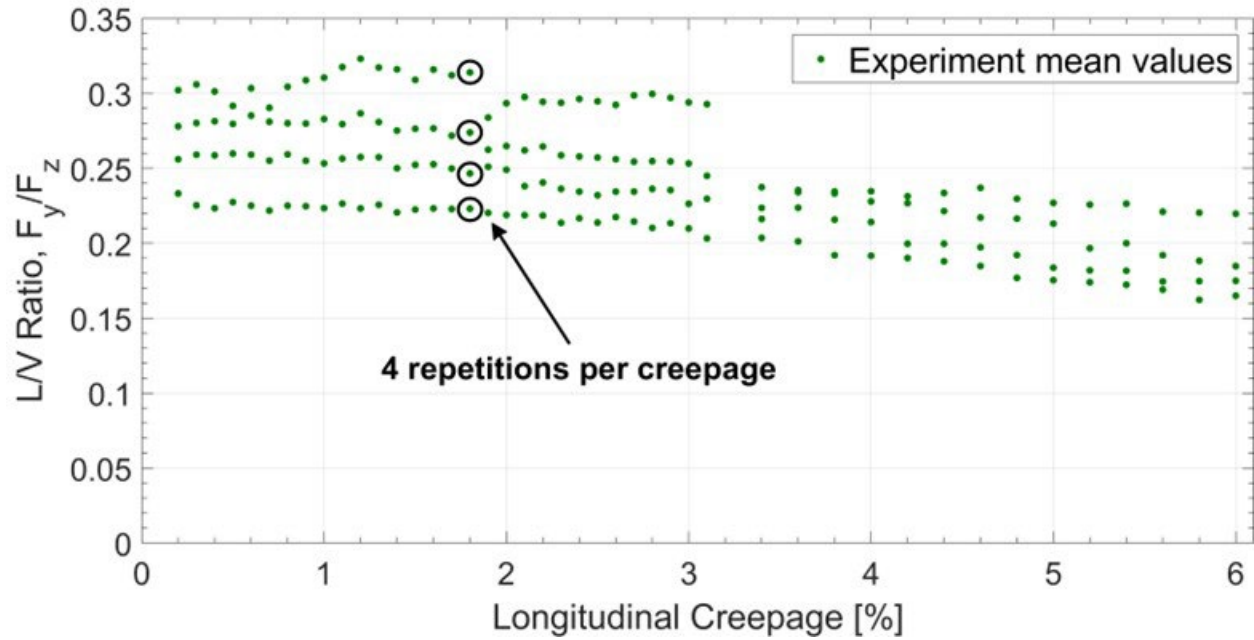


**Figure 5-10** L/V ratios for longitudinal creepages ranging from 0-6% for angle of attack study Experiments

#### 4.9 Experimental Mean of Means

In order to study the creep-creepage curves, mean value of all the measurements at each of the 46 creepage points is computed. A curve fitting method is used to determine the curve through the mean of mean data points for the baseline study and angle of attack study experiments. The results are presented in Chapter 6.

## Chapter 6. Testing Results

The baseline testing results have been highlighted in the previous section, and a detailed step-by-step procedure has been shown on how the data is collected in its raw form, how filtering is performed, and how checks are conducted on the data to make sure that the boundary conditions of the experiment are met. Details and explanation on how the computations are performed and on how the final adhesion-creepage graphs are generated have been included. All the above mentioned steps can be performed using automated test scripts that have been developed as part of this research.

### 5.1 Case Study 1: Influence of Angle of Attack on Adhesion Coefficient and Lateral Stability

Angle of attack is one of the most important parameters affecting the distribution of creep forces at the contact patch, which in turn affects the lateral stability of the locomotives. Contact mechanists around the world are trying to understand the effect of creepage and creep forces at the wheel-rail interface, as it has a direct impact on contact fatigue, hunting, noise, vibration, and other wheel-rail issues [36]. Researchers in the past have experimentally evaluated the effect of angle of attack and humidity on wheel squeal. A twin-disk rolling contact test rig was used and squeal noise was recorded at different angles of attack, rolling speed, and relative humidity. Angle of attack was found to be the dominant factor contributing to wheel squeal, and the results were verified from modal test and finite element analysis [34]. Influence of curve parameters, such as curve radius, circular curve length, and transition curve length, on the rail wear using a virtual prototype technology have been investigated. The study also investigated the effect of introducing cant angle on wheel wear on different radius curves [37]. Formulas for L/V ratios as a function of angle of attack, friction coefficient and contact angle have been developed in the past using the FASTSIM approach and Shen-Hedrick-Elkins creep theory. A derailment criterion is proposed taking into consideration Nadal's criterion. The validity of these equations was verified using a numerical approach and from experimental testing results from scaled testing conducted by Japanese National Railways and full-scale field testing at the Technology Transportation Center, Inc. [38]. An angle of attack of  $2^\circ$  was chosen for the experimental study, as it is commonly observed in the field. In order to compare the results of the angle of attack study, a baseline study was conducted with  $0^\circ$  angle of attack. The angle of attack study experiments simulate an unbanked curve at a constant velocity, while the baseline study experiments simulate a straight track. A series of experiments were conducted to evaluate the adhesion coefficient across a range of creepages from 0% to 6% for both the baseline study and angle of attack study. The relationship between L/V ratio was also evaluated across the creepage range of 0% to 6% for both studies. Regression analysis was conducted to determine the curve fitted through the data, and the functional relationship is discussed during different regions of the adhesion-creepage and L/V ratio-creepage curves.

Each experimental study is conducted by taking closely spaced creepage increments until the maximum value to ensure that all the changing dynamics are captured. For example, in the micro-slip region ( $<1\%$  creepage), the adhesion coefficient rises with a steep slope, as the nature of contact at the wheel-rail interface changes from a pure stick-type contact to more of a slip-type contact. As a result, the creepage increments are kept as low as 0.1% to capture the changing

dynamics. Multiple measurements are taken quasi-statically at each creepage measurement point to ensure that the data collected is repeatable. In order to ensure that there is no day-to-day variability in the data, the experiments are conducted over multiple days. Each experimental study involves 176 individual measurements or experiments conducted over multiple days. A summary of the boundary conditions used for this experiment is listed in Table 6-1.

**Table 6-1** List of testing parameters for baseline and angle of attack studies

<b>Variable Testing Parameters</b>	<b>Baseline Study</b>	<b>Angle of Attack Study</b>
Angle of attack (°)	0	2
<b>Common Testing Parameters</b>		
Wheel profile	Cylindrical	
Roller profile	US136 rail	
Cant angle (°)	0	
Field speed (mph / km/h)	1.86 / 3	
Lab Load (lb. / kN)	562 / 2.5	
Field load (lb. / kN)	71936 / 320	
Lateral displacement (in.)	0	
Contact condition	Dry	
Commanded creepage (%)	0.2 - 6	
Creepage increments (%)	0.1% from 0.2-3%, 0.2% from 3-6%	
Repetitions per creepage point	4	
Experiments conducted	176	
Sampling frequency (kHz)	2	
Measurement time for each experiment (sec.)	7	

### 5.1.1 Baseline Study

The baseline study is conducted to establish a baseline for comparison with the angle of attack studies. The testing parameters for the baseline study are listed in Table 6-1. A non-linear least square method is used to fit a rational polynomial into the data points, as shown in Figure 6-1. Each of the 44 data points represent mean of means of the adhesion coefficient obtained from four experiments conducted at each indicated creepage point. The best-fit curve of the measured data is obtained using a rational model with a R-square value of 0.9466. From Figure 6-1, as the percentage longitudinal creepage increases, the adhesion coefficient increases in a non-linear fashion until it saturates at a value of 0.26 near 2% creepage. When full-size wheel is used, this saturation occurs at smaller creepages [11, 20, 39]. Large contact areas saturate at smaller creepages, if other factors are kept constant. In shorter contact areas, there is less distance for the particles to build elastic deformation. From Figure 6-1, the nature of contact is dominated by a

stick-type contact at micro creepages (<1%), and changes to more of a slip-type contact at higher creepages. The creepage increments are as low as 0.1% in the micro creepage region to capture the changing dynamics from a stick-type contact to a slip-type contact. The 95% prediction bounds obtained from the rational polynomial curve fit indicate a high degree of repeatability of measurements.

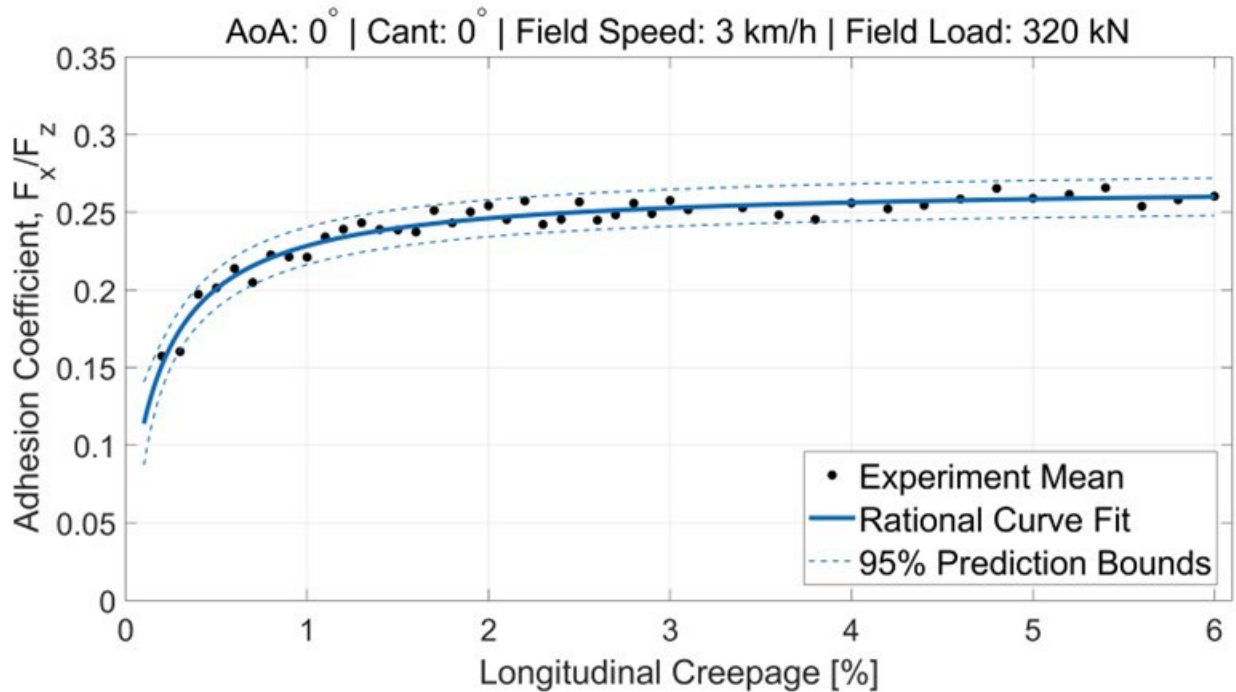


**Figure 6-1** Mean of mean of adhesion coefficients for 0-6% longitudinal creepage with rational fit curve for baseline study experiments

Figure 6-2 shows the variation of L/V ratio as a function of creepage for the baseline study experiments with 0° angle of attack. With 0° angle of attack, the measured lateral creep force should be zero. A very low lateral creep force is measured, as the Rig does not have a zeroing system for an angle of attack positioning system. For the results shown in this section, the angle of attack is set to zero using a different technique. The cylindrical wheel is mounted on the shaft, and the wheel is rotated in contact with the roller. The angle of attack is adjusted dynamically until the mean value of the measured lateral creep force is close to zero.

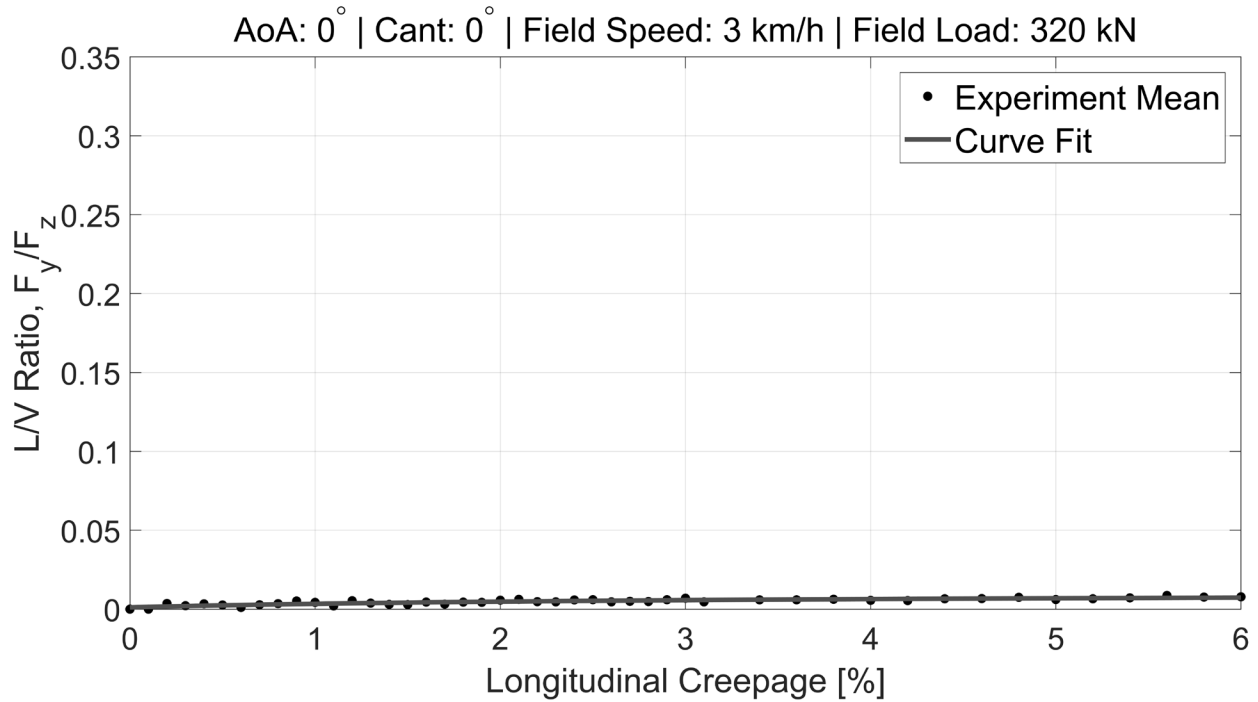


**Figure 6-2** Mean of mean of L/V ratio for 0-6% longitudinal creepage with rational fit curve for baseline study experiments

### 5.1.2 Angle of Attack Study

The testing parameters for the angle of attack study are listed in Table 6-1. Figure 6-3 shows the adhesion coefficient as a function of longitudinal creepage for a railcar navigating an unbanked 2° curve. A non-linear least square method is used to fit a rational polynomial curve in the mean of mean of adhesion coefficients and L/V ratios, as shown in Figure 6-3 and Figure 6-4. As the percentage at longitudinal creepage increases, the adhesion coefficient increases in a non-linear fashion and does not saturate until the commanded longitudinal creepage value of 6%.

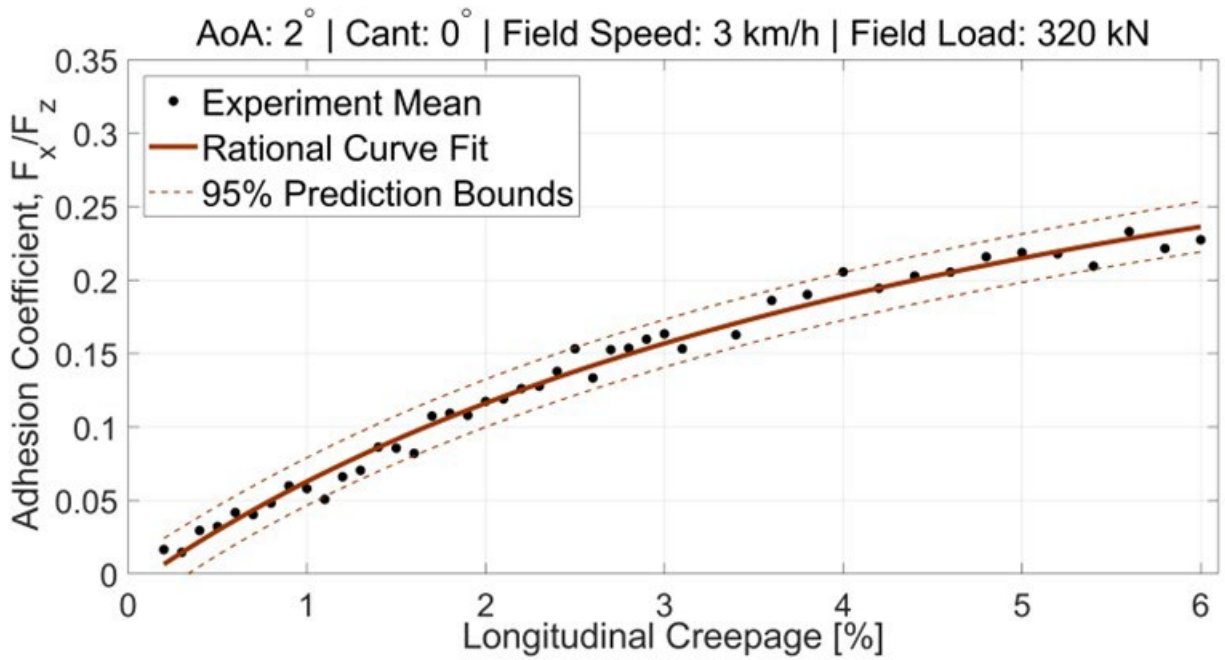


**Figure 6-3** Mean of mean of adhesion coefficients for 0-6% longitudinal creepage with rational fit curve for angle of attack study experiments

Figure 6-4 shows the L/V ratio as a function of longitudinal creepage for a 2° angle of attack. If the angle of attack is kept constant, the lateral creep force, for a given normal load, is a function of creepage at the wheel-rail contact patch. Each of the 44 data points indicated in Figure 6-4 represents the mean of means of the L/V ratio obtained from four experiments conducted at each creepage point. The L/V ratio is lower than expected, as flange contact does not happen due to a cylindrical wheel profile. The curve fit on the measured data was obtained using a rational polynomial model with a R-square value of 0.9867. The 95% prediction bounds, as shown in Figure 6-4, indicate a high degree of repeatability of measurements. From Figure 6-3 and Figure 6-4, it is observed that as longitudinal creepage increases, the lateral creep force decreases, while the longitudinal creep force increases.

The general model with goodness of fit parameters determined from the best fit curves for the adhesion coefficient curve and L/V ratio are listed in Table 6-2.

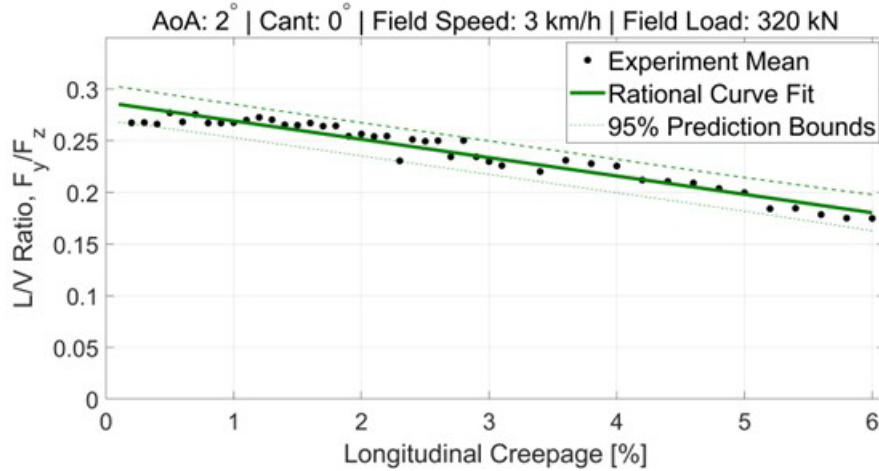


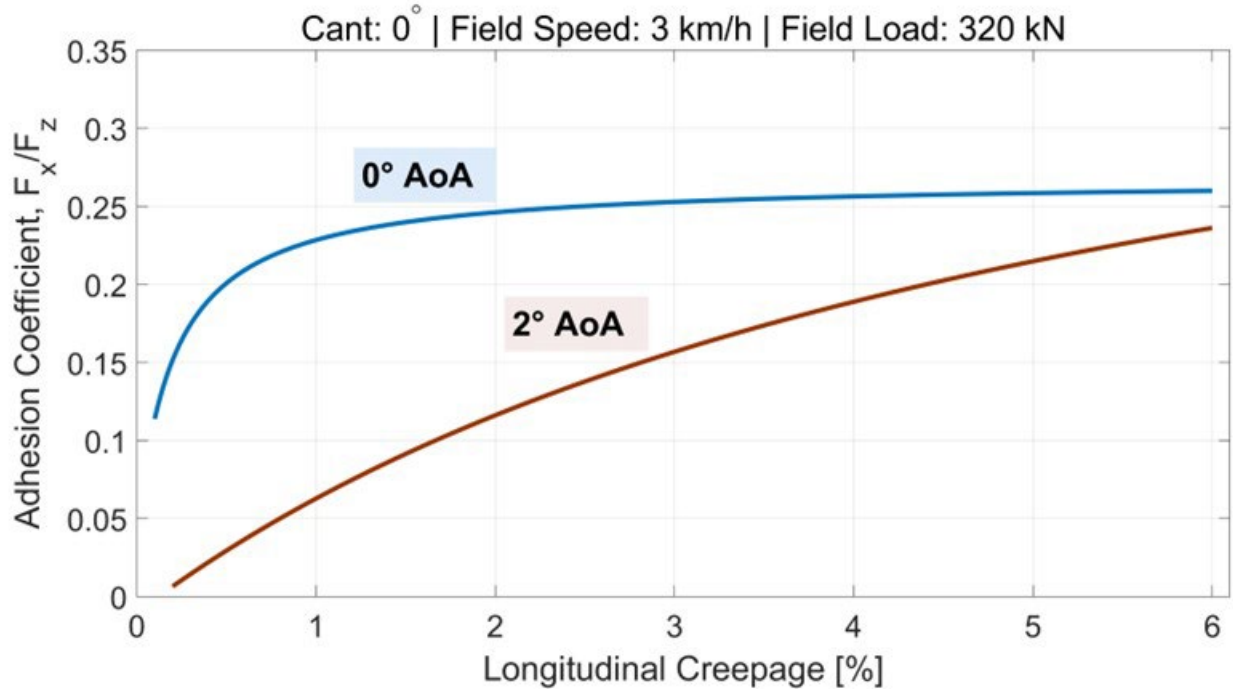
**Figure 6-4** Mean of mean of L/V ratio for 0-6% longitudinal creepage with rational fit curve for angle of attack study experiments

**Table 6-2** Regression model parameters for creep-creepage curves for baseline study and angle of attack study

Study	Baseline study	Angle of attack study	
Curve type	Adhesion-creepage	Adhesion-creepage	L/V ratio-creepage
General model	$f_1(x) = \frac{p_1 * x + p_2}{x + q_1}$		
p <sub>1</sub> (with 95% confidence bounds)	0.2676 (0.2632, 0.272)	0.4595 (0.3967, 0.5223)	-66.08 (-1.281e+04, 1.268e+04)
p <sub>2</sub> (with 95% confidence bounds)	0.008255 (-0.01098, 0.02749)	-0.05515 (-0.09783, -0.01247)	1070 (-2.046e+05, 2.068e+05)
q <sub>1</sub> (with 95% confidence bounds)	0.2077 (0.09755, 0.3178)	5.438 (3.967, 6.909)	3727 (-7.131e+05, 7.205e+05)
Sum of Squares due to Error (SSE)	0.001375	0.002529	0.002496
R-square	0.9466	0.9867	0.9383
Adjusted R-square	0.944	0.9861	0.9353
Root Mean Square Error (RMSE)	0.005791	0.007854	0.007802

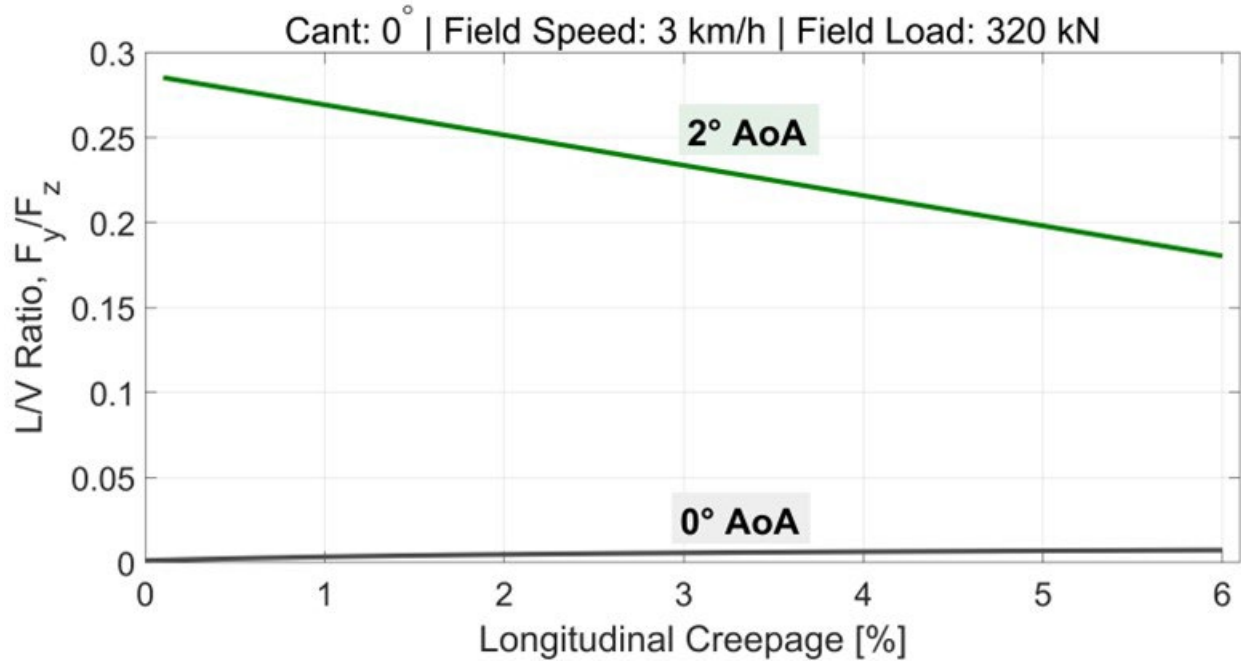
### 5.1.3 Comparison of Results for Baseline Study and Angle of Attack Study

Figure 6-5 compares the adhesion-creepage behavior for the baseline study and angle of attack study. The data shown is replotted from Figure 6-1 and Figure 6-3. Results indicate that the maximum adhesion coefficient in the measurement range drops for the angle of attack study due to an increase in lateral creep forces as a result of the angle of attack.



**Figure 6-5** Comparison of adhesion coefficient as a function of longitudinal creepage for baseline and angle of attack studies

Figure 6-6 compares the L/V ratio as a function of longitudinal creepage for the baseline study and angle of attack study. The data has been replotted from Figure 6-2 and Figure 6-4. It is observed that as the angle of attack is kept constant, the lateral creep force, for a given normal load, is a function of creepage at the wheel-rail contact. The Roller Rig currently does not have a zeroing system for the angle of attack. An indirect method is used to zero the angle of attack. The wheel and roller were run in contact, and the yaw angle is adjusted until the mean lateral creep force became zero, and this orientation was considered to be at zero angle of attack. The maximum lateral creep force for the baseline study, measured at 6% longitudinal creepage, is ~19 N.



**Figure 6-6** Comparison of L/V ratio as a function of longitudinal creepage for baseline and angle of attack studies

After concluding the angle of attack study experiments, a series of tests were conducted to evaluate the adhesion-creepage behavior. The measured adhesion coefficients for the same experimental conditions were lower than the results for the angle of attack case study. This was due to the fact that all the experimental conditions for the angle of attack case study were tightly controlled, except for the wheel and roller contact surface conditions. It was observed that continuously running experiments led to accumulation of wear debris at the wheel-rail contact. The resulting wear debris behaved like a “natural” third-body layer by creating an interfacial layer between the wheel and roller, which affects the contact forces. Based on the initial analysis, it is found that the wear debris is acting like a positive friction modifier. The measured adhesion coefficients reported increased values with wheel and roller contact surfaces contaminated by wear particles, as compared to clean surfaces. In order to further evaluate the effect of wear debris, the contact surface condition is made a controlled parameter for the case study presented in the next section.

## 5.2 Case Study 2: Influence of Water Lubricated Wheel and Rail on Adhesion-Creepage Behavior

Wheel-rail contact inevitably operates in a contaminated contact condition. Natural third-body layers, such as rainwater, wear debris, and leaves, act as Top-of-Rail (TOR) friction modifiers and affect the adhesion levels between the wheel and rail. The third-body layer acts like an interfacial layer in the wheel-rail contact that separates the two primary bodies, which in this case are the wheel and roller.

Presence of leaves between the wheel-rail interface acts like a negative TOR friction modifier. Ishizaka et al. [40] studied the bonding mechanism between a leaf film and rail by developing

laboratory-based and field-based models from past studies. They reported adhesion coefficients below 0.1 with dry leaf, and lower adhesion coefficients of around 0.05 with wet leaf, between the wheel-rail interface. Chen et al. [41] studied the influence of water temperature on the adhesion coefficient and central nominal water film thickness. They reported an increase in adhesion coefficient and a decrease in central nominal water film thickness as the water temperature increases. Trummer et al. [42] used the experimental results from a tram wheel test rig to create a model to predict the drop in adhesion coefficient in the presence of small amounts of water in between the wheel-rail contact patch. They observed adhesion values as low as 0.06 at high creepage with only wear debris and little water present in the contact. Their model results have good agreement with experimental data from locomotive tests in dry and wet conditions.

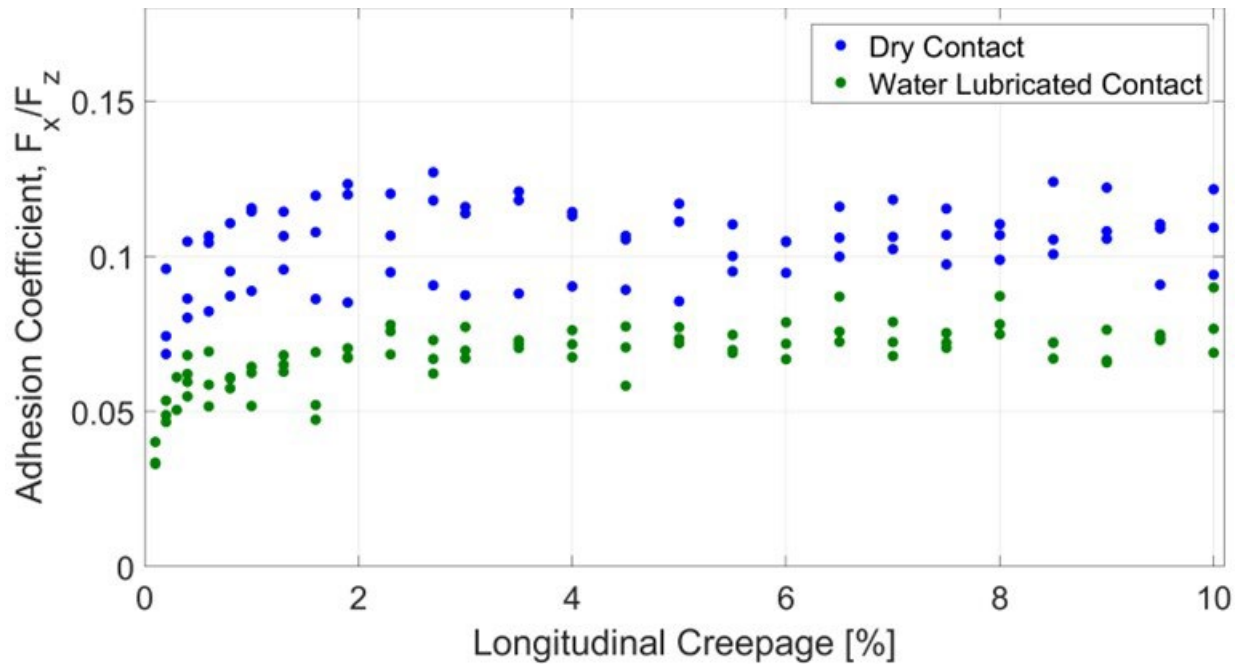
A summary of testing parameters for dry contact and water lubricated contact studies is given in Table 6-3. A flanged wheel profile is used for conducting these studies, compared to a cylindrical wheel profile for the baseline and angle of attack studies. Adhesion-creepage behavior is experimentally evaluated for a creepage range from 0 to 10% for both the baseline study and angle of attack study. The wheel and roller contact surface condition is also controlled for the experiments conducted as part of the current case study. As a result, the wheel and roller contact surfaces is cleaned with a fabric cloth for all experiments conducted for the dry conditions. The cleaning exercise is performed before conducting each experiment in order to prevent formation of any wear debris at the wheel-rail contact. For the experiments conducted to study the adhesion-creepage behavior of water lubricated experiments, a brush dipped in water was used to constantly lubricate the wheel and rail contact surfaces for the entire duration of test. This method ensured that no wear debris was allowed to accumulate at the wheel and rail contact surfaces.

**Table 6-3** Summary of testing parameters for dry contact and water lubricated contact studies

<b>Variable Testing Parameters</b>	<b>Dry Wheel and Rail Study</b>	<b>Water Lubricated Wheel and Rail Study</b>
Contact condition	Clean and dry	Water lubricated
<b>Common Testing Parameters</b>		
Wheel profile	Flanged (Conicity 1/ 20)	
Roller profile	US136 rail	
Angle of attack (°)	0	
Cant angle (°)	0	
Field speed (mph / km/h)	1.86 / 3	
Lab load (lb. / kN)	597 / 2.66	
Field load (lb. / kN)	76416 / 341	
Lateral displacement (in.)	0	
Commanded creepage (%)	0.2 - 10	
Repetitions per creepage point	3	

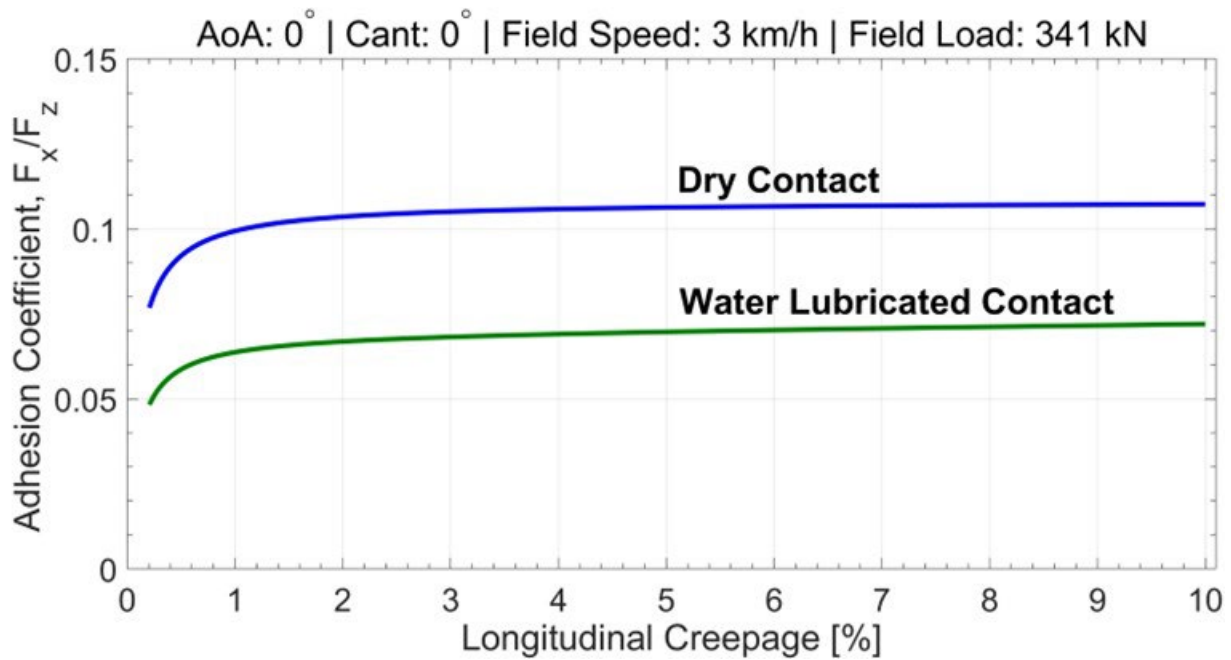
Experiments conducted	81
Sampling frequency (kHz)	2
Measurement time for each experiment (sec.)	7

Figure 6-7 shows the measured adhesion coefficients between the wheel and roller from 0-10% longitudinal creepage. Each point in Figure 6-7 represents an individual experiment performed under testing conditions mentioned in Table 6-3.



**Figure 6-7** Adhesion coefficients for longitudinal creepages ranging from 0-6% for dry contact and water lubricated contact studies with contact surface condition as a controlled parameter

Figure 6-8 shows the adhesion-creepage behavior for dry contact and water lubricated contact studies. The water lubricated contact study shows a clear drop in peak adhesion coefficient over the dry contact study. The dry contact study experiments peaks at an adhesion coefficient of  $\sim 0.11$ , and the water lubricated contact experiments peaks at  $\sim 0.07$ . Both the wheel and roller contact surfaces are continuously lubricated with water at the trailing edge using brushes. Another important thing to note is that to minimize the wear debris build-up at the wheel-rail contact, the wheel and roller contact surfaces are cleaned to remove any contamination before conducting each experiment.



**Figure 6-8** Rational curve fit of experimental data points for dry and water lubricated studies showing variation of adhesion coefficients as a function of longitudinal creepage

In order to further evaluate the effect of the wear debris from the wheel surface at the wheel-rail contact, there is a need to study its effect over increased periods. Case Study 3 discusses the results from analysis of adhesion coefficient at wheel-rail contact.

### 5.3 Case Study 3: Effect of Wheel Wear on Adhesion-Creepage Behavior

Wear debris resulting from high traction forces at the wheel-rail contact acts like a third-body layer at the interface of the two bodies. It consists of particles stemming from both the wheel and rail surfaces, which have a direct effect on the wheel-rail contact mechanics. Beagley et al. [43] reported that rust particles constituted a major part of the railhead debris that maintains high adhesion in dry conditions. Adhesion coefficients ranging between 0.3 and 0.5 were reported for dry contact conditions, depending on the debris coverage. They observed a reduction in friction if the powder particles were mixed with a substantial portion of oil. Nakahara et al. [44] used a twin disk testing setup to investigate the effect of surface oxide layer at the wheel-rail contact on the traction coefficients. Tests carried out with dry contact condition and 0.7% creepage reported an increase in traction coefficients with time. The presence of a hard oxide of iron called hematite ( $\alpha - \text{Fe}_2\text{O}_3$ ) was attributed to the increase in traction coefficient measurements. A peak traction coefficient of  $\sim 0.5$  was reported.

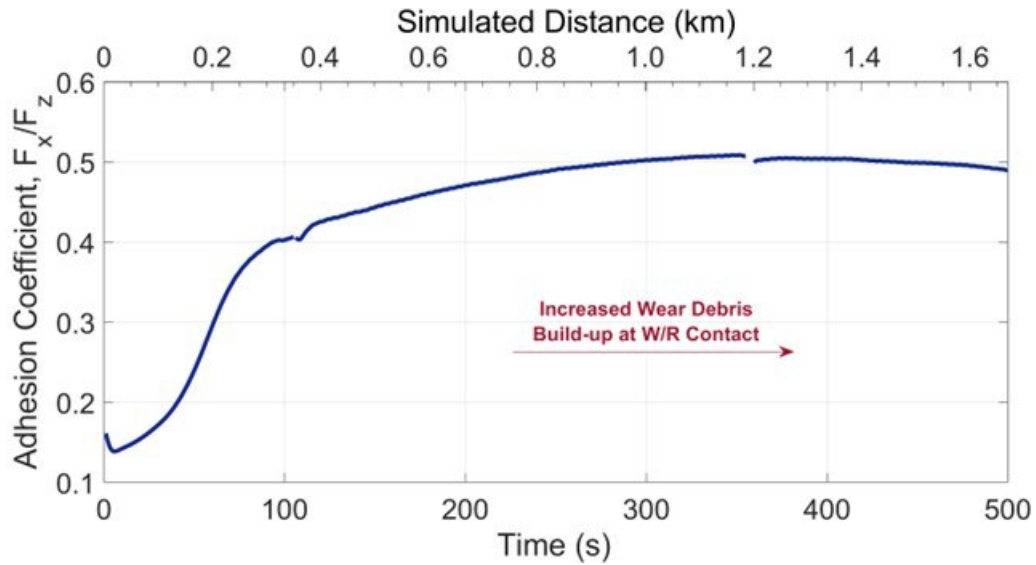
Experimental testing is conducted on the Roller Rig to evaluate the build-up of wear particles between the wheel-rail contact surfaces on the adhesion coefficients. In order to accelerate the process of wear build-up, the longitudinal creepage at the wheel-rail contact is kept constant at 2% for the complete testing duration. Quasi-static measurements are carried out to simulate high normal field loads of 278 KIPS on the rig for a duration of 500 seconds to further accelerate the wear rate. This normal load corresponds to a fully loaded freight railcar. The contact stress is

estimated to be ~ 176 ksi based on Hertzian contact theory. The complete list of testing parameters for the experiment is listed in Table 6-4.

**Table 6-4** Summary of boundary conditions for the wear test

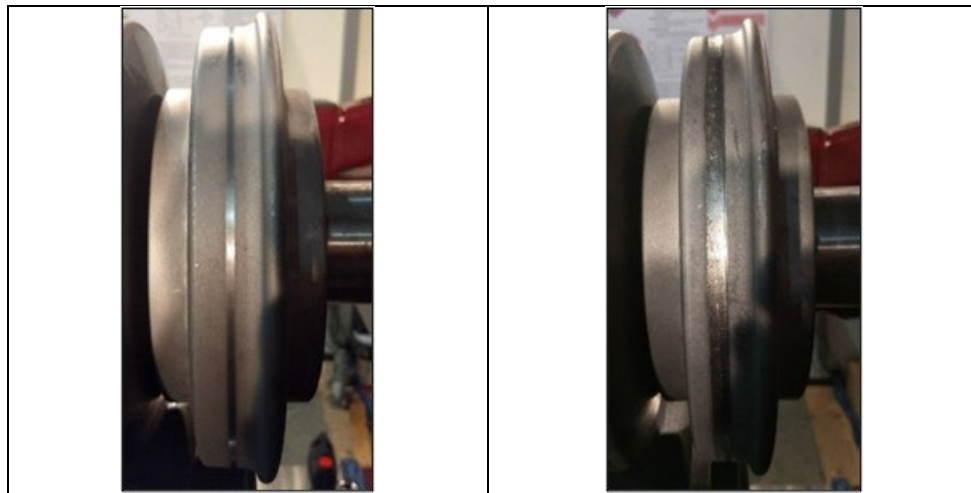
Parameter	3BL Study
Wheel profile	Flanged (1/20 conicity)
Roller profile	US136 rail
Angle of attack (°)	0
Cant angle (°)	0
Field speed (mph)	1.86
Lab load (lb. / kN)	2163 / 9.62
Field load (lb. / kN)	276,864 / 1232
Lateral displacement (in.)	0
Start condition	Clean and Dry
Commanded creepage (%)	2
Sampling frequency (kHz)	2
Measurement time (sec.)	500

Figure 6-9 shows a time series analysis of adhesion coefficients. Both the wheel and roller surfaces are cleaned before the start of the experiment. The adhesion coefficient at the start of the experiment is ~0.16. High creepage and normal load conditions cause an increase in the build-up of wear particles at the wheel-rail contact patch. For the first ~100 seconds, the adhesion coefficient increases steeply in a non-linear fashion. The rate of increases then decreases thereafter until a peak adhesion coefficient of ~0.5 is observed at ~350 seconds.



**Figure 6-9** Experimental testing results of time series analysis of adhesion coefficients at high creepage and normal load

Figure 6-10 shows the wheel contact surface profile before and after conducting the wear testing. Figure 6-10 shows an increase in the wheel tread width due to wear from the wheel's contact surface. High traction forces observed after ~100 seconds accelerate the wear process at the wheel's contact interface. A large amount of debris particles is collected from the wheel surface after the wear test using fabric sheets.



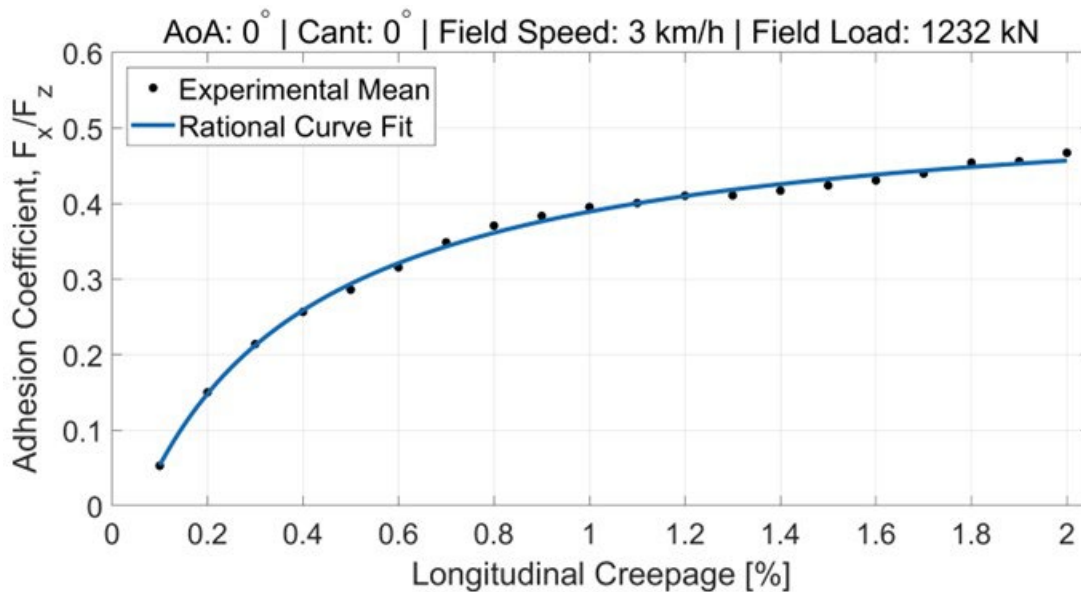
**Figure 6-10** Comparison of wheel profile before conducting the wear test experiment (left) and after conducting the wear test experiment (right)

Figure 6-11 shows the roller profile before and after conducting the wear testing. The roller contact surface does not visibly change before and after the wear test.



**Figure 6-11** Comparison of roller profile before conducting the wear test experiment (left) and after conducting the wear test experiment (right)

Figure 6-12 shows experimentally-measured data points from a 20-point adhesion-creepage experimental study. The current experimental design is different from previous reported results, as the wheel and roller surfaces are not cleaned before conducting the measurements. The wheel and roller surfaces are run in contact. Starting with perfectly clean and dry surfaces, the traction coefficients rise initially until they reach a stable value, as shown in Figure 6-9. The 20 experimental measurements shown in Figure 6-12 are performed after the traction coefficients reached a stable value. The adhesion coefficients from the current experiments are higher than those reported in Figure 6-1 and Figure 6-8, due to presence of naturally generated third-body layer deposits (as a result of wear of wheel and/or roller) between the wheel-roller contact.



**Figure 6-12** Adhesion coefficients for 0-2% longitudinal creepage with rational fit curve for Case Study 3 experiments

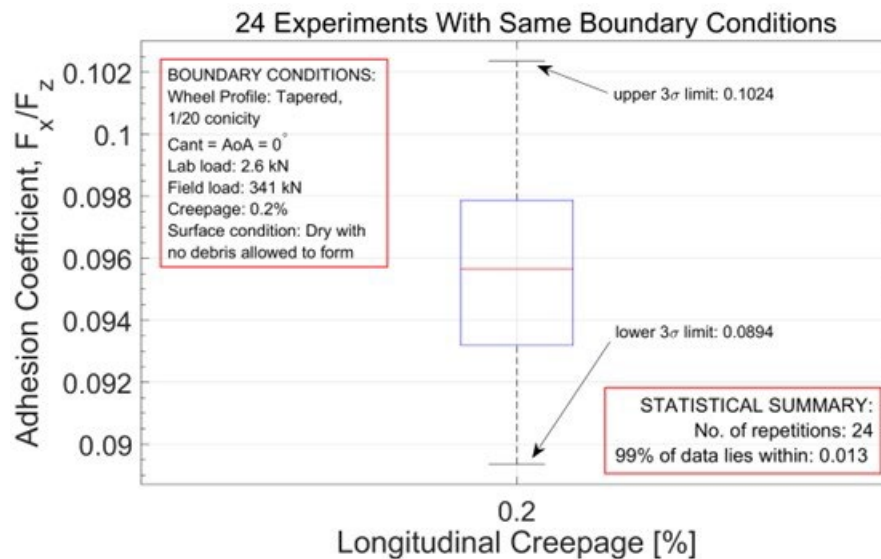
### 5.4 Repeatability of Measurements

Repeatability of measurements is the closeness of agreement between the results of successive measurements of the same measurand, carried under the same conditions of measurement. A system design is repeatable if it can consistently produce measurements with a low spread.

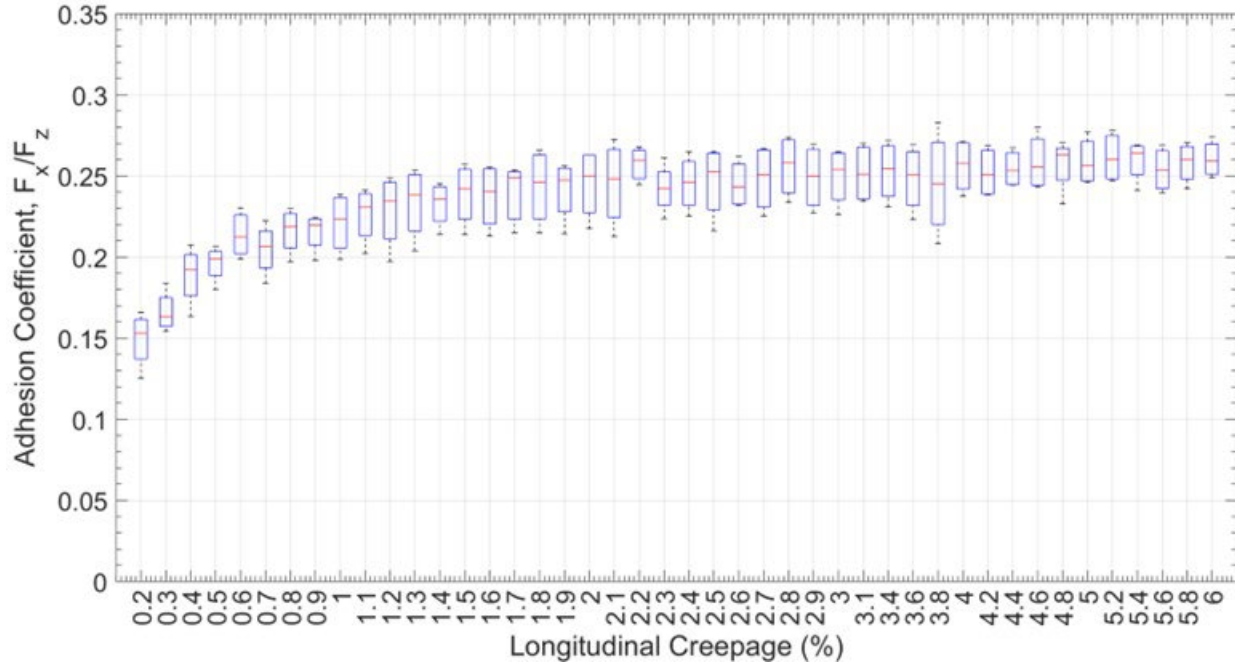
The Rig is designed to make consistent and repeatable measurements with a high degree of precision. Therefore, it is very important to evaluate the repeatability of the Rig across multiple experiments.

Figure 6-13 shows a box-and-whisker plot constructed from measurements from 24 experiments with the same exact boundary conditions. The mean value of adhesion coefficients was 0.0956, and 99% of the data lies within 6.8% of the mean. The Roller Rig has a very tight band of measurements indicating a high repeatability of measurements.

Figure 6-14 shows a boxplot analysis of the adhesion coefficients from all the experiments conducted for the baseline study presented in Section 6.1.1. Each box in the figure represents the adhesion coefficients for the experiments from specific creepage points. There are no outliers reported in this boxplot analysis, and the worst case of reported repeatability among all similar measurements is  $\pm 17\%$  about the median.

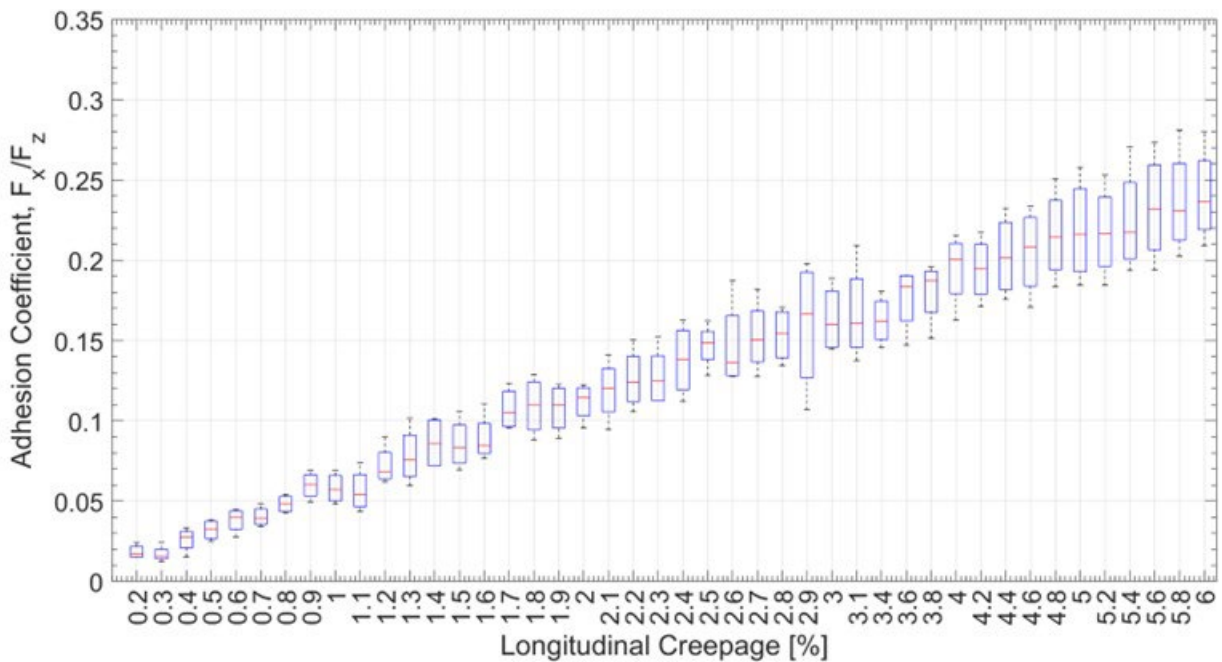


**Figure 6-13** Boxplot analysis of adhesion coefficients taken from 24 experiments conducted with exactly the same boundary conditions



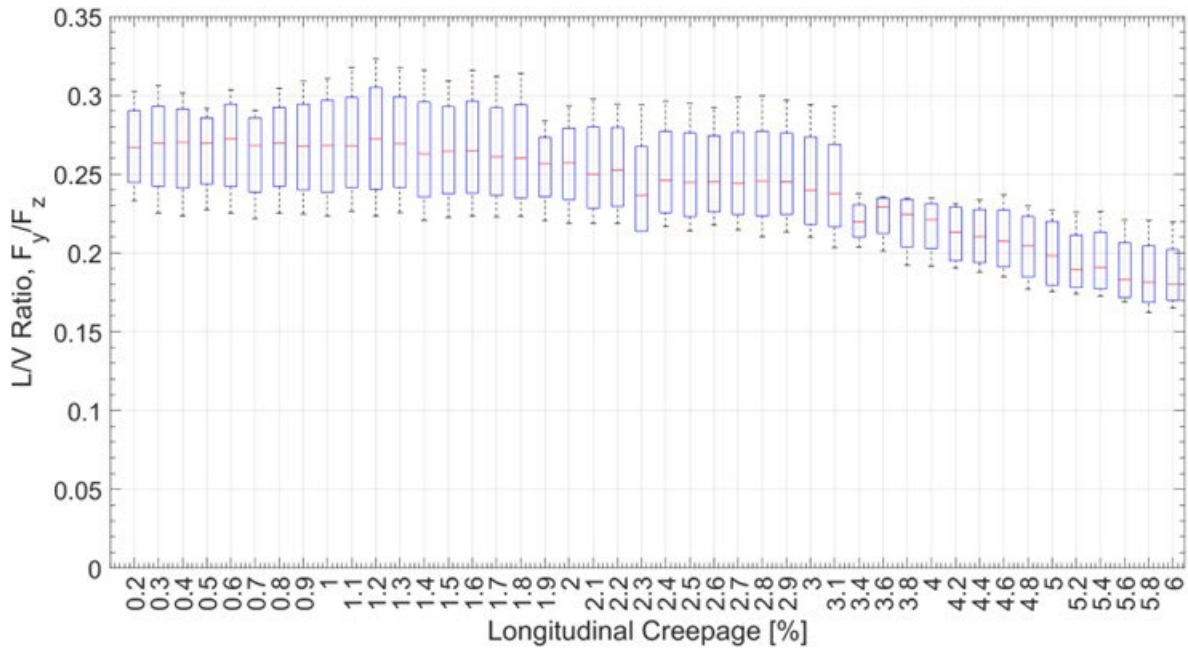
**Figure 6-14** Boxplot analysis of adhesion coefficients for experiments from specific creepage points for the baseline study experiments

Figure 6-15 shows a boxplot analysis of the adhesion coefficients from all the experiments conducted for the angle of attack study presented in Section 6.1.2. Each box in the figure represents the adhesion coefficients for the experiments from specific creepage points. There are no outliers reported in this boxplot analysis, and the worst case of reported repeatability among all similar measurements is  $\pm 27\%$  about the median.



**Figure 6-15** Boxplot analysis of adhesion coefficients for experiments from specific creepage points, for the angle of attack study experiments

Figure 6-16 shows a boxplot analysis of the L/V ratios from all the experiments conducted for the angle of attack study. Each box in the figure represents the L/V ratios for the experiments from specific creepage points. There are no outliers reported in this boxplot analysis, and the worst case of reported repeatability among all similar measurements is  $\pm 18\%$  about the median.



**Figure 6-16** Box plot analysis of L/V ratios for experiments from specific creepage points for the angle of attack study experiments

## **Chapter 7. Summary and Future Studies**

This chapter presents a summary of the work done and recommendations for future studies.

### **6.1 Summary**

The development of the mechanical and electromechanical components of the Virginia Tech – Federal Railroad Administration (VT-FRA) Roller Rig was successfully completed in 2016. The Rig was then ready to be used for conducting experimental studies to understand the complex mechanics and dynamics that occur at the wheel-rail contact patch, with an aim to improve railway operational safety and efficiency.

The main purpose of this research is to experimentally evaluate rolling contact and slip dynamics models developed using the Virginia Tech – Federal Railroad Administration (VT-FRA) Roller Rig. The creep-creepage measurements made, as a part of this study, can be used to validate contact models that attempt to calculate the creep forces and moments at the contact patch under different boundary conditions. This work will shed light on the effect of angle of attack, wheel wear, Top-of-Rail (TOR) friction modifiers, and third-body layers on the changing creep force distribution at the wheel-rail contact patch. Baseline testing results were also established, and each of these experimental studies were compared to the baseline conditions to further evaluate the results. The measured adhesion coefficients and L/V ratios, as part of the creep-creepage measurements, are used to analyze the experimental studies. A repeatability analysis is conducted to establish the 99% confidence intervals for the commanded normal load, adhesion coefficient, and L/V ratio measurements.

Experimental testing workflow is established to make reliable and repeatable measurements on the Roller Rig. MATLAB routines using scripts and custom-made functions is developed with an aim to automate the data processing of measurements made across multiple individual experiments, conducted as part of an experimental study. More details can be found in Chapter 5.

A time and frequency domain analysis of the normal load measurements is conducted in order to analyze trends in the waveform, and to determine the dominant frequencies with an aim to shed light on the Roller Rig's wheel-rail contact characteristics.

### **6.2 Recommendations for Future Studies**

All the measurements made on the Roller Rig are done quasi-statically, which means that all the boundary conditions are kept constant for each experiment. No dynamic measurements can be conducted, as the positioning systems of the Roller Rig, namely, the normal load, angle of attack, cant angle, and lateral displacement, cannot be adjusted dynamically during a test due to a position control feedback loop architecture of the linear actuators. Recently, force control feedback loops have been developed and tuned for the Rig, which has enhanced the capabilities of the Rig. It is now possible to dynamically regulate the positioning systems during a measurement. This development will allow the Rig to better simulate the field conditions. Some of the studies possible with the Roller Rig include:

1. Dynamic testing to evaluate the creep force distribution at the contact patch at different points along the lateral surface profile of the wheel. The equivalent adhesion coefficient due to flange contact and tread contact can be experimentally evaluated, and the L/V ratios obtained can be compared with Nadal's empirical formulas to check the validity of the equation under flange climb and derailment scenarios. The Roller Rig can also be used to study the effect of high angle of attack and time-varying spin moments on the generation of squeal noise when a railcar negotiates a curve. Studies on velocity-dependent coefficient of friction, falling friction phenomenon, and the effects of both positive and negative creepage at the wheel-rail contact patch on the adhesion levels can be experimentally analyzed in greater detail.
2. With a high data acquisition bandwidth of 48 kHz, along with a dedicated operational mode of the force measurement system to capture high frequency content of the experiments, there is a tremendous scope for conducting vibration analysis to study its effects on the creep force and moment distribution at the contact patch, and its influence on passenger comfort.
3. Wheel-rail wear analysis can be conducted to study the evolution of wheel profile from newly-machined surface condition to worn wheel with conformal contact. The changing creep forces and its distribution can be studied. Moreover, more light can be shed on the anecdotal evidence of wheelsets behaving differently after undergoing truing, which has been attributed to the influence of tool marks on the wheel-rail contact patch dynamics. Incidences of low speed derailment that have been reported by field engineers, under such circumstances, can be evaluated in great detail in a controlled laboratory environment. Quantifying the amount of wear and corresponding it with the experimental studies can help validate theoretical models that calculate the amount of wear for different wheel-rail contact conditions.
4. Studies on the effects of Top-of-Rail (TOR) friction modifiers on the creep force and moment distribution at the contact patch can be extended beyond the currently reported results with water lubricated wheel-rail contact condition. Potentially, research can be conducted to compare sand particles, which are currently used to increase wheel-rail adhesion in the railroad industry, with other third-body materials, such as hematite ( $\text{Fe}_2\text{O}_3$ ), which has been also been reported in the literature to act like a positive friction modifier. Effect of these positive friction modifiers on wheel-rail wear changes in surface conditions can also be studied at different adhesion coefficients. The effect on the rate of lubrication can also be analyzed, and a comparison can be made with the baseline testing results.

## References

- [1] Keylin, A., M. Ahmadian, M. Taheri, and A. Tajaddini, "*Wheel-Rail Contact Characteristics on a Tangent Track Vs a Roller Rig*". ASME 2012 Rail Transportation Division Fall Technical Conference, 2012(45073): p. 1-9.
- [2] Jaschinski, A., H. Chollet, S. Iwnicki, A. Wickens, and J. von Würzen, "*The Application of Roller Rigs to Railway Vehicle Dynamics*". *Vehicle System Dynamics*, 1999. **31**: p. 345-392.
- [3] W. Zhang, H.D., Z. Shen, *Handbook of Railway Vehicle Dynamics*. Roller Rigs. 2006.
- [4] Keylin, A., "*Analytical Evaluation of the Accuracy of Roller Rig Data for Studying Creepage in Rail Vehicles*", in *Mechanical Engineering*. 2012, Virginia Tech: Blacksburg.
- [5] Meymand, S.Z., M. Hosseinipour, and M. Ahmadian, "*The Development of a Roller Rig for Experimental Evaluation of Contact Mechanics for Railway Vehicles*". Joint Rail Conference, 2015(56451): p. V001T10A007.
- [6] Knothe, K., "*History of wheel/rail contact mechanics: From Redtenbacher to Kalker*". *Vehicle System Dynamics*, 2008. **46**: p. 9-26.
- [7] Fletcher, D.I. and S. Lewis, "*Creep curve measurement to support wear and adhesion modelling, using a continuously variable creep twin disc machine*". *Wear*, 2013. **s 298–299**: p. 57–65.
- [8] R., L. and O. U., *Wheel–rail interface handbook*. 2009: Cambridge: Woodhead Publishing Limited.
- [9] Olofsson, U., Y. Zhu, S. Abbasi, R. Lewis, and S. Lewis, "*Tribology of the wheel–rail contact – aspects of wear, particle emission and adhesion*". *Vehicle System Dynamics*, 2013. **51**: p. 1091-1120.
- [10] Zhu, Y., "*Adhesion in the wheel–rail contact under contaminated conditions [Licentiate thesis]*", in *Department of Machine Design*. 2011, KTH Royal Institute of Technology: Stockholm.
- [11] S., I., *Handbook of Railway Vehicle Dynamics*. 2006: Taylor & Francis Group.
- [12] .Kalker, J.J., "*Wheel-rail rolling contact theory*". *Wear*, 1991. **144**(1-2): p. 243-261.
- [13] Meymand, S., A. Keylin, and M. Ahmadian, "*A survey of wheel–rail contact models for rail vehicles*". *Vehicle System Dynamics: International Journal of Vehicle Mechanics and Mobility*, 2016. **54**: p. 1-43.
- [14] "*WRI 2017 Conference*". *Wheel-Rail Interaction Fundamentals* [cited 2018 May 3]; Available from: <https://www.wheel-rail-seminars.com/archives/2017/pc-papers/presentations/PC%201-3%20Wheel-Rail%20Interaction%20Fundamentals%20WRI%202017%20-%2020170604.pdf>.
- [15] Andersson, E., M. Berg, S. Stichel, and C. Casanueva, "*Rail Systems and Rail Vehicles*". 2016, KTH Royal Institute of Technology: Stockholm.
- [16] Arnold, E., *Tribology: Friction and Wear of Engineering Materials*. 1992, London: Ian M. Hutchings. 273.
- [17] Harrison, H., T. McCanney, and J. Cotter, "*Recent developments in coefficient of friction measurements at the rail/wheel interface*". *Wear*, 2002. **253**: p. 114-123.
- [18] Ertz, M. and F. Bucher, "*Improved Creep Force Model for Wheel/Rail Contact Considering Roughness and Temperature*". *Vehicle System Dynamics*, 2003. **37**: p. 314-325.

- [19] Hou, K. and J. Kalousek, "*Thermal effect on adhesion in wheel/rail interface*". 2000. p. 239-244.
- [20] Polach, O., "*Creep force in simulations of traction vehicles running on adhesion limit*". Wear, 2005. **258**: p. 992-1000.
- [21] Hosseinipour, M., "*Electromechanical design and development of the Virginia Tech Roller Rig testing facility for performing various studies on wheel-rail contact mechanics and dynamics [Doctoral Thesis]*", in *Mechanical Engineering*. 2016, Virginia Tech: Blacksburg.
- [22] Meymand, S., M. Hosseinipour, and M. Ahmadian, "*The Development of a Roller Rig for Experimental Evaluation of Contact Mechanics for Railway Vehicles*", in *Joint Rail Conference*. 2015: San Jose, California.
- [23] Meymand, S.Z., "*State of the Art Roller Rig for Precise Evaluation of Wheel-Rail Contact Mechanics and Dynamics [Doctoral Thesis]*", in *Mechanical Engineering*. 2015, Virginia Tech: Blacksburg.
- [24] Kumar, S., M.F. Alzoubi, and N.A. Allsayyed. "*Wheel/rail adhesion wear investigation using a quarter scale laboratory testing facility*". in *Proceedings of the 1996 ASME/IEEE Joint Railroad Conference*. 1996.
- [25] Kistler, "*Multichannel Charge Amplifier 5070A*". 2010.
- [26] Kistler, "*3-Component Quartz Force Sensor 9028*". 2013.
- [27] Kistler, "*Troubleshooting Manual – Kistler charge amps*". 2015.
- [28] Andrews, H.I., "*The contact between a locomotive driving wheel and the rail*". Wear, 1959. **2**: p. 468-484.
- [29] Marshall, M.B., R. Lewis, R.S. Dwyer-Joyce, U. Olofsson, and S. Björklund, "*Experimental Characterization of Wheel-Rail Contact Patch Evolution*". Journal of Tribology, 2006. **128**(3): p. 493-504.
- [30] Pau, M., F. Aymerich, and F. Ginesu, "*Distribution of contact pressure in wheel–rail contact area*". Wear, 2002. **253**(1): p. 265-274.
- [31] Dwyer-Joyce, R.S., C. Yao, R. Lewis, and H. Brunskill, "*An ultrasonic sensor for monitoring wheel flange/rail gauge corner contact*". Proceedings of the Institution of Mechanical Engineers, Part F: Journal of Rail and Rapid Transit, 2012. **227**(2): p. 188-195.
- [32] Utah, U.o. "*Contact Stresses and Deformations*". Precision Machine Design [cited 2018 May 3]; Available from: <http://mech.utah.edu/~me7960/lectures/Topic7-ContactStressesAndDeformations.pdf>.
- [33] C., D., *Design and Analysis of Experiments*, ed. 8. 2013.
- [34] Liu, X., P. Bellette, C. Milne, and P. Meehan. "*Investigation about the effect of angle of attack and relative humidity on wheel squeal*". in *Proceedings of ACOUSTICS*. 2011. Gold Coast, Australia.
- [35] Wright, C. "*The Contact Patch*". Hunting [cited 2018 May 3]; Available from: <http://the-contact-patch.com/book/rail/r0418-hunting>.
- [36] Magel, E., A. Tajaddini, M. Trosino, and J. Kalousek, "*Traction, forces, wheel climb and damage in high-speed railway operations*". Wear, 2008. **265**: p. 1446-1451.
- [37] Wang, J., X. Chen, X. Li, and Y. Wu, "*Influence of heavy haul railway curve parameters on rail wear*". Engineering Failure Analysis, 2015. **57**: p. 511-520.
- [38] Guan, Q., J. Zeng, and X. Jin, "*An angle of attack-based derailment criterion for wheel flange climbing*". Proceedings of the Institution of Mechanical Engineers, Part F: Journal of Rail and Rapid Transit, 2013. **228**(7): p. 719-729.

- [39] Spiriyagin, M., O. Polach, and C. Cole, "*Creep force modelling for rail traction vehicles based on the Fastsim algorithm*". *Vehicle System Dynamics: International Journal of Vehicle Mechanics and Mobility*, 2013. **51**.
- [40] Ishizaka, K., S.R. Lewis, and R. Lewis, "*The low adhesion problem due to leaf contamination in the wheel/rail contact: Bonding and low adhesion mechanisms*". *Wear*, 2017. **378-379**: p. 183-197.
- [41] Chen, H., T. Ban, M. Ishida, and T. Nakahara, "*Adhesion between rail/wheel under water lubricated contact*". *Wear*, 2002. **253**(1): p. 75-81.
- [42] Trummer, G., L.E. Buckley-Johnstone, P. Voltr, A. Meierhofer, R. Lewis, and K. Six, "*Wheel-rail creep force model for predicting water induced low adhesion phenomena*". *Tribology International*, 2017. **109**: p. 409-415.
- [43] Beagley, T.M., I.J. McEwen, and C. Pritchard, "*Wheel/rail adhesion — the influence of railhead debris*". *Wear*, 1975. **33**(1): p. 141-152.
- [44] Nakahara, T., K.-S. Baek, H. Chen, and M. Ishida, "*Relationship between surface oxide layer and transient traction characteristics for two steel rollers under unlubricated and water lubricated conditions*". *Wear*, 2011. **271**(1): p. 25-31.

## **ACKNOWLEDGEMENTS**

The authors wish to thank and acknowledge the US Department of Transportation, University Transportation Center Program (RailTEAM UTC) for funding support for this research.

## ABOUT THE AUTHORS

**Mehdi Ahmadian**, J. Bernard Jones Chair and Director

Dr. Mehdi Ahmadian is a Dan Pletta Professor of Mechanical Engineering at Virginia Tech, where he also holds the position of Director of Center for Vehicle Systems and Safety (CVeSS), and the Railway Technologies Laboratory (RLT). Dr. Ahmadian has authored more than 130 archival journal publications and more than 250 conference publications, including a number of keynote lectures. He has served as Editor or Editor-in-Chief for four journals on Vehicle System Dynamics, Vibration and Control, Shock and Vibration and Automobile Engineering. Dr. Ahmadian is Fellow of American Society of Mechanical Engineers of the American Institute for Aeronautics and Astronautics (AIAA). He has received many distinguished scholar awards.

**Karan Kothari**

Mr. Karan Kothari was a graduate research assistant when he worked on this research project. He has his bachelor's degree in mechanical engineering from Vellore Institute of Technology of India and his MS degree from Virginia Tech.